3D-Printed Quasi-Optical Systems for Terahertz Non-Destructive Testing

by

Bryce Chung

In fulfilment of the requirements for the degree of

Doctor of Philosophy

July 2026

College of Engineering and Information Technology

School of Electrical and Mechanical Engineering

Adelaide University

Contents

Contents iii

Abstract vii

Statement of Impact ix

Declaration xi

Acknowledgements xiii

Publications xv

List of Figures xix

List of Figures xx

Outline xxi

I Context 1

1 Introduction 3

1.1 Terahertz Technology . . . 3

1.2 Motivating Applications . . . 4

1.2.1 Non-destructive Testing . . . 5

1.2.2 Ranging . . . 8

1.2.3 Communications . . . 11

1.3 Sources and Detectors . . . 12

1.3.1 Schottky Barrier Diodes . . . 12

1.3.2 Photo-Mixers . . . 14

1.3.3 Pulsed Systems . . . 15

1.4 Terahertz Beam Steering . . . 17

1.4.1 Leaky-Wave Antennas . . . 17
1.4.2 Phased Arrays . . . 17
1.4.3 Mechanically Reconfigurable Optics . . . 18
1.5 3D-printing for Terahertz Applications . . . 19

II Original Contributions 23

2 Terahertz Imaging With 3D-Printed Risley-Prism and Telecentric Objective 25
2.1 Introduction . . . 28
2.2 Design of Optical Train . . . 30
2.2.1 Collimator . . . 31
2.2.2 Risley-Prism . . . 31
2.2.3 Telecentric Objective . . . 32
2.2.4 Assembly . . . 35
2.3 System Performance . . . 36
2.3.1 Focal Plane . . . 36
2.3.2 System Resolutions . . . 38
2.4 Non-Destructive Testing . . . 40
2.5 Discussion . . . 43
2.5.1 3D-printed Anti-Reflection Structures . . . 43
2.5.2 Increasing Scanning Speed . . . 44
2.5.3 Further Evaluating Imaging Performance . . . 44
2.5.4 Further Error Analysis . . . 45
2.6 Conclusion . . . 45

3 Highly Efficient Terahertz Dark-Field Imaging System with 3D-Printed Components 47
3.1 Introduction . . . 50
3.2 Design of Optical Train . . . 52
3.3 Measurement of System Performance . . . 55
3.3.1 Annular-beam Collimation . . . 55
3.3.2 Focal Spot Size . . . 55
3.3.3 Spatial Resolution . . . 55
3.3.4 Efficiency . . . 58
3.4 Demonstration of Simultaneous Bright- and Dark-field Imaging . . . 59
3.4.1 Biological Sensing . . . 59
3.4.2 Surface Defect Detection . . . 60

3.4.3 Defect Detection in Composites . . . 61
3.4.4 Crystalline Identification . . . 64
3.5 Conclusion . . . 64

4 Non-contact Probing of Active Semiconductor Devices Using Terahertz Waves 67
4.1 Introduction . . . 70
4.2 Low Frequency Operation . . . 71
4.2.1 Fresnel and Drude Modelling . . . 71
4.2.2 Experimental Validation . . . 74
4.3 High Frequency Operation . . . 79
4.4 Discussion . . . 82
4.4.1 Model Assumptions and Validity . . . 82
4.4.2 Experimental Considerations . . . 83
4.4.3 Polarization Dependence of Packaged Diodes . . . 83
4.5 Conclusion . . . 84

III The End 85

5 Conclusion and Outlook 87
5.1 Thesis Conclusion . . . 87
5.2 Future Work . . . 88
5.3 Outlook . . . 88

Bibliography 89

Glossary 113

Abstract

The terahertz region of the electromagnetic spectrum is typically considered to be between 100 GHz to 10 THz, with large swathes of this mostly unoccupied frequency range ripe for applications benefiting from high bandwidth. Unfortunately, terahertz sources are inefficient and typically low power, hindering the broad adoption of devices operating at these high frequencies due to low signal to noise ratios; this is further exacerbated by high material and path losses. To maximise the precious transmitted and received terahertz power, quasi-optical components can be used to focus energy onto targets to improve detection sensitivity and spatial resolution, as well as concentrate power towards other antennas for long range transmission. Drastic improvements in 3D-printing technologies over the last few decades have unlocked new quasi-optical designs that take advantage of geometries previously inaccessible to traditional manufacturing methods.

A major challenge with 3D-printing for terahertz applications is finding appropriate materials with low dispersion and minimal dielectric losses for building electrically large structures, while maintaining low prototyping cost and fast turnaround time. Materials commonly used to 3D-print components for the microwave domain are typically lossy at terahertz frequencies, necessitating phase wrapping techniques to minimise thickness, ultimately limiting bandwidth. Fortunately, cyclic olefin copolymer (COC) features low dispersion and low dielectric loss for terahertz waves, while also being easy to 3D-print with consumer grade hardware, permitting terahertz systems to be rapidly prototyped at low cost. In essence, COC has emerged as the choice material for 3D-printed quasi-optical components for the terahertz range.

This thesis showcases how I use COC and a small fleet of consumer grade 3D-printers to build a variety of terahertz quasi-optical systems for non-destructive testing applications. For systems requiring high bandwidth beam-steering, a Risley-prism serves as the core beam manipulation device. Comprised of two counter-rotating COC prisms, the Risley-prism is a simple solution to a lack of effective beam-steering in the terahertz domain. The first of three projects in this thesis combines additional aspherical components with the Risley-prism, forming a functional 3D-printed terahertz imaging system capable of

acquiring detailed near-field images. Second, in order to capture sub-wavelength features indistinguishable by the Risley-prism system, a dark-field setup was developed to drastically enhance terahertz image contrast. Enabled by the complex geometry afforded by 3D-printed COC, this novel dark-field architecture also incorporates bright-field imaging capabilities, allowing for the simultaneous capture of both modes, eliminating reconfiguration time necessary for the sequential systems that exist in literature. The third and final system makes use of 3D-printed lenses to enhance the unprecedented observation of charge carrier dynamics in active semiconductor devices due to terahertz plasma resonance. Using discrete semiconductor components such as diodes and transistors as weak reflective modulators, bias signals buried inside are recovered with terahertz probing. The design of each system is shown in detail and evaluated using a series of experiments intended to represent a real-world application, illuminating new uses for terahertz technology. Future terahertz research will also make use of this work to inform and assist in the development of 3D-printed quasi-optical systems, primarily for but not limited to non-destructive testing purposes.

Statement of Impact

The work contained within this thesis has direct impact on the research community and potential impact on wider society in a number of ways. Generally, the advancement of 3D-printing capabilities demonstrated in this work will help to accelerate terahertz research by reducing the cost of entry and turnaround time for custom low-loss terahertz optics. Previously, the Terahertz engineering laboratory was typically constrained to commercial off the shelf quasi-optical components, which limited the types of optical setups to relatively simple configurations. Cyclic Olefin Copolymer (COC) has been of interest to the terahertz community for some time as a choice material for optical components but historically has been dismissed due to difficulties with 3D-printing. Now that the 3D-printing capability has been developed over the course of my candidature, other researchers can realise their complex ideas in a short timeframe at low cost, rather than waiting for an overseas manufacturer to produce the same components. Our collaborators, both domestic and international, have benefited from discussions on this 3D-printing work, helping them establish their own in-house capabilities. Wider society benefits from this aspect of the research as it accelerates the development of potential beneficial terahertz technologies.

Established literature on the terahertz measurement of semiconductor devices primarily focuses on the determination of offline material properties, such as dopant levels, as the acquisition speed of traditional terahertz time-domain spectroscopy methods are not fast enough to capture operational activity. The work in the latter portion of this thesis which pertains to semiconductor probing has established a novel technique for the terahertz measurement of solid-state devices in operation. This will likely open new approached for quality control and device monitoring in the semiconductor and security industries.

Declaration

I certify that this work contains no material which has been accepted for the award of any other degree or diploma in my name, in any university or other tertiary institution and, to the best of my knowledge and belief, contains no material previously published or written by another person, except where due reference has been made in the text. In addition, I certify that no part of this work will, in the future, be used in a submission in my name, for any other degree or diploma in any university or other tertiary institution without the prior approval of the Adelaide University and where applicable, any partner institution responsible for the joint-award of this degree.

I acknowledge that copyright of published works contained within this thesis resides with the copyright holder(s) of those works.

I also give permission for the digital version of my thesis to be made available on the web, via the University's digital research repository, the Library Search and also through web search engines, unless permission has been granted by the University to restrict access for a period of time.

This research was supported by an Australian Government Research Training Program (RTP) Scholarship doi.org/10.82133/C42F-K220.

Bryce Chung 14/7/2026

Acknowledgements

First and foremost, I would like to acknowledge the immeasurable work of my supervisory panel, Withawat Withayachumnankul, Daniel Headland and Wenle Weng. They have managed to keep me on track over the last four years of my candidature, and I am forever grateful for their guidance, patience, and knowledge.

I was incredibly fortunate to have been allocated to one of Withawat's honours projects in the last year of my bachelor's degree. This is where I first got a taste of terahertz and 3D-printed quasi optics, setting me on the path towards research. Withawat's dedication to his work is second to none, and is what primarily drew me towards continuing my studies with him. He is always willing to answer questions, respond to messages at odd hours of the night, and take time away from his busy schedule to discuss experiments or explain a new idea; I couldn't ask for much more.

Daniel was my tutor for antennas and propagation during my final honours year, and the willing target of my endless questions about what doing a PhD was like. Not eager to pressure me towards PhD, Daniel allowed me to arrive at my own decision to study terahertz. Much like Withawat, Daniel is also incredibly passionate about electromagnetics and supervision, and has been an invaluable source of knowledge in almost any subject I can think of. Having completed his own PhD semi-recently in 2017, he has been a great person to turn to when I needed help navigating the stresses of PhD life.

Although I have not spent as much of my PhD working with Wenle as I have with Withawat and Daniel, his advice early in my candidature has served me very well. Wenle encouraged me to spend countless hours in the lab, to familiarise myself with every piece of test equipment and become a skilled experimentalist. This aspect of my PhD is what I have enjoyed the most.

Despite meeting with my supervisors at least once a week for the last four years, the amount of time spent with them is dwarfed by Harrison (Harry) Lees. Harry has been a close friend during my studies, spending countless hours with me in the lab working on projects, in the kitchen eating lunch, and walking to the supermarket for the sake of walking. Harry's enjoyment of his work and dedication to helping others in the lab is

deeply inspiring. As my time in the lab draws to a close, I will miss him the most.

To everyone else in the terahertz engineering laboratory, thankyou for your advice and shared experience throughout our time spent together. The research group that Withawat has fostered remains one of the closest and most friendly in the school. I have no doubt that my PhD (and conference presentations) would be significantly worse without your discussions around the office and during group meetings.

I don't think I would have been able to complete half of my experiments without the support of Danny Di Giacomo, one of the most hardworking members of staff that I know. Danny has seen me through from first year, taking care of my electronics workshops, all the way to the end of my PhD, helping me design circuits and navigate the eProcurement system. He is always willing to give up his time to help, no matter how difficult the problem. His tireless work is truly inspirational.

I would like to thank the developers of Matplotlib [1] and NumPy [2] for making their incredible software freely available and open-source, it has been invaluable throughout my degree. I think it is safe to assume any original plot in this thesis probably involves those two libraries in some way.

To my parents, Julie and Damian, I am eternally grateful for your unconditional love and support throughout my life and education. You have been fully on-board with any and all of my choices along the way, helping me up through difficult times, and seeing me through good ones. To my sister, Poppy, thankyou for your laughs and support as we both live away from home. To my cat, Socks, thankyou for always waiting at the door, it makes coming home after a long night in the lab just that bit better.

And to those who have contributed to my PhD in some way that I have neglected to include here, I offer my apologies.

Publications

Journal Papers

B. Chung, H. Lees, J. Hesler, C. Chuengsatiansup, and W. Withayachumnankul, *Non-contact probing of active semiconductor devices using terahertz waves,* IEEE Journal of Microwaves, vol. 6, no. 2, pp. 324–333, DOI:10.1109/JMW.2026.3653411.

Contributions: theoretical analysis, experiment design and execution, data processing, and manuscript writing.

B. Chung, H. Lees, M. Ibrahim, D. Headland, and W. Withayachumnankul, *Highly efficient terahertz dark-field imaging system with 3D-printed components (Invited),* Journal of Physics: Photonics, vol. 7, no. 2, art.no. 025012, DOI:10.1088/2515-7647/adb81e.

Contributions: theoretical analysis, experiment design and execution, data processing, and manuscript writing.

B. Chung, D. Headland, and W. Withayachumnankul, *Terahertz imaging With 3D-printed Risley-prism and telecentric objective,* IEEE Transactions on Terahertz Science and Technology, vol. 14, no. 4, pp. 446–454, DOI:10.1109/TTHz.2024.3404642.

Contributions: theoretical analysis, experiment design and execution, data processing, and manuscript writing.

Conference Papers

B. Chung, J. Nedosyko, W. Withayachumnankul, and D. Headland, *Tuning of integrated terahertz disk resonators via evanescent loading,* 2026 19th Australasian Symposium on Antennas, IEEE, *Accepted*.

Contributions: experiment design and execution.

B. Chung, H. Lees, and W. Withayachumnankul, *Quadrature detection systems for contactless probing of active semiconductor devices,* 2025 50th International Conference on Infrared, Millimeter, and Terahertz Waves (IRMMW-THz), IEEE, DOI:10.1109/IRMMW-THz61557.2025.11319829.

Contributions: theoretical analysis, experiment design and execution, data processing, and manuscript writing.

B. Chung, D. Headland, M. Ibrahim, and W. Withayachumnankul, *3D-Printed quasi-optics for sub-terahertz range,* 2024 49th International Conference on Infrared, Millimeter, and Terahertz Waves (IRMMW-THz), IEEE, DOI:10.1109/IR-MMW-THz609-56.2024.10697738.

Contributions: theoretical analysis, experiment design and execution, data processing, and manuscript writing.

B. Chung, H. Lees, C. Chuengsatiansup, and W. Withayachumnankul, *Probing Live PN junctions with terahertz waves,* 2023 48th International Conference on Infrared, Millimeter, and Terahertz Waves (IRMMW-THz), IEEE, DOI:10.1109/IRMMW-THz57677.2023.10299299.

Contributions: theoretical analysis, experiment design and execution, data processing, and manuscript writing.

B. Chung, D. Headland, and W. Withayachumnankul, *3D-Printed quasi-optical components for terahertz applications (Invited),* 2023 IEEE International Symposium on Radio Frequency Integration Technology (RFIT), IEEE,

Contributions: theoretical analysis, experiment design and execution, data processing, and manuscript writing.

B. Chung, H. Lees, D. Headland, and W. Withayachumnankul, *Broadband and efficient terahertz beam scanning using a 3D-printed Risley prism,* 2022 47th International Conference on Infrared, Millimeter and Terahertz Waves (IRMMW-THz), IEEE, DOI:10.1109/IRMMW-THz50927.2022.9895483.

Contributions: theoretical analysis, experiment design and execution, data processing, and manuscript writing.

N. Amnuayphol, H. Lees, **B. Chung**, M. Baumert, and W. Withayachumnankul, *Non-contact vital sign sensing with THz-wave homodyne receiver,* 2026 19th Australasian Symposium on Antennas, IEEE, *Accepted*.

Contributions: experiment design.

H. Lees, **B. Chung**, and W. Withayachumnankul, *Sensitivity measurements of terahertz vibrometer,* 2025 50th International Conference on Infrared, Millimeter, and Terahertz Waves (IRMMW-THz), IEEE, DOI:10.1109/IRMMWTHz61557.-2025.11320076.

Contributions: experiment design and execution, and data processing.

H. Lees, **B. Chung**, and W. Withayachumnankul, *All-silicon 90-degree hybrid coupler for the WR3.4 band,* 2025 50th International Conference on Infrared, Millimeter, and Terahertz Waves (IRMMW-THz), IEEE, DOI:10.1109/IRMMW-THz61557.2025.11319692.

Contributions: experiment design.

H. Lees, **B. Chung**, D. Headland, and W. Withayachumnankul, *Simultaneous multi-target monitoring with terahertz leaky-wave radar,* 2024 49th International Conference on Infrared, Millimeter, and Terahertz Waves (IRMMW-THz), IEEE, DOI:10.1109/IRMMW-THz60956.2024.1069759.

Contributions: experiment design.

List of Figures

1.1 Spectrum of the terahertz region. 3
1.2 Examples of terahertz material characterisation applications. 5
1.3 Examples of terahertz biological sensing applications. 7
1.4 Examples of terahertz food inspection applications. 7
1.5 Examples of terahertz agricultural sensing applications. 8
1.6 Example of high-resolution terahertz radar. 9
1.7 Examples of terahertz security screening applications. 10
1.8 Example of terahertz vital sign detection application. 11
1.9 Impact of atmospheric attenuation of THz waves. 12
1.10 Sketch and schematic of a 440 GHz frequency tripler. 13
1.11 State-of-the-art frequency multiplied sources based on Schottky diode. . . 14
1.12 Leaky-wave antenna illustration and experiment. 18
1.13 Examples of terahertz phased arrays. 18
1.14 Examples of terahertz reconfigurable optics. 19
1.15 Refractive index and absorption coefficient of various thermoplastics used in FDM 3D-printing. 20
1.16 Examples of 3D-printed COC components. 21

2.1 Conceptual model of a large scale terahertz imaging system using a Risley-prism and telecentric objective to detect concealed objects on a torso. 30
2.2 Ray trace diagram of an incident normal beam through a Risley-prism. . . 32
2.3 Illustration of the Risley-prism coordinate space. 33
2.4 Simplified comparison between spherical and aspherical surfaces for telecentric lens design. 34
2.5 Chief ray angle over ϕ_{spot}, along the x-axis of the image plane. 34
2.6 3D rendered images of the Risley-prism system design. 35
2.7 Calibration of the system scanning region. 37
2.8 Evaluation of the spatial resolution of the imaging system using a Siemens star imaging target. 39

2.9 Detection demonstration of metal wire hidden inside marshmallow. . . . 41
2.10 Detection demonstration of hidden chocolates. 42
2.11 Detection demonstration of hidden and missing medication tablets. . . . 42
2.12 Monte Carlo Tolerance Analysis. 45

3.1 Lens train model of the imaging system. 53
3.2 Near field scanning setup of the imaging system. 56
3.3 Spatial resolution test of the imaging system. 57
3.4 Power transmission efficiency of the optical train. 58
3.5 Detection of growth rings in cut *Eucalyptus cladocalyx* branch. 60
3.6 Detection of surface defects on acrylic substrate. 61
3.7 Defect detection in fibreglass block. 62
3.8 Defect detection on carbon fibre panel which has undergone a three-point bend test. 63
3.9 Detection of concealed granular substance in paper envelope. 65

4.1 Simulation of terahertz interaction with free carriers in the PN junction. . 72
4.2 Change in reflectivity of modelled material between 0.1–1 THz 73
4.3 Integrated quadrature receiver system. 75
4.4 Bias voltage ramping at low frequency showing the change in the reflected time-domain signal. 80
4.5 Localization of PN junctions in semiconductor components. 82

Outline

This thesis is divided into three parts, which are each subdivided into chapters.

Part I: Context—contains the chapters which introduce and provide background information on terahertz technology.

Chapter 1: Introduction—introduces terahertz technology and provides a broad review of the literature. This chapter also focuses on 3D-printing and quasi-optics in terahertz research.

Part II: Original Contributions—consists of three self-contained chapters, which are the journal articles I have authored over the course of my candidature.

Chapter 2: Terahertz Imaging With 3D-Printed Risley-Prism and Telecentric Objective—is a terahertz imaging system based on a 3D-printed Risley-prism and supporting quasi-optical components.

Chapter 3: Non-contact Probing of Active Semiconductor Devices Using Terahertz Waves—is a dual-mode terahertz imaging system, able to acquire bright- and dark-field images for enhanced contrast.

Chapter 4: Non-contact Probing of Active Semiconductor Devices Using Terahertz Waves—is a more standard quasi-optical setup which enables the unprecedented measurement of charge carrier dynamics within active semiconductor components.

Part III: The End—summarises and concludes the thesis.

Chapter 5: Conclusion and Outlook—concludes the thesis with some general remarks and future outlook.

Part I

Context

Chapter 1

Introduction

1.1 Terahertz Technology

As radio spectrum on the order of megahertz and gigahertz frequencies becomes more crowded due to the exponential growth in wireless devices, researchers continuously look to push the limits of operating frequency. Continuing this monotonic increase in operation frequency will inevitably lead to an encounter with 'terahertz radiation,' a mostly underutilised region of non-ionising spectrum with ample bandwidth for a host of applications which will be discussed throughout this thesis. However, simply scaling conventional microwave designs up, or photonic designs down, typically fails to meet engineering requirements.

There is some debate within the research community over how much of the electromagnetic spectrum falls underneath the terahertz banner, as those with a microwave engineering background may or may not consider 100 GHz to be far beyond any practical limit of traditional design philosophy and material selection, while those of photonic inclination may group such frequencies with mains electricity. Hyperbole aside, for the purpose of this thesis, the terahertz region of the electromagnetic spectrum is considered to lie within 100 GHz to 10 THz [3], as illustrated in Fig. 1.1.

A major challenge in the advancement of terahertz technology is the position of the research gap between electronic and photonic domains, where we cannot directly apply

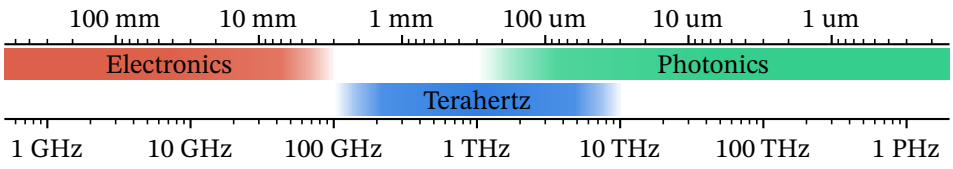

Figure 1.1: Spectrum of the terahertz region.

the centuries of accumulated knowledge from either field. Terahertz researchers must essentially blend the two disciplines together, while also creating new fundamental research. Quasi-optics serves as a prime example of this idea, borrowing mainstream optical design concepts, too electrically large for sub-terahertz frequencies, and combining them with established microwave architectures. Moreover, a core concept throughout this thesis is that the fabrication constraints for terahertz quasi-optics are relaxed due to the millimetre-scale wavelength, permitting the use of affordable 3D-printing techniques considered too imprecise for visible or infrared optics.

1.2 Motivating Applications

In this section I shall discuss some of the applications that have motivated the investment of time and money into fundamental terahertz research over the past few decades. Broadly speaking, the applications of terahertz technology can be grouped into three main areas: non-destructive testing (NDT), typically near-field sensing or imaging of samples for quality assurance or defect detection; ranging, longer distance detection with reduced spatial information; and communications, transmitting data between devices at range.

These application areas exist due to several favourable factors, the first of which is that terahertz waves can traverse many non-conductive materials including, but not limited to, plastics, paper, and clothing, while also being strongly absorbed by polar molecules such as water [4]. For terahertz NDT and ranging applications in particular, this is an advantage over infrared or visible-light based systems, which struggle or fail to penetrate packaging materials or clothing. Lower-frequency microwave and millimetre-wave devices such as airport body scanners are transparent to many of these non-conductive materials. However, terahertz waves much have higher spatial resolution due to their shorter wavelength [5]. This positions terahertz waves in a middle-ground of sorts, having the material penetration properties of microwave devices, but with improved spatial resolution, closer aligned with infrared and beyond.

Where biological samples are concerned, terahertz radiation features low photon energy on the order of milli-eV, too low to ionise atoms or molecules [6], making their use safe for agricultural, biomedical, and handheld operator use. This is a strong advantage over ultraviolet and x-ray wavelengths, where high spatial resolution and material penetration comes at the cost of potentially destructive (depending on the target) probing.

Of benefit to most applications is the large swathes of nearly unused bandwidth in the terahertz region of the spectrum. For NDT and ranging applications, the range resolution is the distance at which the observer can distinguish two targets; this value is propor-

tional to the bandwidth of the probing wave [7], [8]. Where range resolution is important, such as detecting individual layers within a multi-layer structure, high bandwidth is necessary. For communication applications, higher data rates depend on increasing the channel bandwidth, necessary for the growing demand for greater capacity links [6].

1.2.1 Non-destructive Testing

Material Characterisation

The classical use case for terahertz waves since the 80s and 90s has been non-destructive material characterisation with terahertz time-domain spectroscopy (TDS) systems [9], [10], using setups such as the one shown in Fig. 1.2(i). Non-destructive testing of important optical properties such as refractive index and absorption coefficient has proved invaluable in the development of terahertz technology itself. It is also well known that terahertz TDS can be applied to sensing of charge carriers in semiconductor materials [11], [12], illustrated in the terahertz images of doped semiconductor regions in Fig. 1.2(ii) and Fig. 1.2(iii). This is of particular importance to semiconductor manufacturing processes, which assess dopant levels in wafers during production.

Molecular Spectroscopy

It is well known that many vibrational and rotational modes of molecules occur in the terahertz region of the electromagnetic spectrum due to the corresponding low photon

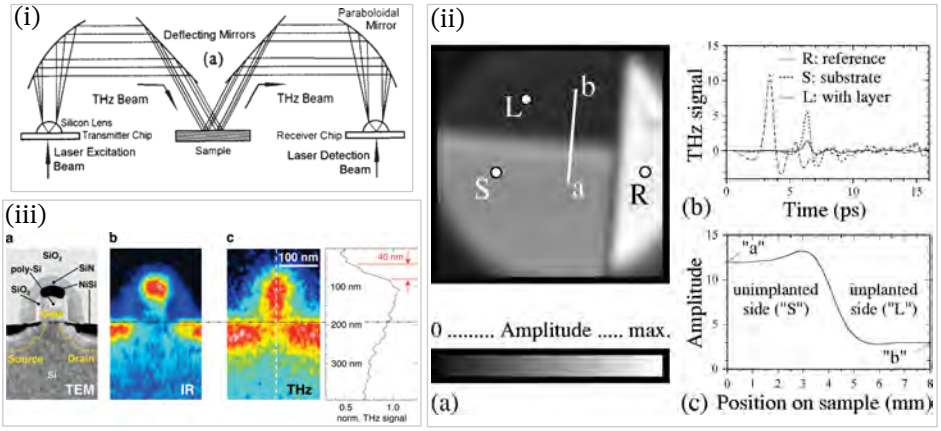

Figure 1.2: Examples of terahertz material characterisation applications. (i) Reflection based terahertz TDS setup for characterisation of doped semiconductors. Reprinted from [10], with the permission of AIP Publishing. (ii) Observation of terahertz TDS transmission affected by ion implantation on silicon sample. Reprinted from [12], with the permission of AIP Publishing. (iii) Comparison between transmission electron microscopy, infrared, and terahertz imaging for dopant regions in transistors. Reprinted with permission from [11]. Copyright 2008 American Chemical Society.

energy [13]. This has been one of the primary application development areas for terahertz research since terahertz TDS was first used to measure the absorption lines of water vapour as mentioned earlier [14]. Since then, applications have expanded to detecting the spectral fingerprints of solid compounds including illicit drugs [15] and explosives [16] for security applications. Another key application for terahertz molecular spectroscopy is quality control in the pharmaceutical industry, where TDS systems complement existing X-ray and infrared methods to provide information on tablet crystallisation and porosity [17]. Furthermore, terahertz liquid sensing takes advantage of the strong interaction with dipoles, such as resonance with hydrogen bonds, allowing for the characterisation of polar liquids [18], [19]. Another historically important area of terahertz spectroscopy research has been astronomy due to the presence of rotational modes of gases in planetary atmospheres and cosmological formations [20], [21], [22]. Sensitivity to water is also critical as researchers seek to understand the origin and viability of life on other planets and the formation of the universe [22]. These systems are found on both ground-based and space telescopes [22], [23], [24].

Chip Failure Analysis

Time-domain reflectometry [25] is an important tool in the failure analysis of integrated semiconductor circuits. By probing and measuring the reflections from a chip, operators can compare the response to a known healthy device to locate discontinuities in impedance along conductive traces [26], [27]. Compared to conventional electronic systems operating at lower frequencies, these electro-optical terahertz pulse reflectometry systems feature much higher bandwidth and thus temporal resolution. Large companies such as NVIDIA use this technology as a first step in failure analysis to screen for faults and inform additional methods to use [28], [29]. By identifying issues during and after production, semiconductor fabrication processes can be tweaked to improve yields.

Biological Sensing

The non-ionising property of terahertz waves lends itself well to the imaging of biological samples as the process is inherently and desirably non-destructive. The strong terahertz absorption by water molecules provides high contrast on external skin conditions, shown in pilot studies on skin conditions such as psoriasis and eczema [30], [31]. Figure 1.3(i) shows the automated setup in [31], allowing for repeatable terahertz measurements of the skin. Early *ex vivo* studies on detecting cancers with terahertz waves, such as in Fig. 1.3(ii), demonstrated that cancerous and healthy tissue could be differentiated via optical properties such as refractive index and absorption coefficient [32], [33]. The first in vivo study of skin cancer with a handheld terahertz scanner demonstrated that skin

cancers could be differentiated from healthy skin, but the confidence in diagnosis across multiple measurements was low [34]. Generally, while terahertz waves can identify unhealthy skin and tissues in controlled environments, much more work is required to build confidence in diagnosis across patients.

Food Inspection

The low photon energy of terahertz waves is also beneficial in cases where the density of the target may be low and unsuitable for NDT using X-ray. Food inspection has long been a focus of terahertz research, showing promise in the detection of foreign material in low density foods such as peanuts [35], crackers [36] and chocolate [37]. Terahertz systems offer a fast solution with minimal health risk in environments where personnel may be overseeing product lines.

Agricultural Sensing

The monitoring of crops in agricultural settings is an emerging area of terahertz research, where terahertz waves are sensitive to the internal structures and fluctuating moisture content of plants. Fragile crops vulnerable to strong variations in weather often have to

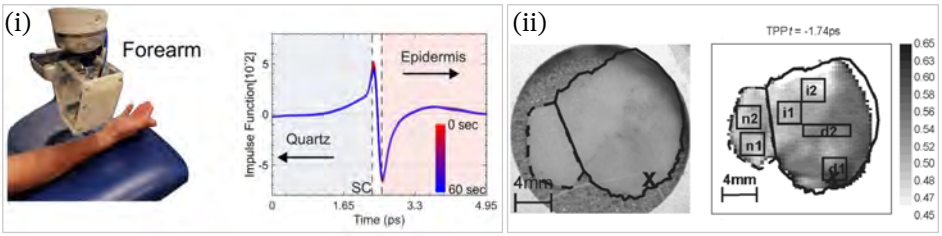

Figure 1.3: Examples of terahertz biological sensing applications. (i) Demonstration of robotic acquisition of terahertz reflection data for skin. Reproduced from Anubhav Dogra et al. [31]. Licensed under CC BY 4.0. (ii) Terahertz analysis and comparison of healthy, inflamed, and diseased skin. Copyright © Institute of Physics and Engineering in Medicine. Reproduced from [32] by permission of IOP Publishing Ltd. All rights reserved

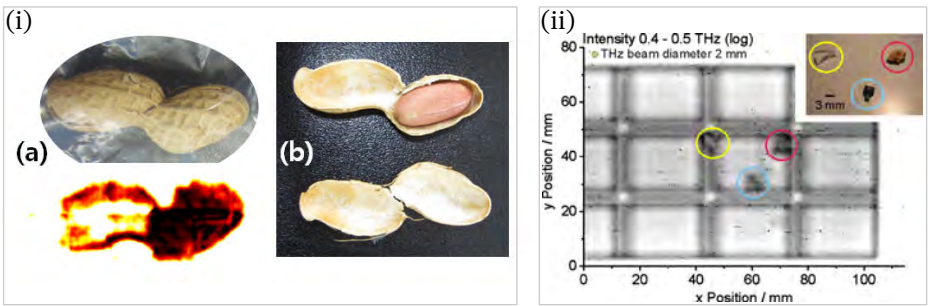

Figure 1.4: Examples of terahertz food inspection. (i) Demonstration of peanut imaging with terahertz gyrotron. Reprinted, with permission, from [36] © 2012 IEEE. (ii) Demonstration of terahertz imaging to detect glass, stone, and metal contaminants in a chocolate bar. Used with permission of Jördens et al., from [37]; permission conveyed through Copyright Clearance Center, Inc.

be manually assessed for moisture content, damage, and health, which is typically time consuming and destructive. Terahertz waves can be used to monitor the moisture content of leaves over time, as shown in Fig. 1.5(i), potentially assisting in the optimisation of watering schedules in order to reduce water usage on farms and inform harvesting plans [38], [39]. Transmissive and reflective terahertz imaging of barley in laboratory conditions has been successfully demonstrated in discriminating between healthy and frost damaged seeds, shown in Fig. 1.5(ii), assisting farmers in determining whether early harvest is necessary [40]. Conventionally, such tests require samples from a spatially diverse set, in order to obtain meaningful results across large areas of land. The long-term vision of these terahertz agricultural applications is to at least have handheld devices for NDT purposes, and eventually move towards drone mounted non-contact terahertz sensors to monitor crop health.

1.2.2 Ranging

The capacity to quickly measure distances accurately is necessary for a wide variety of tasks, from early airspace surveillance systems developed in the 1930s around the time of World War Two [41], to joint international effort in measuring gravitational waves in the 2010s [42]. Most common infrared and visible light detection and ranging (LiDAR) systems measure the time of flight (ToF) from a pulsed laser source reflected by a target, where range resolution is mainly limited by the timing resolution of the electronics [43]. The majority of pulsed systems in the terahertz domain fall under the TDS umbrella, typically used in near-field NDT as mentioned earlier, so we will not mention them here. Laser-based systems provide superior range-resolution, frequency response, and dynamic range in well controlled conditions, but are confounded by dusty or foggy environments due to scattering effects [44]. In such challenging environments, radio de-

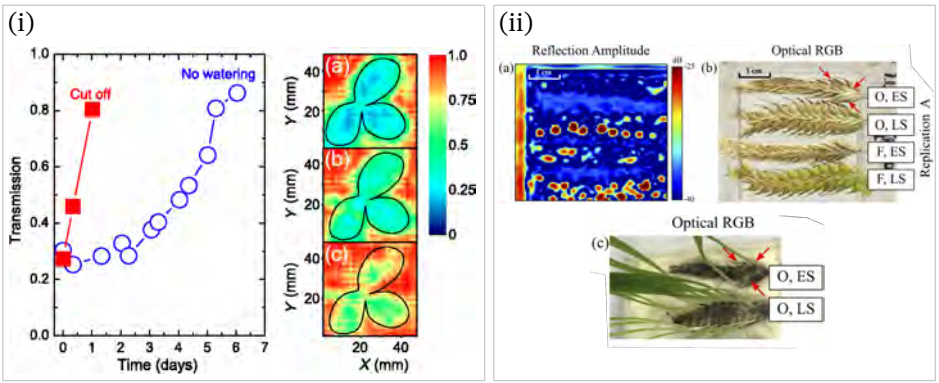

Figure 1.5: Examples of terahertz agricultural sensing applications. (i) Assessing the moisture content of clover over time with terahertz waves. Used with permission of Anton Shchepetilnikov et al., from [38]; permission conveyed through Copyright Clearance Center, Inc. (ii) Demonstration of terahertz NDT on barley to determine healthy and frost damaged seeds. Reproduced from W. S. L. Lee, et al., [40]. Published by Optica Publishing Group under the terms of the OSA Open Access Publishing Agreement.

tection and ranging (radar) systems across microwave to terahertz frequencies are popular, as they are much more resilient to atmospheric disturbances and other visibly opaque obstructions, as long as particles are significantly sub-wavelength.

Historically the development of radar technology has primarily driven by military applications [41], [45]. However, due to high atmospheric absorption and free space path loss, terahertz development is better suited to serve a growing number of short-range civilian applications. Of particular interest are frequency-modulated continuous-wave (FMCW) radar systems, able to measure target distance and velocity by continuously sweeping the transmitted frequency. The frequency difference between transmitted and received signals is proportional to the range, and the measured Doppler shift is proportional to the speed of the target [46]. The terahertz region is well suited for high resolution ranging, as FMCW radar range resolution is proportional to bandwidth [46]. For example, the FMCW radar imaging system displayed in Fig. 1.6 is presented in [47], achieving lateral resolution of 1 mm and range resolution of approximately 1.875 mm over a bandwidth of 80 GHz centred on 343 GHz. It is worth noting that the linearity of the frequency modulation is important and influences the accuracy of a FMCW radar system [48],[49]. Thus maintaining linear sweeping over wide terahertz bandwidths is a key challenge. Additionally, high-frequency terahertz components are smaller than their microwave counterparts, relaxing space constraints, desirable for vehicle or robotic design where room might be limited or come at a cost premium.

Security Screening

In the last few decades, millimetre-wave security scanning systems have become common in airports to screen for prohibited items, such as explosives and weapons, owing to the moderately high imaging resolution allowing for more accurate discernment of hid-

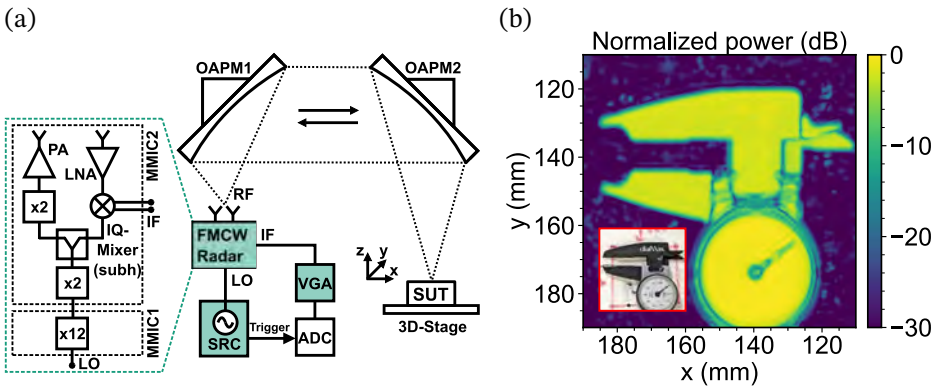

Figure 1.6: Example of high-resolution terahertz radar. (a) System block diagram, showing off-axis parabolic mirror focusing system. (b) terahertz image of the sample under test, a pair of callipers. Reproduced from Benjamin Baumann et al. [47]. Licensed under CC BY 4.0.

den objects [50]. Terahertz based scanners are able to provide security personnel with images of higher resolution due to the shorter wavelength, as demonstrated by the 300 GHz body scanning radar in Fig. 1.7(i), able to show hidden objects and replica weapons on a torso [51]. A limitation of current systems is the need for cooperative and stationary targets, requiring people to stand in a set position for several seconds at a time; ideally, a security scanning system would be 'walk-through' for higher throughput. These systems, as shown in Fig. 1.7(ii), have shown great promise, obtaining high resolution images despite challenging target conditions [52], [53].

Automotive

The number of sensors on passenger vehicles has been rapidly increasing, as automakers include modern autonomous functionalities such as collision avoidance, signage identification, hazard classification, and more. In order to meet the requirements outlined under autonomous driving standards [54], a forward measurement range of over 250 m is expected [43]. Strong motivations for terahertz radar research are found in the autonomous vehicle sector where ranges are in the order of a few hundred metres at frequencies close to 100 GHz [55], [56]. Stationary FMCW ranging demonstrated at 150 GHz with a range resolution of 2.5 cm [57] showed reasonable results at a range of 12 m, under a variety of fog densities. Results showed good agreement with commercial optical camera and ToF LiDAR systems, indicating adding terahertz sensors to the suite of available technologies for automotive use is feasible. Additionally, frequency extenders have been used to implement radar systems aimed at automotive applications in the 300–600 GHz range [58].

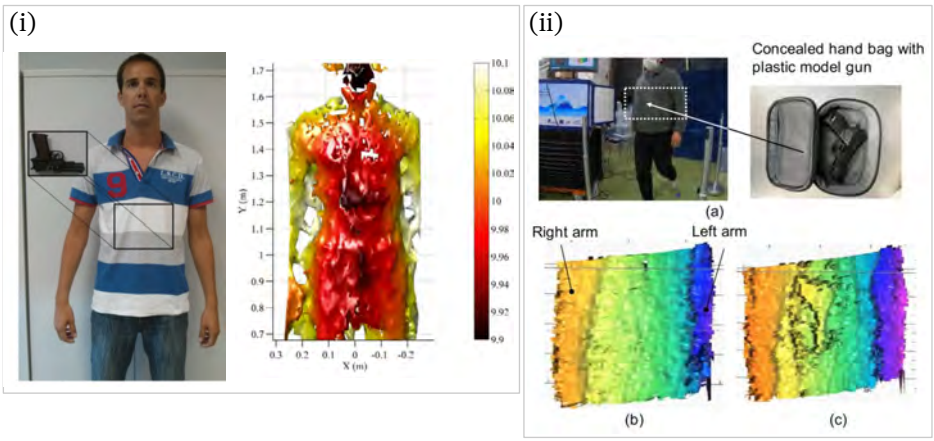

Figure 1.7: Examples of terahertz security screening applications. (i) Stationary terahertz FMCW radar at 300 GHz, revealing hidden replica gun. Adapted from [51] © 2015 IEEE. (ii) Walk-through terahertz FMCW radar at 290 GHz, revealing hidden replica gun. Reproduced from Ikari et al., [52]. Licensed under CC BY 4.0.

Vital Sign Sensing

Non-contact methods for measuring respiratory activity and heart rate in patients are of importance in healthcare scenarios where physically attached probes are not viable or patients may require strict quarantine controls, increasingly relevant in a post-pandemic world [59]. Notably, terahertz waves have higher sensitivity to chest movement from breathing and heartbeat, due to displacements close to the millimetre wavelengths of terahertz waves. This in turn relaxes stand-off distance requirements to maintain acceptable signal to noise, shown in Fig. 1.8 is a 228 GHz radar used to measure heart rate and respiration at 8 m [60]. It is worth noting that this system was successfully extended to 50 m, at the expense of increased noise.

1.2.3 Communications

Terahertz technologies are expected to be a key enabling technology for the next generations of wireless networks [61], [62]. As mentioned previously, the capacity of a communication link is proportional to the available bandwidth; fortunately there are large swathes of spectrum up in the terahertz range that remain mostly unallocated [61], [63]. Unfortunately, free space path losses and atmospheric attenuation pose a significant challenge for medium to long range links at these frequencies, as shown in Fig. 1.9. Additionally, photo-mixer sources are often used in conjunction with infrared fibre-optic communication equipment to enable high data rates, but the terahertz components still suffer from low power output and poor conversion efficiency [64], [65]. This limits potential terahertz communications to within atmospheric windows, but presents an appealing application for private and localised macro cell networks contained within walls which

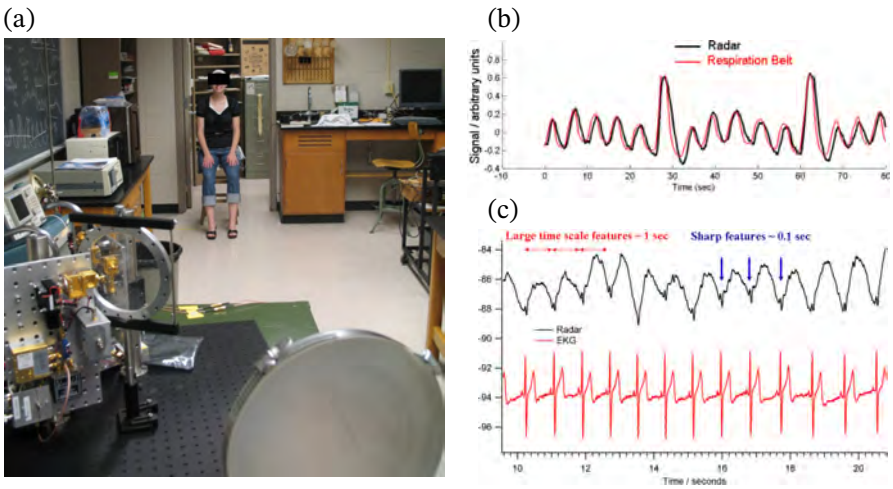

Figure 1.8: Example of terahertz vital sign detection application. (a) Photograph of the target at 8 m distance. (b) Respiration and (c) heart rate from the target in (a), compared to ground truths. Adapted from [60] © 2009 IEEE.

attenuate the majority of terahertz energy [6]. Wireless terahertz links with 220 Gb/s capacity can operate over 214 m at 300 GHz [66], showing promise for these short-range links, useful for local backhaul communications.

1.3 Sources and Detectors

To realise the applications discussed previously, we of course need some way to generate and detect terahertz waves. On the one hand, the generally low output power and efficiency of terahertz sources is still an ongoing challenge and a limiting influence on the widespread adoption of terahertz technologies. On the other hand, over the past few decades, terahertz detector technology has matured with sensitive devices that offer high bandwidth. This leaves us somewhat unbalanced, with satisfactory detection capabilities compensating for the lack of generation capability [4].

1.3.1 Schottky Barrier Diodes

The key technology supporting the original contributions of this thesis are Schottky barrier diodes (SBD), primarily as waveguide-coupled multiplicative sources as shown in Fig. 1.10 [67]. Utilising the non-linear properties of a SBD, terahertz frequency multipliers up-convert the frequency of an input signal by a factor of N, allowing for doubling

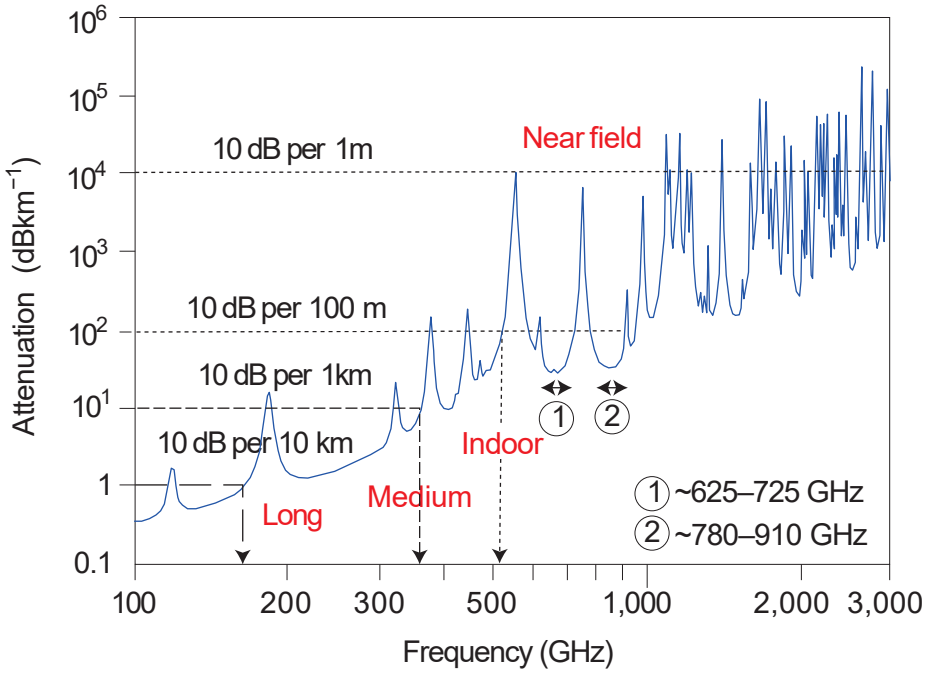

Figure 1.9: Transmission distance is limited by the attenuation, and the appropriate carrier frequency or frequency band is chosen by application, for example, long-distance, medium-distance, indoor and near-field communications. Above 600 GHz, there are two windows for indoor communications: ~625–725 GHz and ~780–910 GHz. Reprinted, with permission, from [61], with permission from Springer Nature.

and tripling operations over practically all of the terahertz range as shown in Fig. 1.11. By chaining a series of multipliers together, with appropriate filtering for unwanted higher order harmonics, terahertz signals can be produced from a microwave-range source [68]. This is particularly useful for implementing test equipment, such as vector network analysers, signal generators, and spectrum analysers, for the terahertz range by extending existing microwave range devices [21], [69]. The conversion efficiency of these devices is moderate, typically ranging between 15–20%, coming at the expense of bandwidth [70]. A state of the art tripler in the 306–317 GHz range is capable of producing >100 mW of terahertz power, at conversion efficiencies of >17% [71].

A downside to multiplicative sources is that phase noise degrades by $20 \log N$, relative to the input signal, meaning that generating terahertz waves with SBD multipliers beyond the 1.5–2.0 THz range comes at the cost of significant noise. Further detail on mixing architectures to overcome phase noise is available in Chapter 4.

SBDs are also commonly used as mixers and zero-bias square law detectors, where their

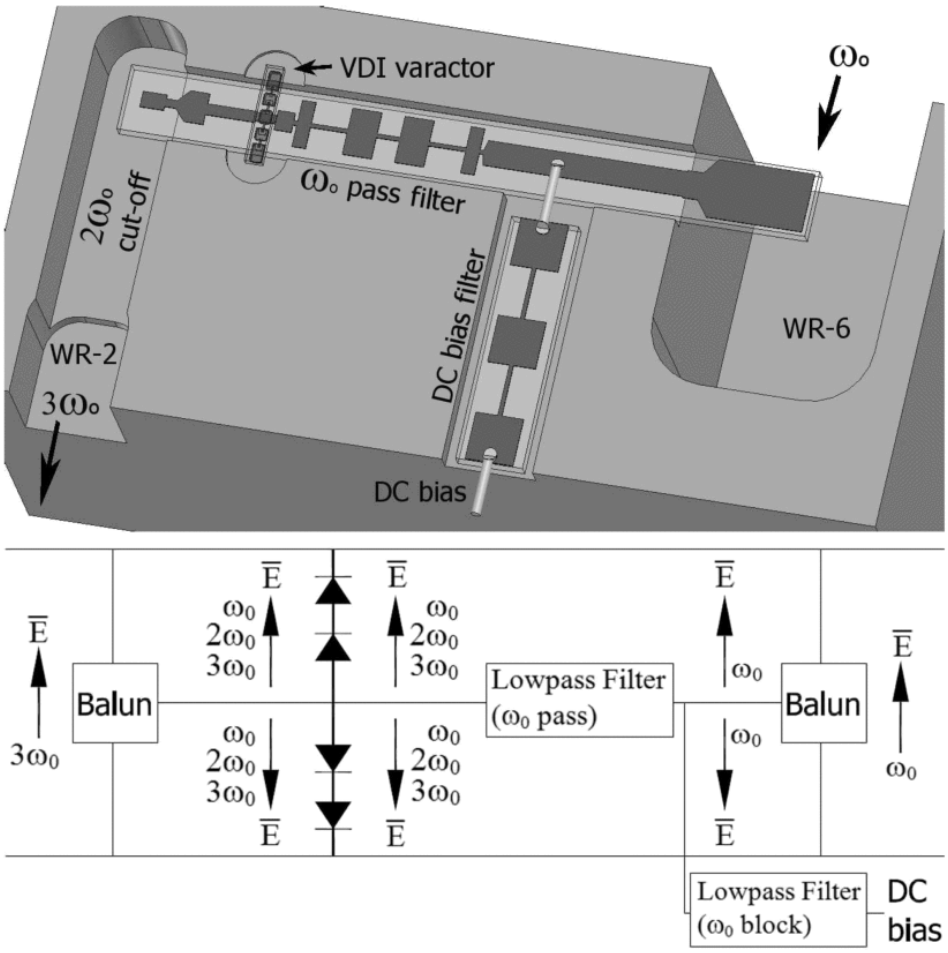

Figure 1.10: Sketch and schematic of a 440 GHz frequency tripler, based on Virginia Diodes (VDI) Schottky varactor diode chip. The waveguide block is split in the E-plane and the top half removed to expose the circuits. The waveguide backshorts are machined in a fixed position. Adapted from [67] © 2007 IEEE.

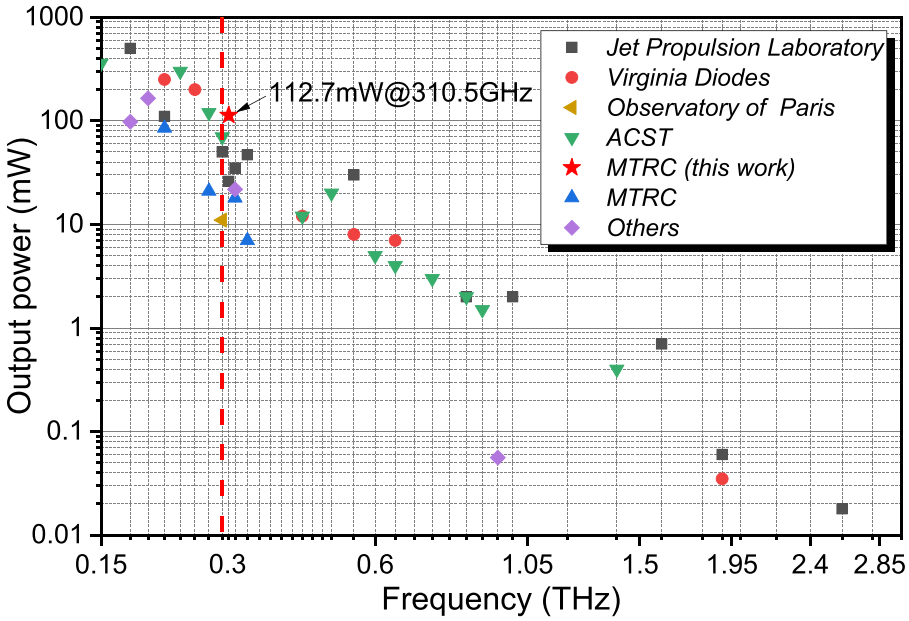

Figure 1.11: State-of-the-art frequency multiplied sources based on Schottky diode. Data table: Jet Propulsion Laboratory [72], [73], [74], [75], [70], [76], [77], Virginia Diodes [78], [79], [80], Observatory of Paris [81], ACST [82], [83], [84], [85], MTRC [86], [87], [88], [89], [90], Others [91], [92], [93], [94]. Reprinted, with permission, from [71] © 2025 IEEE

high sensitivity and fast response time in comparison to other detectors, such as Golay cells, pyroelectric detectors and bolometers [95], is advantageous, particularly for communications [61], [96], [97]. For practical consideration, SBD devices also permit room temperature operation, in comparison to bolometer style detectors, which require active cooling in order to detect the low energy terahertz waves below thermal noise.

1.3.2 Photo-Mixers

Early on in my candidature, I investigated photo-mixers as a potential alternative to electronic multipliers for my NDT and ranging projects. Photo-mixers are devices that use lasers to generate and detect terahertz waves, instead of multiplying radio-frequency sources. Despite choosing multiplicative devices, I shall briefly mention photo-mixers here as they remain widely used in the literature.

For applications with more-stringent phase noise constraints, photonic sources such as PIN and uni-traveling-carrier photodiodes (UTC-PD) are popular [98], [99]. The incredible stability offered by Brillouin lasers can also be exploited for ultra low phase noise applications in the terahertz range [100]. To generate terahertz power these devices are optically pumped with two continuous-wave (CW) lasers, separated by a beat frequency equal to the desired terahertz output [101]. It is preferable for these devices function near telecommunication wavelengths of 1.5 μm to take advantage of compact fibre cou-

pled sources [102]. One of the lasers can be modulated in order to increase and decrease the beat frequency, allowing for FMCW operation in the terahertz domain. As mentioned previously, nonlinearities in the frequency sweeping introduce distortions in FMCW systems, as such it is important that photo-mixers for these applications are well characterised. Fortunately drift diffusion models [103] have been used to calculate the non-linearities in both UTC [104], [105] and PIN [106] photodiodes.

Furthermore, to decrease phase noise from using two laser sources, a single, high quality, FMCW laser can be used in conjunction with a micro-resonator to produce a frequency modulated optical comb at roughly 1550 nm wavelengths [107]. This has the additional benefit of being able to measure range and velocity at multiple frequencies, mapped spatially with dispersive optics. This work should in theory be able to be extended to terahertz ranging.

1.3.3 Pulsed Systems

This thesis is primarily concerned with devices and systems operating in CW, but it is worth briefly mentioning pulsed sources and detectors to provide some background information relevant to the applications mentioned previously. The historical use of pulsed systems has enabled and driven the development of modern terahertz sources and detectors by enabling the characterization of new suitable materials and emergence of novel applications, so it is appropriate they are acknowledged. Common reasons to choose CW over pulsed terahertz systems are cost and acquisition speed. Due to the manufacturing precision and complexity required by laser components, pulsed systems cost significantly more than CW alternatives. The use of delay lines or other means limits measurement to slow changes over time, with acquisition speeds reaching a ceiling of approximately a million samples per second [108].

Photoconductive Antennas

Widely considered mature and commonly found across terahertz research groups worldwide, photoconductive antennas (PCA) have been used since the early experiments by Grischkowsky [14]. The bandwidth of these devices is high, making them particularly useful for static spectroscopic applications where spectral fingerprints may span octaves. The operation of PCAs is relatively straightforward and safe, as they operate at room temperature and utilise fibre-coupled lasers typically not-exceeding 30 mW. For use as sources, femtosecond laser pulses are impinged onto an extremely fast semiconducting

material to generate free carriers, which are accelerated by an applied DC bias to produce a photocurrent. This current pulse is coupled to an antenna to radiate a broadband terahertz pulse into free space, often through a silicon lens [109]. For measurement, the inverse occurs, where the terahertz pulse is impinged onto the antenna, inducing a transient bias voltage. A copy of the source laser pulse with swept delay pumps the receiver to generate a short burst of carriers, convolved over the time-delay with the terahertz pulse. This allows the temporal profile of the transmitted terahertz pulse to be coherently recovered. The primary drawback of these setups are the slow measurement times, limited by the sweeping of the optical delay line. However, asynchronous optical sampling (ASOPS) and electronically controlled optical sampling (ECOPS) systems have become increasingly popular in commercial offerings, utilising a second pulsed laser instead of a delay line to increase measurement frequency to the order of kHz [13]. Non-coherent Schottky-based detection schemes are also common, removing optical delay lines to sacrifice spectral information for significantly improved measurement speed [110].

Non-linear Crystals

For broadband applications requiring higher average power and field amplitude than what is offered by PCAs, optical rectification of ultrashort pulsed lasers is an attractive solution [111]. Femtosecond laser pulses impinged upon a suitable electro-optic non-linear crystal, such as ZnTe or LiNbO3, undergo difference frequency mixing, down converting spectral components from the pulse into the terahertz range [13]. The bandwidth and temporal shape of the generated terahertz radiation is primarily dependent on the bandwidth of the laser pulse and the phase matching between the input laser and output terahertz pulses. Sampling a terahertz pulse with non-linear crystals is similar to the receiving setup used with PCAs, in this case a copy of the laser pulse is propagated through another crystal and phase modulated by the terahertz pulse [112].

Beyond Popular Devices

Although PCAs and non-linear crystals are widespread throughout the terahertz research community, other technologies exist where factors such as absolute power or frequency stability is critical to applications. They will not be exhaustively covered in this thesis but acknowledged as important to the continual advancement of terahertz science and applications. Devices such as free electron lasers and gyrotrons fill a niche where cost and compactness are not important considerations and power is on the order of kilowatts to megawatts [113]. Precision metrology with quantum cascade lasers is possible but requires complex cryocooled setups [114].

1.4 Terahertz Beam Steering

As discussed previously, the efficient generation of terahertz radiation still remains a challenge, and so terahertz devices need to be highly efficient and directive to concentrate and conserve power wherever possible. The concept of beam steering aims to somewhat alleviate the poor performance of terahertz sources, by maximising transmitted power towards the receiver. Beam steering is particularly important for directive and high-gain links, where active antenna alignment is necessary for long-range transmission. Broadly speaking, three types of beamforming exist for use in the terahertz domain: leaky-wave antennas (LWA), phased arrays, and mechanically reconfigurable optics [115].

1.4.1 Leaky-Wave Antennas

LWAs operate on the principle of frequency dependent beam steering, where the radiation source increases and decreases frequency to change the direction of the output beam, as illustrated in Fig. 1.12(a). Although LWAs have been demonstrated for terahertz communication [116], they are of limited use in steering beams with high bandwidth due to the spatial mapping of frequency. In other words, a highly directional LWA sacrifices bandwidth in a single direction for the ability to steer a beam over a wider field of view. This inherently limits the range resolution and data rate of ranging and communication applications. Although LWAs offer impressive scan areas for ranging applications, they are also conventionally limited to a single scanning plane [117]. An advantageous use case for LWAs is the tracking of multiple targets without any moving components, as was demonstrated effectively in [118] and reproduced here in Fig. 1.12. For frequency-agnostic and narrowband applications where beams are required to cover multiple directions, such as CW Doppler radar, LWAs are a suitable option [119].

1.4.2 Phased Arrays

Phased arrays are a classical approach to beam steering from the radio-frequency (RF) domain which make use of coherent antenna arrays with precisely controlled phase relationships to tilt the direction of a beam [120]. This presents a fast and dynamic beam steering solution with no moving parts, ideal for scenarios requiring high-speed tracking, such as mobile telecommunications, military targeting, and autonomous driving. Unfortunately the performance of current terahertz phase shifters is subpar, as high insertion loss limits the physical scale of phased arrays, hampering their development for applications requiring large aperture sizes. It is worth noting that advancements in complementary metal-oxide-semiconductor (CMOS) technology have continued to progress

research in terahertz phased arrays, typically by coupling and synchronising an array of sources, as shown in Fig. 1.13(a) [121]. The approach shown in Fig. 1.13(b) typically features low radiated power and DC-to-RF efficiency often below 1% [122].

1.4.3 Mechanically Reconfigurable Optics

In scenarios where bandwidth is key and speed is a secondary consideration, mechanically reconfigurable optics present an attractive trade-off in performance metrics. This design paradigm is typically cost effective, in most cases requiring only motors and optical components; this improves accessibility, since researchers likely do not require com-

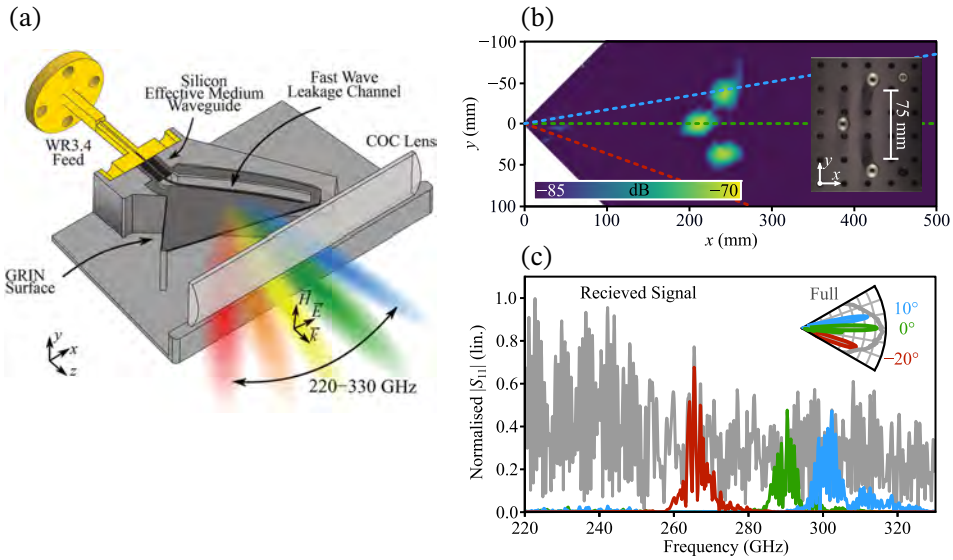

Figure 1.12: Leaky-wave antenna illustration and experiment. (a) Illustration of leaky-wave antenna and packaging with cyclic olefin copolymer (COC) lens. (b) Experimental demonstration of simultaneous target tracking. (c) showing frequency mapping of direction. Adapted from Harrison Lees et al. [118]. Licensed under CC BY.

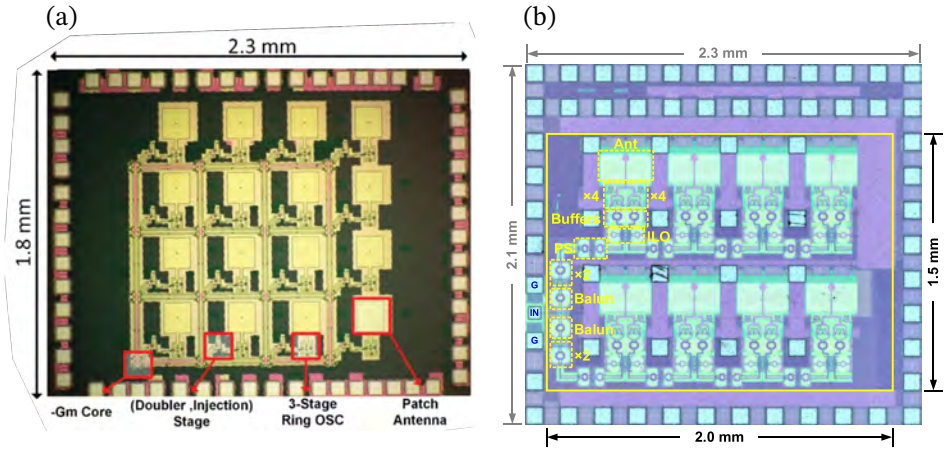

Figure 1.13: Examples of terahertz phased arrays. (a) 4 × 4 phased array at 416 GHz. Adapted, with permission, from [121] © 2022 IEEE. (b) 4 × 2 phased array at 298–334 GHz. Adapted, with permission, from [122] © 2025 IEEE.

plex fabrication. Although glass components used for conventional refractive optics are less favourable at terahertz frequencies owing to high dielectric losses and dispersive properties, the underlying design principles remain the same, so design techniques are often inspired by work done in the optical domain. Mechanical scanning designs commonly found in optical systems such as gimballed mirrors [123], [124] and galvanometer scanners [125] have found use in terahertz applications. Often found in the microwave domain, adjustable Luneburg lenses, as shown in Fig. 1.14(a), serve as compact mechanical beamformers at terahertz frequencies [126], [127]. These devices require minimal adjustment for wide steering angles. In addition to pre-established concepts, the umbrella of reconfigurable optics covers a wide variety of unique and innovative designs, such as the reconfigurable diffraction grating shown in Fig. 1.14(b) [128]. Another method of altering the physical structure of a focusing lens is realised by the pumping of oil into a flexible lens container [129]. Discussed in more detail in Chapter 2, Risley-prisms from the optical domain have shown promise in terahertz applications due to the straightforward and broadband nature of the design. A challenge across the reconfigurable optics design paradigm is finding suitable materials and manufacturing processes, as complex designs are often expensive and difficult to produce with conventional tools [130].

1.5 3D-printing for Terahertz Applications

The advancement of 3D printing technology in the last decade or so has been beneficial to terahertz research, with researchers now having the capability to quickly produce reasonable quality parts at low cost in the lab [131]. Consumer grade fused deposition

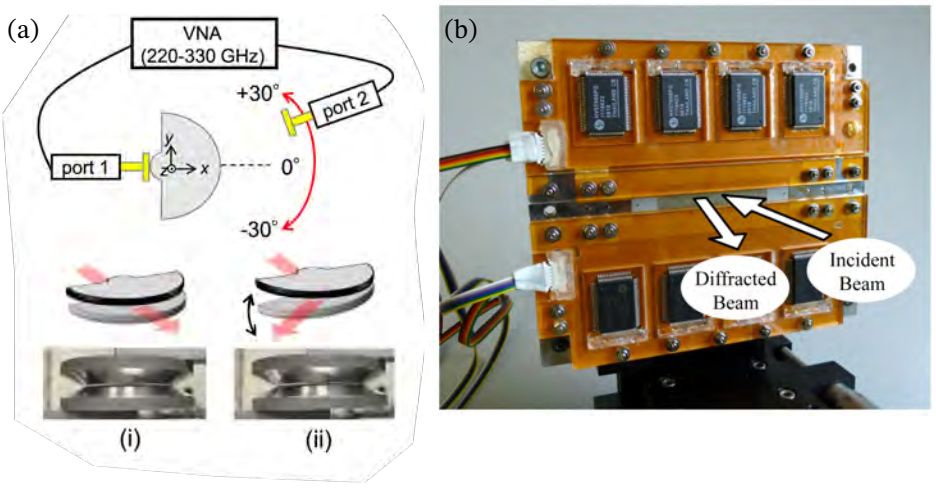

Figure 1.14: Examples of terahertz reconfigurable optics. (a) Mechanically adjustable Luneburg lens. Reprinted, with permission, from [126] © 2020 IEEE. (b) Reconfigurable diffraction grating. Reproduced from Y. Monnai et al. [128]. Published by Optica Publishing Group under the terms of the OSA Open Access Publishing Agreement.

modelling (FDM) printers are typically capable of fine enough resolution to achieve results matching simulations [132], reducing the dependence on traditional manufacturing techniques that limit design freedom. Common 3D printing materials such as Acrylonitrile Butadiene Styrene (ABS) and Polylactic Acid (PLA) perform adequately at RF frequencies [133], but do not appear well suited to the terahertz domain, suffering from high dielectric losses [134], [135], visible in Fig. 1.15. However more exotic 3D-printable polymers show reasonable results across terahertz frequencies [136]. A key example is COC, a printable material exhibiting low dispersion and loss which has been of great use in 3D-printing terahertz research for approximately a decade [137]. Due to surface roughness approaching wavelength scale, 3D-printed lenses typically become less effective around 500–600 GHz [138], although post-processing likely extends the frequency range by reducing the effects of scattering. Although the applications of 3D-printing in the terahertz domain are vast, in this section we shall constrain discussion to mostly transmissive quasi-optical structures.

One of the motivating factors behind the original contributions of Chapter 2 was to improve upon the work of Wu et. al. [140], in which the steering of a Bessel beam is demonstrated using two discrete dielectric lenses based on a Risley prism to achieve a two dimensional scanning system. The use of resin printed components incurs signif-

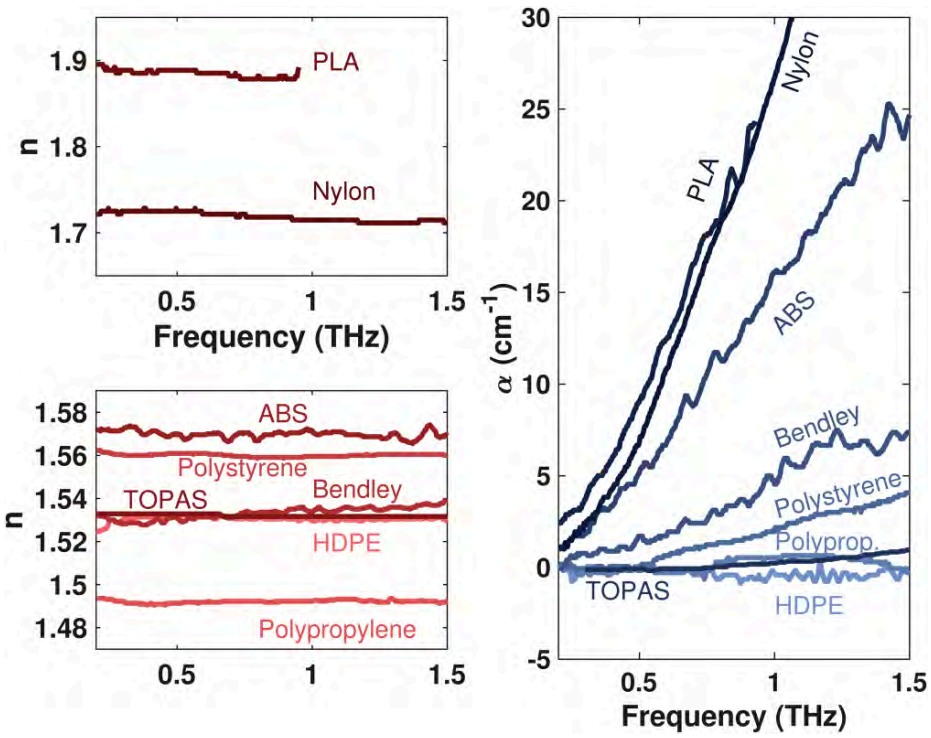

Figure 1.15: Refractive index and absorption coefficient of various thermoplastics used in FDM 3D-printing. The acronyms and abbreviations are HDPE = High Density Polyethylene, Polyprop. = Polypropylene, ABS = Acrylonitrile Butadiene Styrene, and PLA = Polyactic acid. Data from Refs. [138] and [137]. Reprinted from [139] with permission from AIP Publishing.

icant material losses, as the photopolymer materials which polymerize when exposed to ultraviolet light are highly absorptive at terahertz frequencies [141]. To work around these lossy materials, designs make use of phase wrapping to minimise the thickness of material that a terahertz wave must pass through, thus reducing the loss [140]. This inherently leads to bandwidth restrictions, as phase wrapping is designed around a centre frequency, making this technique unsuitable for the plethora of broadband applications mentioned earlier.

An advantage of 3D-printing is the design freedom afforded by the technology, allowing researchers to create complex geometries that would typically be difficult with conventional machining. Simple designs such as common plano-convex lenses have been well documented [142], and more demanding devices such as bendable COC waveguides [143] have already been realised. Other components for lab use such as 3D-printed dielectric resonators have been demonstrated for frequency reference applications [144], and 3D-printed polarizers for low-terahertz frequencies [145], 3D-printed anti-reflection structures [146], and 3D-printed axicon lenses and off-axis parabolic mirrors were realised for long focal depth imaging systems [147]. 3D-printed dielectric antennas have also been demonstrated direction of arrival applications [148]. This shows that 3D-printing can be applied to most, if not all, areas of terahertz research.

Printing parameters such as layer height and flow rate do affect the optical properties of COC [149], and considerable work has been done to document the optimisation of these settings [143]. Furthermore, it is known in the microwave domain that the fill factor of 3D-printed parts influences their properties [150], [151]. This concept has been extended to terahertz frequencies, where the refractive index and absorption coefficient of COC can be controlled via printing parameters [152]. This new paradigm unlocks many potential gradient index designs from optics for the terahertz region, realisable

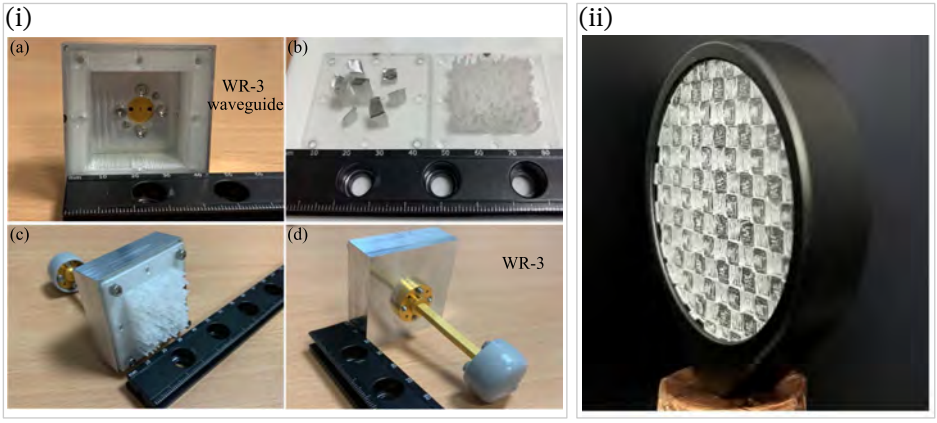

Figure 1.16: Examples of 3D-printed COC components. (a) 3D-printed COC cavity antenna for direction of arrival applications. Reprinted, with permission, from [148] © 2024 IEEE. (b) 3D-printed COC frequency reference. Reproduced from Tobias Kubiczek et al. [144]. Licensed under CC BY 4.0.

with cheap 3D-printing [127], [153].

Researchers are now no longer limited by material choice in regards to 3D-printing quasi-optical components for the terahertz range, all that is left is imagination and a willingness to iterate on failed prints. This leads us to Part II to scratch the surface on the application of 3D-printed COC quasi-optics.

Part II

Original Contributions

Chapter 2

Terahertz Imaging With 3D-Printed Risley-Prism and Telecentric Objective

Abstract

Non-destructive testing is one of the key envisaged applications for terahertz technology due to non-ionizing energy levels and the ability to penetrate many optically opaque materials. Conventional terahertz imaging systems typically rely on raster scanning the target with a moving transceiver, or make use of goniometric beam manipulation schemes. As an alternative, we propose the use of a Risley-prism, essentially a cascaded pair of independently rotating prisms, to function as a simple beam-steering mechanism. When deployed in conjunction with an aspheric, telecentric objective, the Risley-prism allows for scanning a focused terahertz beam in two dimensions. We utilize 3D-printed COC, a low-loss and low-dispersion polymer, to minimize material loss and facilitate the construction of these bulk optics. Owing to true time delay, our imaging system operates over 220–330 GHz, making use of this bandwidth for resolving depth features and hidden objects. We achieve a spatial resolution of 0.419 lp/mm over a circular scanning region 27.8 mm in diameter. The proposed Risley-prism imaging system offers a simple solution to the complicated problem of broadband and high resolution imaging, and hence is readily amenable to widespread adoption and commercial applications.

Statement of Authorship

Title of Paper	Terahertz Imaging With 3D-Printed Risley-Prism and Telecentric Objective
Publication Status	Published
Publication Details	**B. Chung**, D. Headland, and W. Withayachumnankul, IEEE Transactions on Terahertz Science and Technology, vol. 14, no. 4, pp. 446–454, 23 May 2024, DOI:10.1109/TTHz.2024.3404642.

Principal Author

Principal Author	Bryce Chung
Contribution to Paper	Theoretical analysis, experiment design and execution, data processing, and manuscript writing.
Overall Percentage (%)	80%
Certification	This paper reports on original research I conducted during the period of my research degree candidature and is not subject to any obligations or contractual agreements with a third party that would constrain its inclusion in this thesis. I am the primary author of this paper.
Signature	.....
Date	.....

Co-Author Contributions

By signing this Statement of Authorship, each author certifies that:

I. The candidate's stated contribution to the publication is accurate (as detailed above),

II. Permission is granted for the candidate to include the publication in the thesis; and

III. The sum of all co-author contributions is equal to 100% less the candidate's stated contribution.

Name of Co-Author	Daniel Headland
Contribution to Paper	Conceptualization, drafting
Signature	.....
Date	.....

Name of Co-Author	Withawat Withayachumnankul
Contribution to Paper	Conceptualization, drafting, resources
Signature	.....
Date	.....

2.1 Introduction

The need to explore underutilized portions of the electromagnetic spectrum above the microwave range has become clear in recent decades. Abundant and unoccupied bandwidth in the terahertz spectrum presents a multitude of opportunities for high capacity communication links [63], high resolution ranging [51], and NDT and imaging [7], [40], [47], [154], [155]. With respect to imaging applications in particular, the non-ionizing energy levels at low terahertz wavelengths offer a favourable combination of biological safety and spatial resolution. Furthermore, the ability of terahertz waves to penetrate dry and non-metallic substances, and typically estimate material density better than radio-frequency or X-ray range devices, offers unique opportunities for security screening, food contamination detection, and production-line monitoring systems [37], [156]. Nonetheless, high free space path loss, lossy materials, and atmospheric attenuation due to water vapor are at odds with the low available source power typically observed in the terahertz range, posing the biggest threat to the widespread adoption of terahertz domain technologies [157]. To overcome these challenges and take advantage of the terahertz domain, low-loss beam-steering techniques must conserve terahertz power and operate over the wide available bandwidth [115].

Terahertz imaging systems often utilize single-source and single-detector schemes, which permit broadband operation, but typically suffer from slow, bulky and inefficient raster scanning techniques requiring the source, detector, or sample to move [47], [158]. Tilting and rotating mirrors serve as a broadband and highly efficient alternative to raster scanning [159], [160], [161], [162], [163], but typically involve complicated apparatus such as a Gregorian focusing system, as exploited in [51]. Multi-pixel terahertz microbolometers for direct detection permit faster acquisition time, but are frequency- and phase-insensitive, and hence unable to take full advantage of available bandwidth [164]. Despite intensive research, these multi-pixel direct detection schemes are costly and challenging to fabricate. The need for broadband beam-steering schemes with fast acquisition times for imaging has created an area of highly active research, leading to a wide variety of solutions [137], [140], [165], [166], [167]. However, their principles of operation typically impose intrinsic limitations upon operating bandwidth, reducing performance in practical applications. In our work, we assert that broadband systems are necessary for imaging in order to resolve depth features and avoid artifacts due to interference effects in narrowband.

A promising solution for beam-steering, a Risley-prism is a pair of two dielectric prisms which diffract incident light to a controlled angle, adjustable by the independent rotation of each prism. Originally devised for ophthalmological purposes [168], the Risley-prism concept has been used for radio-frequency beam-steering [169], [170] and antenna

alignment [171] as well as optical ranging [172] and communication [173] systems. Terahertz ranging and imaging with a Risley-prism had been demonstrated in narrowband, as bandwidth was limited by high material loss and resultant phase wrapping [140]. A broadband terahertz-pulse imaging system, operating in reflection-mode by incorporating a Risley-prism and telecentric objective has been realized, but comes with the drawbacks of small aperture size and spherical lens componentry, hampered by expensive crystalline quasi-optics [174]. In addition, the use of quartz components and a beamsplitter introduces additional and unnecessary losses, worsening signal to noise ratio (SNR) given the typically low source power in the terahertz range. Such imaging setups requiring precise manual alignment are typically not amenable to applications in the field. Broadband biomedical spectroscopy has made use of the Risley-prism, requiring physical contact between the device and the analyte [175]. Despite broadband operation, the Risley-prism concept remains underutilized in the terahertz domain for free-space communications applications, with limited demonstrations [176].

In this study, we introduce an optical train consisting of a Risley-prism in tandem with a collimator and telecentric objective to realize a complete and broadband imaging system, as illustrated in Fig. 2.1. All these components are 3D-printed with COC, featuring low dispersion and low material loss, with a relative permittivity of $\varepsilon_r = 2.34$ and loss tangent $\tan\delta = 0.0019$ at 220 GHz [137], [143], [177], [178]. 3D-printing permits the rapid prototyping of aspheric quasi-optics for the terahertz range, allowing our system to maintain image quality across the scanning area, as opposed to the systems using conventional spherical surfaces. The low cost of 3D-printing in comparison to traditional methods such as milling and grinding also encourages uptake of terahertz systems for real-world applications. The broadband nature of COC lenses permits us to use a vector network analyser (VNA) to capture complex reflection spectra, and perform time-domain analysis techniques to observe depth features. Our system operates at a fractional bandwidth of 40%, which is limited by the VNA system, at a centre frequency of 275 GHz. The inclusion of the telecentric objective allows for normal incidence on a target, maximizing detectable power in reflection. In addition, operating in the reflection mode allows for greater flexibility regarding targets, where systems operating in transmission may not be able to place the receiver on the other side of the sample. The $\pm 10.5°$ field of view from the Risley-prism is focused with the telecentric objective to cover a circular scanning region with a diameter of 27.8 mm. The results and discussion throughout this work support further development of a larger scale system capable of performing full body imaging, as illustrated in Fig. 2.1(c).

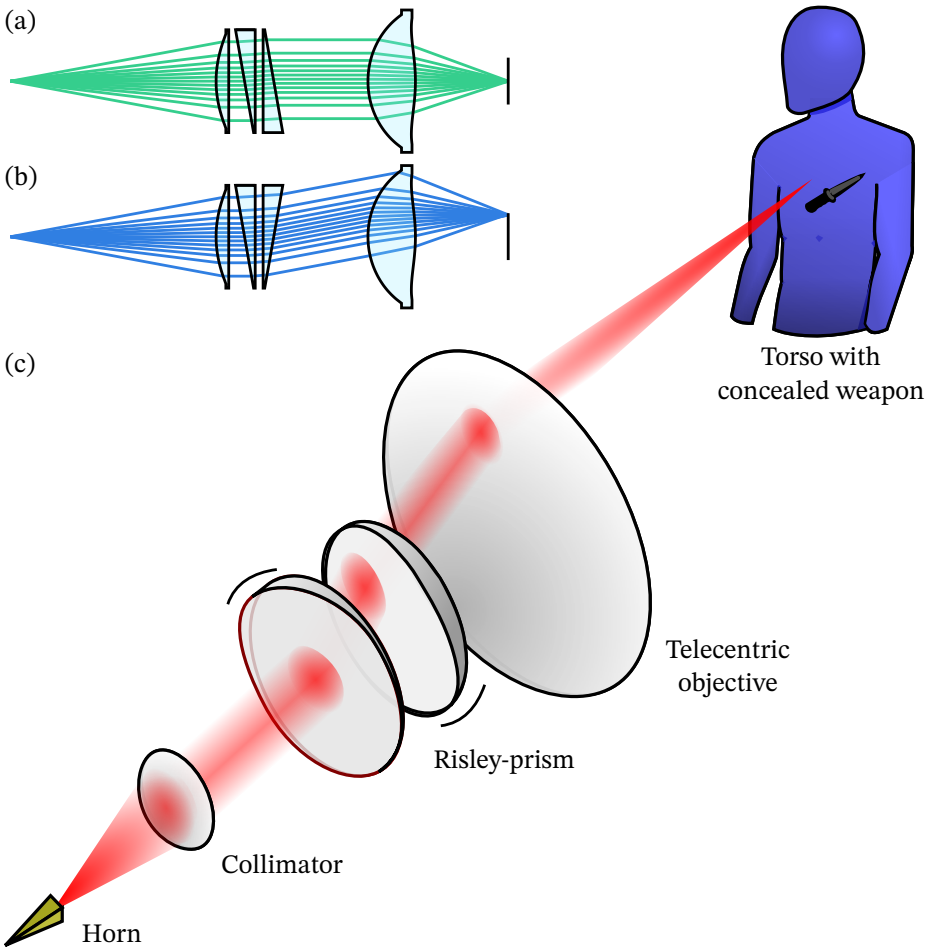

Figure 2.1: Conceptual model of a large scale terahertz imaging system using a Risley-prism and telecentric objective to detect concealed objects on a torso. (a) Minimum deflection and (b) maximum deflection configurations. (c) 3D illustration of the system, showing normal wave incidence on the target to maximize detectable power in reflection.

2.2 Design of Optical Train

The design procedure depends on information about the refractive index of 3D-printed COC, and to this end, a 10-mm thick puck of COC is 3D-printed by a Prusa MK3S+ at 100% infill, and the refractive index $n_{\mathrm{COC}} = 1.521$ and loss tangent $\tan\delta = 0.00039$ is extracted with the VNA, using the method outlined in [179]. The loss tangent is lower than reported in the literature, likely due to the presence of sub-wavelength air voids in the puck. The material loss of the COC is low enough to be safely neglected for designing lens geometry. Identical printing parameters are used for all COC components hereafter.

Since COC is low-loss, reflections at the air and COC interfaces are the primary source of loss in the system, of which there are eight in one direction. For index $n_{\mathrm{COC}} = 1.521$, $n_{\mathrm{air}} = 1$ and assuming normal incidence for the best case scenario, the transmitted power

through each individual surface is:

$$T = 1 - \left|\frac{n_1 - n_2}{n_1 + n_2}\right|^2 = 0.957\ . \tag{2.1}$$

Raising T to the power of 16 for the number of surfaces for transmission to and reflection from the target, 49.74% of the original power is lost. This estimate is consistent with the losses due to Fresnel reflection as calculated using the system modelled in Ansys Zemax OpticStudio, and assumed to be accurate given our previous work on measuring transmission efficiency for a COC Risley-prism [180] showed good agreement between calculations and measured data. Reduction in reflection losses is possible through the addition of anti-reflection layers based on COC with lower infills. Further discussion on such anti-reflection structures is found in the latter part of the thesis.

We note that since full-wave simulation and optimization techniques for electrically large structures such as lenses require significant computation and time resources, we use ray-tracing within Ansys Zemax OpticStudio for the design of the lens components. We also note that the physical optics solver is a reasonable middle-ground between full-wave and ray-tracing methods, but is not used for design and optimization in this work as it lacks operands for beam angle.

2.2.1 Collimator

An aspheric singlet lens is designed in Ansys Zemax OpticStudio to collimate the approximately Gaussian output of a diagonal horn antenna into a beam of approximately 50 mm in diameter at 220 GHz, as shown in Fig. 2.1(a, b). The collimator is positioned sufficiently far from the horn antenna that it may be treated as a point source. The beam divergence from the horn antenna is known and inversely proportional to frequency; the half angle of the beam is approximately 10.5°, 8.8° and 7.6° at 220, 275 and 330 GHz respectively. In this work, we use a separate quasi-optical component for beam collimation for modularity, allowing the imaging system to be used with other antennas and terahertz equipment. A more compact version would combine the collimator and the first prism, reducing the number of reflections from air-COC interfaces.

2.2.2 Risley-Prism

We first describe the operating principle of the Risley-prism, which consists of two parallel and identical dielectric prisms, which are henceforth referred to as wedges to avoid confusion. As illustrated in Fig. 2.2, each wedge has incline angle α to deflect the inci-

dent ray according to Snell's law,

$$\phi_0 = \arcsin\left(n_{\mathrm{COC}} \times \sin\alpha\right) - \alpha. \tag{2.2}$$

For a prism of two wedges of $\alpha = 10°$, the maximum deflection angle is $2\phi_0 = 10.63°$; our preliminary work showed this calculated deflection aligns well with measurement [180]. By counter-rotating both wedges according to the two-step method [181], the output beam can be scanned over both angular dimensions, albeit constrained by the solid angle of maximum deflection. To point the beam at a specified $(\phi_{\mathrm{spot}}, \theta_{\mathrm{spot}})$ within this region, the wedges are rotated by (θ_1, θ_2), as illustrated in Fig. 2.3.

A noteworthy physical limitation of the Risley-prism is the inability to point the beam down boresight, leaving a small region in the centre of the scanning area which cannot be targeted. The radius r_d of this centre null is proportional to the distance S between the two prisms, as well as prism geometry and dielectric properties, as the beam propagates between the air-gap and acquires translation as illustrated in Fig. 2.2(b). This limitation can potentially be overcome with the introduction of a third wedge [182]. Alternatively, here we account for this offset in the design of the telecentric objective.

2.2.3 Telecentric Objective

Having designed the mechanism by which we are to steer the two-dimensional angular trajectory of a beam, we now direct our attention towards the quasi-optical component for focusing the steered output to a small spot in the focal plane with normal incidence and compensating for the centre offset inherent to the Risley-prism as illustrated in Fig. 2.2(b). For this purpose, we use an aspheric biconvex lens, with the benefit of minimizing aberrations and chief ray angle compared to a conventional spherical lens, enabling a more consistent image quality across the image plane and maximising reflected

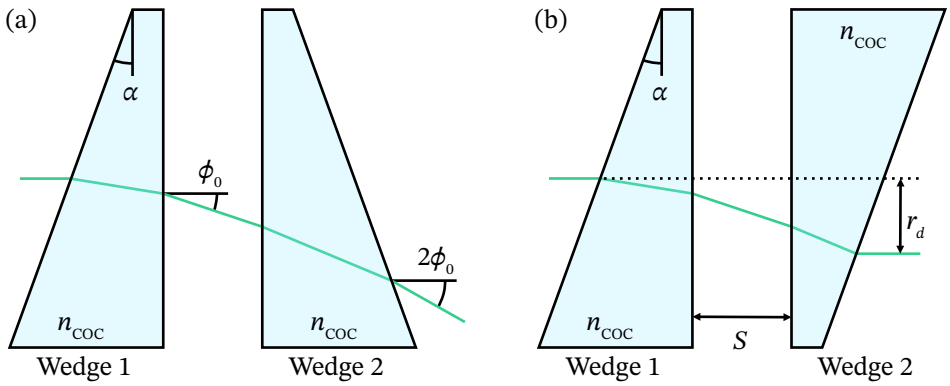

Figure 2.2: Ray trace diagram of an incident normal beam through a Risley-prism. Both wedges feature an inline angle α. (a) Maximum deflection configuration. (b) Minimum deflection configuration showing the centre offset r_d.

power. Figure 2.4 illustrates some advantages of using an aspheric lens, in contrast to a spherical one. Namely, reduced aberrations at increased field angles and consistent spot size across the image plane with the aspheric lens can be seen in Fig. 2.4(a, b). The chief ray angle shown in Fig. 2.4(c) is lower and more consistent when using the aspheric lens. Whilst aspherical lenses are typically seen as difficult to manufacture using traditional methods such as grinding, 3D-printing allows us to easily prototype arbitrary lens geometries as needed.

Using a ray-tracing model in Ansys Zemax OpticsStudio, with the least squares optimization algorithm, a COC telecentric lens is optimized to focus the output of the Risley-prism onto the image plane, minimizing the spot size and the chief ray angle of two configurations of the Risley-prism, namely minimum and maximum deflection. The chief ray angle is used to estimate the angle of incidence at the imaging plane, with Fig. 2.5 showing the angle is maintained below 1°.

The design of the telecentric objective is subject to the key trade-off between scanning region size and spatial resolution. For a larger scanning area, greater excursion of the steered beam away from the optical axis is required. The telecentric objective must be either positioned at a greater distance from the Risley-prism, in turn increasing the focal length of the lens, or a steeper incline angle must be used for the Risley-prism. Increasing the focal length degrades the spatial resolution according to Gaussian beam propagation

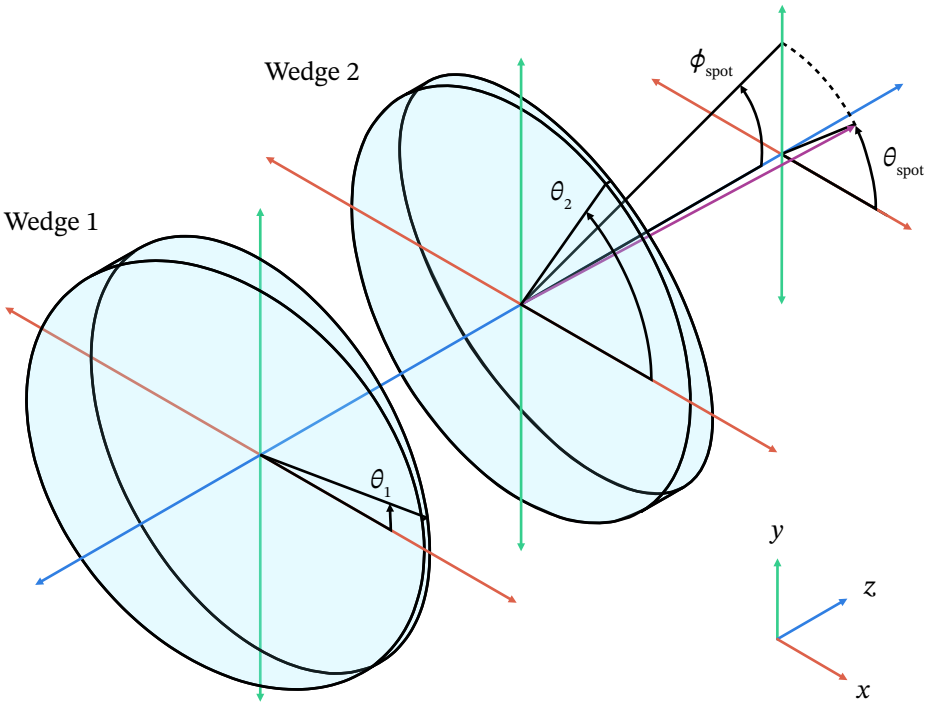

Figure 2.3: Illustration of the Risley-prism coordinate space. Each wedge is rotated about the z-axis by angle θ_k, where k is the wedge number. θ_1 and θ_2 for a desired ϕ_{spot} and θ_{spot} are found using the two step inverse method [181].

theory. Increasing the incline angle of the wedges widens the centre-null of the Risley-prism, increasing the angle of incidence at the centre of the scanning region. To improve spatial resolution, the focal length can be decreased, or the beam diameter into the objective can be increased. At 275 GHz, our design features a theoretical focal length of 58.7 mm, spot size of 2.398 mm, and Rayleigh length of 2.5 mm, for a reasonable compromise between system size, spatial resolution and scanning area, appropriate for the targets under investigation.

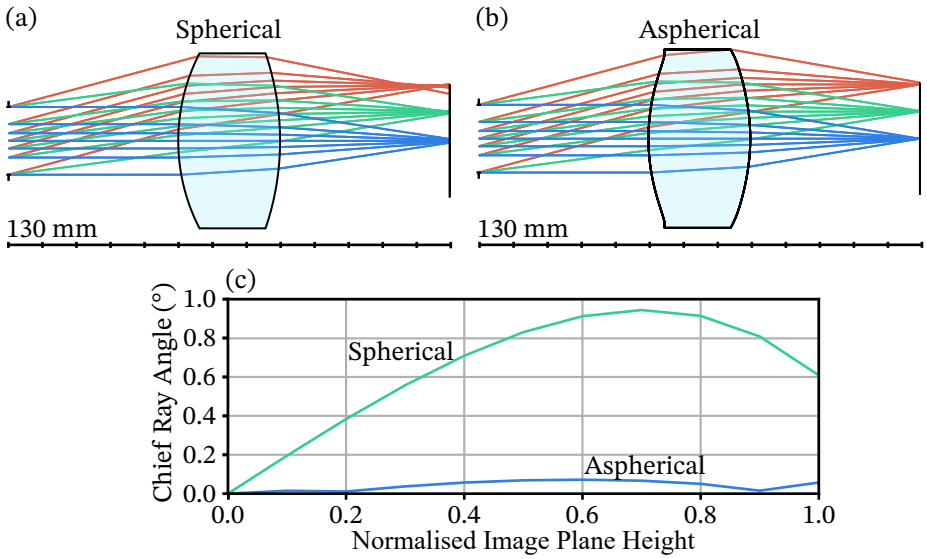

Figure 2.4: Simplified comparison between spherical and aspherical surfaces for telecentric lens design. Both lenses are optimized with the same figure of merit to minimize spot size and chief ray angle, from a beam diameter of 20 mm with up to 15° deflection. (a) Spherical biconvex lens, showing aberrations at maximum field angle. (b) Aspheric biconvex lens, with reduced aberrations compared to the spherical design. (c) Chief ray angle over the image plane. For optimization, the distance from the entrance pupil to the first surface and the distance from the second surface to the image plane are fixed at 50 mm. The thickness of the lens is fixed at 30 mm. The radii of the spherical surfaces are variable. The radii, conic constant, and even-aspheric coefficients of the aspheric surfaces are variable.

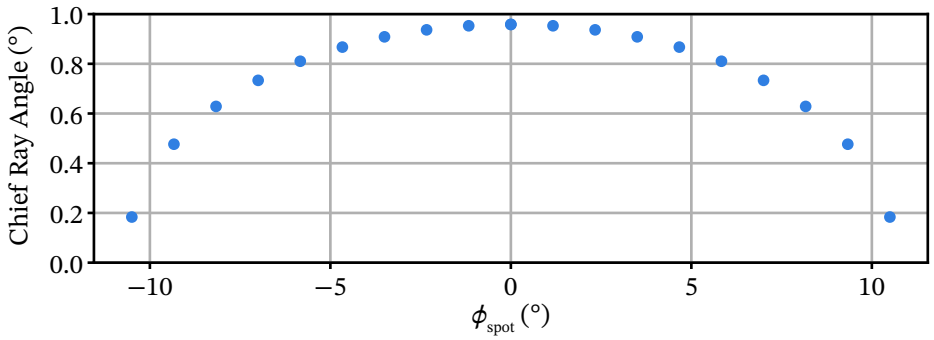

Figure 2.5: Chief ray angle over ϕ_{spot}, along the x-axis of the image plane. Computed with the Risley-prism in conjunction with the telecentric objective, at various configurations, like those shown in Fig. 2.1(a,b).

2.2.4 Assembly

To combine the collimator, Risley-prism, and telecentric objective into a single unit, the packaged system in Fig. 2.6 is designed to mount and align the components. Each wedge is affixed with screws to a 3D printed ring, incorporating a 140-tooth gear profile. The ring is pressed into a bearing, and the bearing is pressed into a 3D-printed frame that also serves as the mounting point for motors and switches. The collimating optic is mounted directly to the frame of first rotating wedge. An open-loop stepper motor with a 20-tooth pulley is connected to each wedge via a tensioned belt, geared at a ratio of 140:20 to achieve a rotational resolution of 0.257° for each wedge, given a 1.8° step angle of the stepper motor. This translates to a arc-length spatial resolution of 0.0623 mm along the circumference of the scanning region, and a maximum elevation resolution of 0.186°, corresponding to a worst case elevation spatial resolution of 0.252 mm at the edge of the scanning region. Microswitches are used to home the wedges to the zero position. It is noted that the use of a rotation resolver for position feedback and high speed motors in a constant rotation configuration would significantly decrease acquisition time, but is deemed too expensive and complicated; the current stepper motor system functions as a low speed proof of concept. Each dataset in this work is collected over approximately three hours, with the exception of the Siemens star, which is intentionally over-sampled.

We expect the lower limit of acquisition time for rotational scanning to be lower than that of conventional raster scanning, as compensating for inertia in rotation is easier than linear movement. M6 bolt holes allow the entire system to be fastened to standard 25 mm optical mounting surfaces for experimental characterization. It is noted that some artifacts occur when the wedges are near minimum and maximum rotation angles of 0° and 360° respectively, where the control algorithm wraps above 360°. This is attributed to open loop control and inaccuracies of the 3D-printed components. Artifacts also oc-

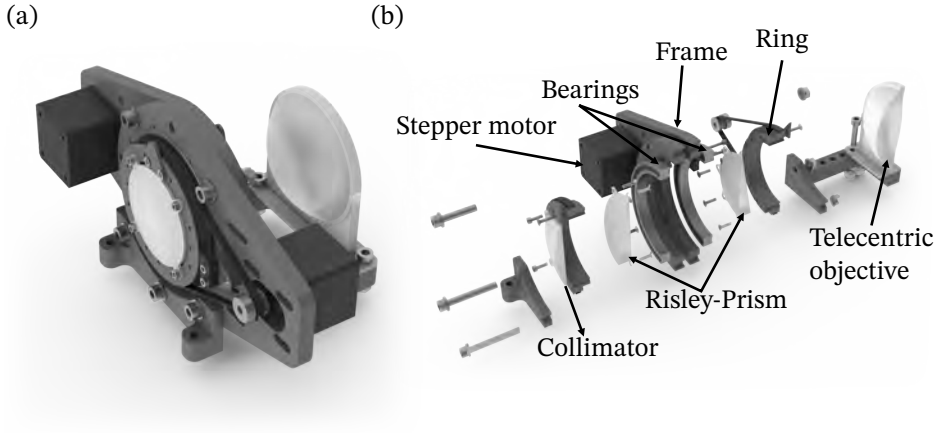

Figure 2.6: 3D rendered images of the Risley-prism system design. (a) Collapsed model view. (b) Exploded view along cutting plane.

cur when the Risley-prism is pointing at $\theta = 0°$. Both sets of artifacts are omitted from the measurements and linearly interpolated over. Linear interpolation is also performed on each image to transform the angular coordinate system to Cartesian for plotting purposes.

2.3 System Performance

All experiments are performed with a Keysight 5222B VNA with WR-3.4 frequency extenders for 220–330 GHz operation. This allows for convenient and coherent evaluation of the reflection of the analyte, through the quasi-optical imaging system that is the main subject of this work, via the complex S_{11} response.

2.3.1 Focal Plane

To validate and calibrate the operation of the motion control algorithm and assess the homing error of the Risley-prism hardware, the focused beam is pointed to the left, centre and right of the x-axis on the focal plane, and the near field distribution of each position is scanned with the motorized xy translation stages shown in Fig. 2.7(a). Complex S_{21} is measured with the VNA at increments of 0.25 mm over a scanning range of 40×6 mm^2. This measurement is compared against the footprint diagrams generated in Ansys Zemax OpticStudio, which includes Fig. 2.7(b), showing no homing inaccuracy, and Fig. 2.7(c) showing the same system with $-3°$ of homing error on both wedges, rotating the axis. Summed transmission intensity images shown in Fig. 2.7(d) confirm the Risley-prism system operates as expected, with good agreement between expected and measured positions. Minor rotation is visible in the summed transmission intensity images shown in Fig. 2.7(d), where the outermost focal spots are slightly above and below $y = 0$ mm, indicating some small error in the homing, attributed to the use of physical switches. The distance between the focal spots in Fig. 2.7(e) serves as a calibration for the scanning region, measured at 27.8 mm in diameter. The phase of each spot in Fig. 2.7(f–h) is also observed to ensure approximately Gaussian focus at normal incidence at the inner and outer regions of the scanning area.

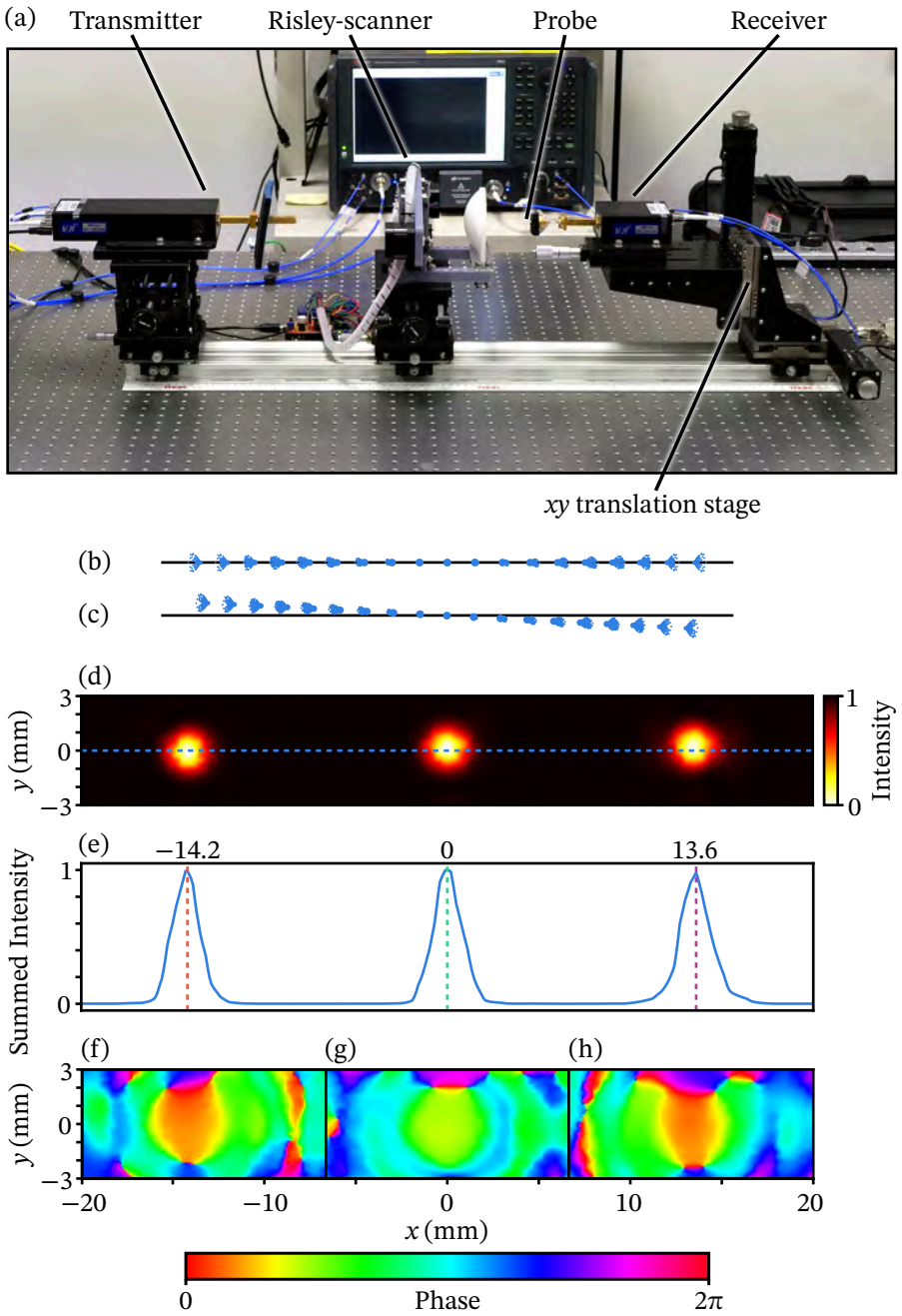

Figure 2.7: Calibration of the system scanning region. A S_{21} raster-scan is taken for each azimuth position of −10.5, 0, 10.5° with a near-field probe. (a) Side view photo of the raster scanning setup. (b) Ray-traced footprint diagram showing the spot positions along the x-axis; see Visualization 1. (c) Footprint diagram showing the effect of wedge positioning error. With both wedges offset −3°, there is rotation along the points. (d) Three raster scans of S_{21} intensity at 275 GHz normalized and summed, with probe at the focal plane. (e) Cross section at the midpoint of the summed intensity scans showing 27.8 mm between the two furthest points.(f–h) Phase profile of each raster scan at 275 GHz.

2.3.2 System Resolutions

Spatial Resolution

High spatial resolution allows for fine features to be resolved. Hence, it is important to quantify the limits of the imaging system; to do this, two experiments are performed. First, Gaussian curves are fitted over the 2D raster-scans from Section 2.3.1 to find the average $1/e^2$ beam width of the focal spot at 220, 275 and 330 GHz. Although spot size is not particularly useful for comparing imaging systems, it serves as an estimation of image quality, as a high spatial resolution requires low focal spot size. The theoretical $1/e^2$ beam width of a coherent system is [183],

$$w = \frac{0.82\lambda}{\mathrm{NA}} \,. \tag{2.3}$$

When the wavelength $\lambda = 1.364, 1.091, 0.909$ mm and numerical aperture $= 0.446, 0.373, 0.323$, the beam width is therefore 2.508, 2.398, 2.308 mm, respectively. The numerical aperture takes into consideration the narrowing beam divergence of the horn antenna proportional to wavelength. Thus, the beam from the antenna progressively under-illuminates the collimator, reducing the resolving power of the system as frequency increases. The measured average spot size of 3.52, 3.12 and 2.89 mm approximately align with the calculated values. This discrepancy is attributed to inaccuracies in the 3D-printed lenses and minor misalignment during experimental setup.

In the second experiment, we image a Siemens star, a common target used to evaluate the spatial resolution of a complete imaging system [184]. The star, shown in Fig. 2.8(a), is mounted in a plastic frame and placed at the focal plane of the objective, as shown in Fig. 2.8(b). The Siemens star is a copper circle on FR4 fibreglass substrate, with thirty alternating segments, half with copper etched away. By imaging this target, we estimate the spatial resolution $N/(2\pi r)$ in line pairs per millimetre, where $N = 15$ is the number of segment pairs, and r is the radius from the centre of the star, according to the method detailed in [185]. Probing the Siemens-star radially, the outermost radius will feature maximum contrast between the highly reflective copper and the fibreglass due to the lower spatial frequency. Towards the centre of the star, the segments will appear to touch as the spatial frequency increases, at which point the system is not capable of resolving any higher spatial frequencies. Ordinarily, we would determine the spatial resolution relative to frequency, but due to the interference effects that can be seen in Fig. 2.8(c–e), the resolution cannot be accurately estimated in narrowband. This is where the broadband nature of the imaging system becomes relevant, by allowing us to resolve time delay by processing the frequency domain data.

The control algorithm points the beam to 40956 equidistant points within the solid an-

gle range of the Risley-prism, scanning from the centre outwards in a spiral pattern. Performing an inverse fast Fourier transform (IFFT) on each complex S_{11} measurement pixel, which contains the spectrum over 220–330 GHz, we obtain the time-domain signal representative of each pixel. To form a 2D image, the Risley-prism output elevation angle ϕ_{spot} is normalized by the maximum deflection angle of 10.5° and multiplied by 13.9 mm to form a radial distance, and the angle from the x-axis θ_{spot} is used to map the measured points to polar coordinates within a unit circle. For image export purposes, the polar data is interpolated over a 500×500 point Cartesian grid, using linear interpolation, and normalized to the maximum intensity. This information is plotted to show the reflection intensity over time delay, allowing us to move a virtual observation plane through time, which corresponds to the axis of propagation. The time step between each observation plane is approximately 1.51 ps, assuming a sampling frequency of 660 GHz to meet Nyquist requirements for measuring spectrum up to 330 GHz. In the case of the Siemens star, the spatial resolution is evaluated in the observation plane at

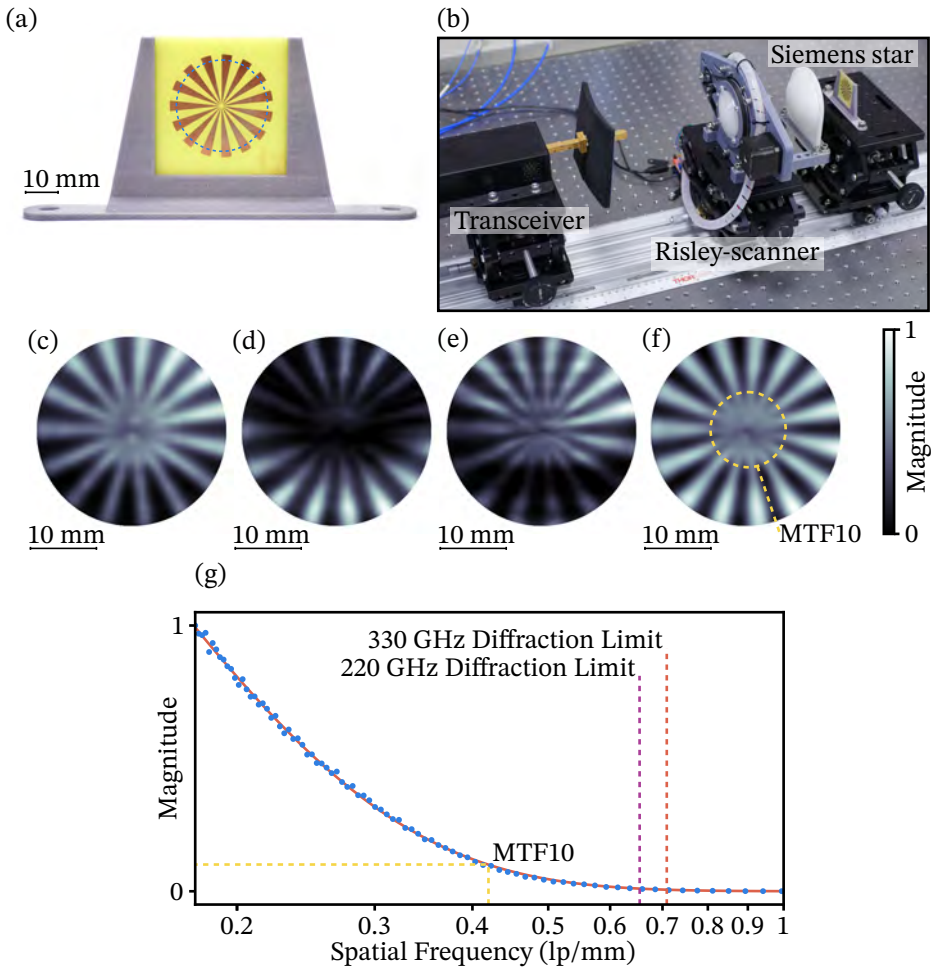

Figure 2.8: Evaluation of the spatial resolution of the imaging system using a Siemens star imaging target. (a) Front view photo of Siemens star. (b) Photo of experimental setup. (c, d, e) S_{11} at 220, 275 and 330 GHz. (f) Observation plane at the peak reflection in the time-domain. (g) Modulation transfer function of the imaging system, extracted from the observation plane. 10% contrast occurs at 0.419 lp/mm.

maximum time-domain reflection, shown in Fig. 2.8(f). The interference effects present in the frequency domain images of Fig. 2.8(c–e) are significantly reduced in this time-domain image. From this image we extract the relationship between spatial resolution and the radius of interest, in the form of the modulation transfer function (MTF). The MTF10 criterion, based on the Rayleigh criterion, indicates the spatial frequency beyond which features cannot be considered resolved. We achieve a MTF10 of 0.419 lp/mm, at a radius of 5.693 mm, as indicated in Fig. 2.8(g). Diffraction limits for the telecentric objective at 220 and 330 GHz are also indicated, for which zero contrast occurs at 0.655 and 0.709 lp/mm respectively, according to the spatial cutoff frequency,

$$\mathrm{SCF} = \frac{1}{f/\# \times \lambda}, \tag{2.4}$$

where $f/\#$ is the f-number of the telecentric objective, and λ is the free space wavelength.

Depth Resolution

Since the system is measuring coherently over a wide bandwidth, we expect to resolve depth features at a resolution of,

$$\Delta z = \frac{2\ln 2}{\pi} \frac{c}{\mathrm{B}\left(1 - \frac{\mathrm{B}^2}{4f_c^2}\right)} = 1.25 \text{ mm}\ , \tag{2.5}$$

where c is the speed of light, $\mathrm{B} = 110$ GHz is the bandwidth of the system, and $f_c = 275$ GHz is the centre frequency [7]. For practical imaging purposes, Δz is limited to the Rayleigh length of ± 2.5 mm of the focal plane, where the beam is focused and normally incident upon the target.

2.4 Non-Destructive Testing

A range of different real-world objects are selected to demonstrate the non-destructive testing and imaging capabilities of the system; of primary interest are samples with prominent depth features and hidden objects that optical systems would fail to detect. The samples are placed at the focal plane of the lens and scanned from an elevation angle ϕ_{spot} of 0.001°–10.5°, as shown in Visualization 2, with complex S_{11} measured over 10030 equidistant points. In the same vein as the Siemens star measurements, these frequency-domain images show little useful information, and have been omitted from analysis. This is due to the aggregation of multiple reflections from the air-COC surfaces.

We first analyse the scan taken of a marshmallow with a copper wire of 1 mm diameter

inserted approximately 4 mm behind the front surface, as shown in Fig. 2.9(a). Due to the broadband nature of the acquisition, the observation plane can be moved through the sample in order to show the different features at different depth positions, as demonstrated earlier for the Siemens star target. Figure 2.9(b,c) shows the two planes of interest, both locally normalized to make the images clearer. The first plane in Fig. 2.9(b) corresponds to the reflection measured from the first air-marshmallow interface. Although this interface does not align with the focal plane, we still expect to receive strong reflections, as it lies just outside the Rayleigh length. Since the back of the marshmallow lies close to 10 mm outside the Rayleigh length, reflection magnitude is minimal and out of focus. The second plane shown in Fig. 2.9(c) reveals the hidden copper wire inside the sample. This observation plane is plotted as a surface in Fig. 2.9(d) to better show the magnitude distribution of the reflection from the wire. The reflection from the front face of the marshmallow is much stronger than the wire, as wave-propagation within the lossy marshmallow attenuates the terahertz power, evident in the change in reflection magnitude of the portions of wire inside and outside the marshmallow. Furthermore, the circular profile of the wire scatters the incident beam in many directions, decreasing reflection magnitude.

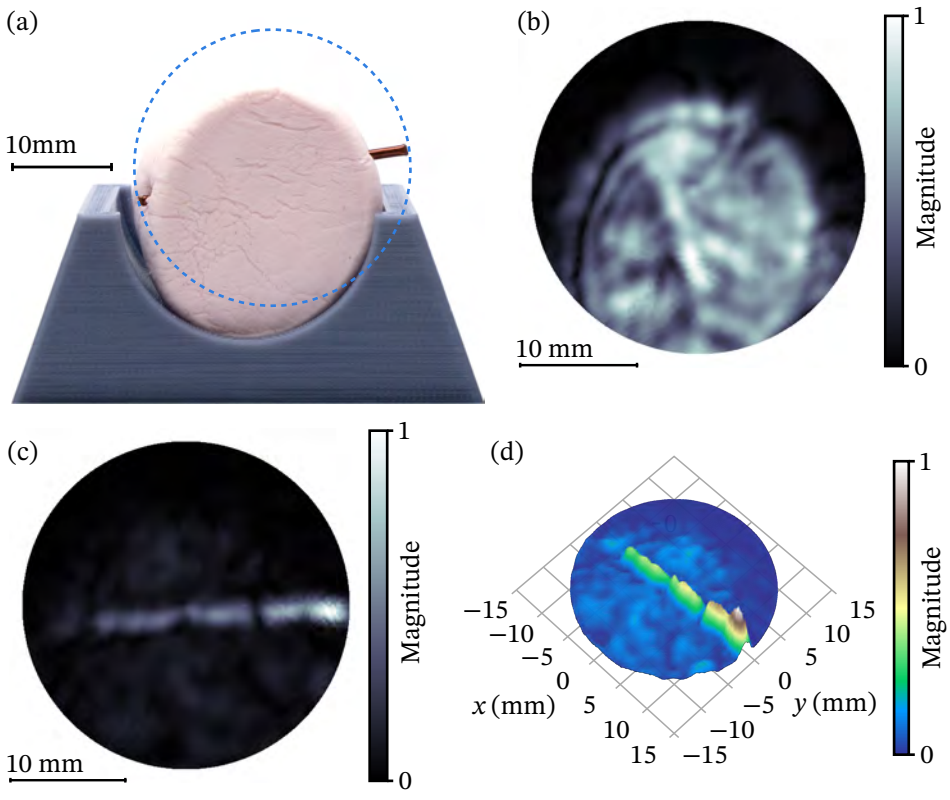

Figure 2.9: Demonstration of a food-safety application of terahertz imaging, namely the detection of a hidden wire inside a marshmallow. (a) Front view photo of the marshmallow with copper wire in 3D printed holder. (b) Observation plane at the front face of the marshmallow. (c) Weak reflection from the copper wire. (d) Contour plot differentiating the wire and the marshmallow.

We now turn our attention to imaging chocolates through the terahertz-transparent packaging shown in Fig. 2.10(a). Owing to the broadband measurement, the chocolates are resolved in the time-domain image in Fig. 2.10(b), despite the fact that the packaging is optically opaque. The strong reflection intensity and resultant high contrast from the hard sugar shell of the chocolate permits volume rendering, with Fig. 2.10(c) showing the position of some of the hidden chocolates near the focal plane in 3D-space, and their characteristic round shape.

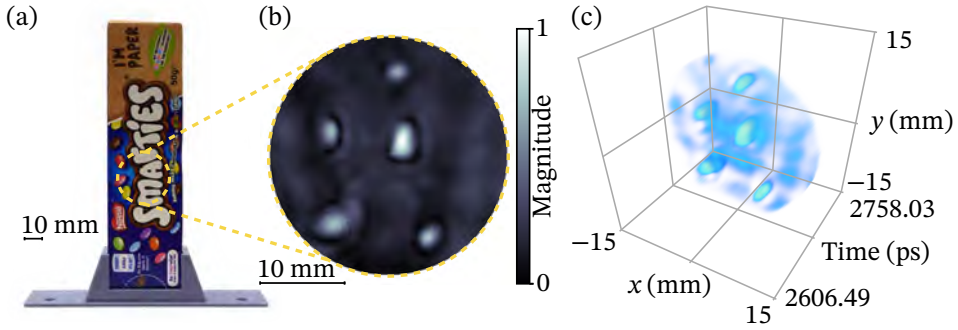

Figure 2.10: Demonstration of hidden object detection. Chocolates concealed inside a cardboard box are revealed with terahertz imaging. (a) Front view photo. (b) Observation plane showing the location of chocolates in the focal plane. (c) Volumetric render of dataset showing the locations of the chocolates in 3D space.

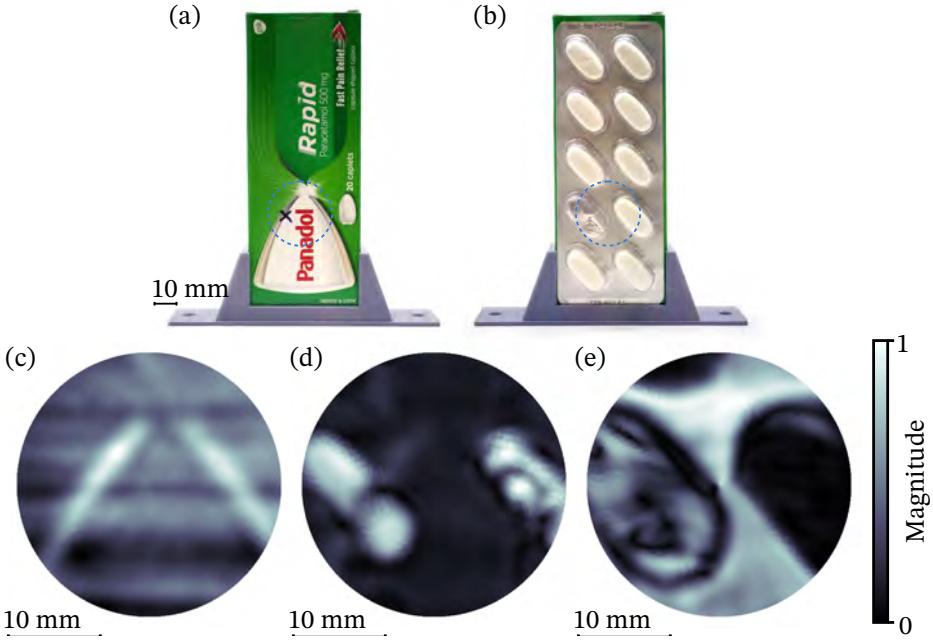

Figure 2.11: Demonstration of hidden and missing object detection. A tablet missing from a blister packet is revealed with terahertz imaging. (a) Front view photo. (b) Front view photo of blister packet outside of cardboard box to show the location of the missing tablet. (c) Observation plane showing small reflections from the metallic foil on the packaging. (d) Observation plane showing the top of the pre-formed plastic packaging. (e) Observation plane corresponding to the metallic backing of the blister packet. The stronger reflection on the left-hand side of the image indicates the missing tablet.

To extend the ideas presented in the marshmallow and chocolate demonstrations, we present the absence of a tablet inside the cardboard package shown in Fig. 2.11(a), with the location of the missing tablet depicted in Fig. 2.11(b). We move the observation plane through the sample, observing reflections from the triangular section of metallic foil on the packaging in Fig. 2.11(c), the plastic of the blister packet in Fig. 2.11(d), and the foil backing of the packet in Fig. 2.11(e). The absence of reflection on the right of Fig. 2.11(e) indicates the tablet has absorbed the incident power, so we can deduce the presence or absence of the tablet, consistent with the photograph in Fig. 2.11(b).

The three food-item imaging targets that we have investigated serve as a proof-of-concept for the hidden-object detection capabilities of terahertz imaging, showing the viability of terahertz waves for food-safety and inspection applications. However, we must emphasize that this is only true in the case of broadband imaging, due to the ability to observe reflections at the focal plane using time-domain analysis techniques, and counteract the negative impacts of interference fringes in narrowband. This is possible with the high bandwidth available with bulk COC optics. To this end, we achieve object-penetrating imaging, demonstrated by resolving wires inside marshmallows, locating chocolates inside packaging and detecting missing tablets. As such, broadband imaging techniques allow a wide range of samples to be analysed, highlighting the significance of broadband terahertz imaging systems.

2.5 Discussion

2.5.1 3D-printed Anti-Reflection Structures

To alleviate the losses incurred by Fresnel reflections at the air and COC interfaces of the Risley-prism system, the early designs include 3D-printed anti-reflection structures into the components. The two most promising methods are adding progressive index and quarter-wave matching layers. The progressive index matching scheme utilises a quintic index gradient from air to COC [186], with the refractive index controlled via the fill factor of COC and thus the ratio of polymer and air. The quarter-wave matching scheme is designed to negate reflections at the centre frequency of 275 GHz, sacrificing some of the bandwidth of the design. Despite somewhat promising simulations and test pieces, these structures were are too difficult to implement in 3D-printed COC, due to the inability of the 3D-printer to produce fine features accurately enough on the surface geometries of the lenses; It remains an avenue for future exploration.

2.5.2 Increasing Scanning Speed

The hardware of the Risley-prism scanner is designed to be low-cost and easy to troubleshoot. Consequently, the scanning times are approximately three hours, far too slow for applications such as production-line monitoring or security screening. The stepper motors used are open-loop, simplifying the control system for the prototype. To improve the scan speed, faster motors with closed-loop positional feedback are appropriate. Increasing the rotational speed of the Risley-prism also necessitates finding an alternative to the 3D-printed PLA frame, in favour of either a different material or manufacturing process, to improve rigidity and ensure structural integrity at high speeds. Involvement of mechanical engineers in such a design is critical to ensure the vibrations at high speeds are safely managed.

2.5.3 Further Evaluating Imaging Performance

Another aspect of the Risley-prism imaging system that warrants future work for commercial development is the evaluation of imaging performance. It is worth noting that the system presented in the article is intended as a prototype, without the expectation of being used in a critical situation which may require rigorous imaging specifications. Although the objective lens compensates for the central blind spot of the Risley-prism, it is mentioned in the article that the addition of a third wedge overcomes this drawback. This is likely an avenue for compromising speed and mechanical complexity in favour of greater image accuracy and quality, or vice versa. In conjunction with hardware, the software of the Risley-prism system is of interest for future development. The effects of different rotation patterns and coordinate interpolation on the final imaging results across the line of 0° and 360° have been identified as a potential issue for critical applications. This could be evaluated by over-scanning this segment of image and comparing data at 0° and 360°. Alternatively, two identical images could be acquired and compared, with one starting angle increased to 90° to ensure there is no wrapping distortion over the 0° portion of the image. This issue would primarily be dependent on manufacturing precision, and the accuracy of control system homing and rotation operations. Further testing on the reliability of the system to detect small anomalies is worth undertaking but would be dependent on the target application.

2.5.4 Further Error Analysis

Across the quasi-optical components in this thesis, there is some discrepancy between the theoretical and measured performance. Although the imaging performance of the systems is satisfactory, a deeper investigation into these discrepancies would be of interest for future 3D-printed COC components. However, performing an error analysis on a system such as the Risley-prism scanner would likely be an entire research project on its own. To provide an example scenario, the accumulated positional and tilt error across each of the four 3D-printed COC lenses would need to be considered, as well as the manufacturing tolerance which is significant since the parts are printed on FDM machines. The lenses are optimized at 220, 275, and 330 GHz, across 20 rotation configurations which map the pointing space. A rudimentary Monte Carlo sensitivity analysis on the centre frequency at a single configuration was performed in Zemax with conservative tolerances, producing the MTF plot shown in Fig. 2.12. Minor changes to optical element position and surfaces parameters result in moderate change across the MTF, indicating that deeper error analysis and design consideration is warranted.

2.6 Conclusion

Broadband beam-steering solutions are needed to replace raster scanning schemes for terahertz NDT. However, existing solutions make use of beam-steering components which are vulnerable to narrow-band interference effects or require complex apparatus requiring tedious alignment in order to achieve high quality images. To address these limitations, the Risley-prism imaging system presented in this work makes use

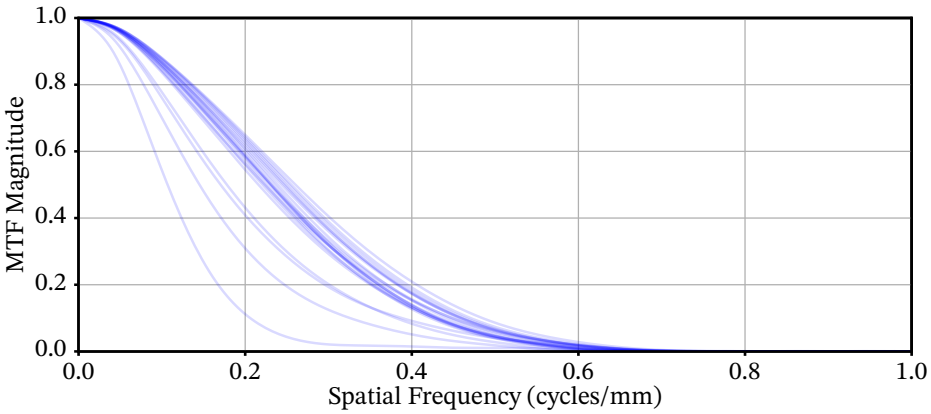

Figure 2.12: Monte Carlo tolerance analysis of the Risley-prism system in Ansys Zemax OpticStudio. Performed with a 0.2 mm tolerance for surface geometry and optic position. These results are comparable to those shown in Fig. 2.8(g).

of a simple structure and design to achieve broadband imaging with high spatial resolution. Importantly, the system delivers a scanning beam across an object plane at normal incidence to achieve maximum reflection. This is achieved by 3D-printing a custom aspherical telecentric objective, improving upon systems with spherical lenses to further enhance image quality. All the quasi-optical components are 3D-printed from COC for high operational bandwidth and low material loss considerations. Our work highlights great potential for future 3D-printed terahertz systems, with packaging and optics both conveniently manufactured at low cost in a lab environment. The simple and broadband nature of the design can be easily retrofitted to a pre-existing terahertz radar or VNA system as a drop-in beamforming front-end. Results demonstrate the ability of the system to image a variety of targets, revealing contamination, depth profiles and hidden objects in assorted food items. Future use of the system can be extended to larger scale imaging schemes for security applications or production-line monitoring, as well as far field beam-steering for broadband communications and ranging [176], by simply removing the telecentric objective.

Chapter 3

Highly Efficient Terahertz Dark-Field Imaging System with 3D-Printed Components

Abstract

Non-destructive testing and evaluation of targets with low contrast and sub-wavelength features tends to be challenging. By illuminating the target off-axis, dark-field imaging techniques can resolve diffracted or scattered features that are typically challenging to discern with conventional bright-field imaging, which relies on specular reflection exclusively. Traditional dark-field methods achieve off-axis illumination by blocking the central portion of the incident beam, but this unfortunately incurs significant power losses of up to 99%. This level of power loss is unfavourable at terahertz frequencies where source power is relatively scarce. To address this, we propose a terahertz dark-field imaging system that makes use of a double axicon beam expander to create an annular beam, which is then focused down upon the target through an objective. The system permits simultaneous bright and dark-field imaging in reflection without modifying the optical train, making greater use of raster scan time while achieving an average transmission efficiency of 33.15% and bright-field spatial resolution of 0.391 lp/mm. The proposed dark-field imaging system is able to enhance the detection of fine features such as growth rings in wood, superficial imperfections on bulk materials, and defects in fibreglass. This approach to achieve dark-field imaging will be valuable for biomedical imaging at the terahertz range that harbors interesting molecular vibration activities.

Statement of Authorship

Title of Paper	Highly Efficient Terahertz Dark-Field Imaging System with 3D-Printed Components
Publication Status	Published
Publication Details	**B. Chung**, H. Lees, M. Ibrahim, D. Headland, and W. Withayachumnankul, Journal of Physics: Photonics, vol. 7, no. 2, art.no. 025012, 7 March 2025, DOI:10.1088/2515-7647/adb81e.

Principal Author

Principal Author	Bryce Chung
Contribution to Paper	Theoretical analysis, experiment design and execution, data processing, and manuscript writing.
Overall Percentage (%)	80%
Certification	This paper reports on original research I conducted during the period of my research degree candidature and is not subject to any obligations or contractual agreements with a third party that would constrain its inclusion in this thesis. I am the primary author of this paper.
Signature	.....
Date	.....

Co-Author Contributions

By signing this Statement of Authorship, each author certifies that:

I. The candidate's stated contribution to the publication is accurate (as detailed above),

II. Permission is granted for the candidate to include the publication in the thesis; and

III. The sum of all co-author contributions is equal to 100% less the candidate's stated contribution.

Name of Co-Author	Harrison Lees
Contribution to Paper	Conceptualization, drafting
Signature	.....
Date	.....

Name of Co-Author	Matthew Ibrahim
Contribution to Paper	Conceptualization, drafting, resources
Signature	.....
Date	.....

Name of Co-Author	Daniel Headland
Contribution to Paper	Conceptualization, drafting
Signature	.....
Date	.....

Name of Co-Author	Withawat Withayachumnankul
Contribution to Paper	Conceptualization, drafting, resources
Signature	.....
Date	.....

3.1 Introduction

Many methods exist for performing NDT which make use of X-rays, visible light, magnetic fields, and ultrasonic waves. For in-situ systems, it is desirable for an imaging system to be non-ionizing to ensure the safety of operators and potential targets, in scenarios such as: security screening, biomedical imaging, and process line monitoring. The capability to penetrate optically opaque materials with non-ionizing radiation, while maintaining reasonable spatial resolution is the main advantage of terahertz waves for non-destructive testing, useful in the detection of subsurface defects in structural materials [154] and frost damage in biological samples [40]. Improvements to these techniques will therefore increase the applicability and versatility of such terahertz imaging systems. Terahertz imaging serves to complement existing NDT techniques, providing a balance between spatial resolution and object penetration. Conventional bright-field terahertz imaging typically relies upon the spatial dependence of the specular reflection or transmission across a target, measuring the change in received power as image contrast [187]. For such raster-scanning schemes, the apparatus typically involves focusing a Gaussian beam to a small spot and moving it across the sample at normal incidence, maximising the signal to noise ratio [40], [47]. To achieve high bright-field contrast at terahertz frequencies, samples should exhibit high variation in absorption across scanned areas [187]. However, incident power scattered by or transmitted through a sample will also provide contrast in reflected power. When imaging samples with uneven surfaces or intricate granules, a large portion of power is typically lost through diffraction and scattering effects [188], which are an ambiguous source of loss from the perspective of a receiver in a bright-field imaging setup. This work addresses this limitation by capturing the scattered power, and uses it to differentiate between scattered and absorbed terahertz power in a bright-field system.

Dark-field techniques are well established in the optical domain, and they address the issue of ambiguity by illuminating samples off-axis and collecting only the scattered or diffracted power [189], [190]. This capability for resolving features, which might otherwise go undetected with a bright-field scheme, is useful for terahertz imaging, where features may not be discernible with bright-field techniques [191]. Such techniques are particularly useful for surface characterization at terahertz frequencies, permitting the discernment between convex and concave surface imperfections [192], [193]. A typical dark-field setup achieves off-axis incidence by blocking the central portion of the incident Gaussian beam before passing through an objective lens [194]. This technique significantly reduces the transmitted power, as this is where the majority of the beam's power resides [187], [195], [196]. While high source power requirements may be manageable at shorter visible wavelengths, terahertz source power is modest, necessitating optical

schemes to conserve power where possible. Generally, dark-field systems in the terahertz domain are uncommon [196], and systems proposed almost exclusively aperture obstruction [187], [191], [196], significantly reducing power incident upon the target. An alternative method for off-axis illumination is to use a pair of conic lenses, known as axicons [197], to expand a collimated beam into a ring shaped, annular beam, and then focus it with an objective lens [198], [199]. This beam expansion technique is used in optical dark-field imaging [190], [195], fluorescence imaging [200], and laser machining [201].

To achieve off-axis incidence and maintain high transmission efficiency, our work realises a terahertz dark-field imaging system with a 3D-printed axicon pair for beam expansion and annular-beam generation, avoiding the use of an inefficient beam block. Placing a mirror inside the centre of the annular-beam allows for the reflected scattered and diffracted waves to be collected for dark-field imaging. Combined with low loss COC quasi-optical components, our optical train design permits terahertz dark-field imaging at an average transmission efficiency of 33.15%, improving upon the $< 1\%$ efficiency observed in the literature [192]. The low absorption of the COC components also avoids unnecessary power loss during the measurement of the low power scattered and diffracted waves. By using a vector network analyser, we simultaneously collect bright-field information, allowing for reflected bright- and dark-field images to be acquired with a single raster-scan. We wish to acknowledge that an optical scheme capable of acquiring both bright- and dark-field images has been demonstrated at visible wavelengths [189], but does not capture both images simultaneously, requiring manual reconfiguration to switch between imaging modes. In contrast, our present simultaneous bright- and dark-field system also maximizes the information collection in comparison to standard raster imaging schemes, making the best use of limited terahertz power and scan time within a single acquisition. The reflection mode of our system is also beneficial for samples with high moisture content, which has been identified as an issue for terahertz dark-field imaging operating in transmission mode [191]. In such scenarios, the low transmitted power from beam-blocking is exacerbated by the high absorption of water at terahertz frequencies. With a focal length of 47.3 mm and bright-field spatial resolution of 0.391 lp/mm, we demonstrate the capability of our design by detecting features within natural wood-grain, for future non-invasive biological imaging, and defects inflicted to fibreglass, for non-destructive testing of composite material integrity.

3.2 Design of Optical Train

The key feature of the design shown in Fig. 3.1 (a) is to launch an annular beam with a double-axicon expander, and then focus this beam onto the target for oblique incidence. In this way, the annular beam is generated by deflecting the central portion of the input Gaussian beam, rather than obscuring it with a conventional beam blocker. Since the central portion of the Gaussian beam contains the majority of the power, the double-axicon conserves the limited terahertz power. To simultaneously measure the bright- and dark-field information, we use terahertz frequency extension modules from Virginia Diodes Inc. attached to a Keysight precision network analyser to acquire complex reflection and transmission spectra across 220–330 GHz. The transceiver unit contains a directional coupler, allowing the power reflected back from the system to be measured during transmission. In the bright-field path, power that is specularly reflected from the target, which contains the low spatial-frequency information, travels back through the same lenses to the transceiver. In the dark-field path, power that is scattered from the target containing the high spatial-frequency information is collimated by the objective and directed towards a mirror placed inside the centre of the annular-beam, reflecting it 90° towards the receiver. The design of the optical train can be easily adapted to work with other systems, provided they have some form of free-space coupling.

Ray-tracing is used to design the dark-field optical train within ANSYS Zemax OpticStudio, and scalar diffraction theory simulations performed to take diffraction into consideration and validate the field distribution of the desired annular-beam. All lens components are implemented in COC, a 3D-printable polymer that features low dispersion and low loss over terahertz frequencies, advantageous for optical components [143]. While the 3D-printing process slightly increases scattering losses in comparison to traditional injection moulding techniques, 3D-printed lenses maintain reasonable optical performance in the range of 220–330 GHz, where imperfections are sub-wavelength [137]. These properties permit low chromatic aberration over the 220–330 GHz range, with no absorption peaks or molecular resonances. Refractive index $n_{\mathrm{COC}} = 1.521$ and $\tan\delta = 0.0004$ is used from previous lens design work [202].

We first design the plano-convex collimating lens to transform the quasi-spherical wavefront emitted by the horn antenna to a collimated beam, indicated by L1 in Fig. 3.1(a). The aperture of 48.5 mm accommodates a $1/e^2$ beam diameter of 40.76 mm at 220 GHz, 100 mm away from the end of the horn antenna that is attached to the transmitter. The larger aperture is left as a margin in order to avoid truncating the diverging Gaussian beam.

A double axicon expands the collimated beam into a large annular shape by first deflecting the power away from the optical axis, and then correcting the diverging beam such that it propagates parallel to the optical axis. This is done in order to fit a small, off-axis reflector inside the centre-null. To diverge the collimated beam, we use a negative axicon lens with a diameter of 46 mm and 36° incline angle as indicated by L2 in Fig. 3.1(a). This lens is placed against the first collimating lens L1. To then correct the divergence of the first axicon into a collimated annular-beam, we use a positive axicon with a diameter of 96.8 mm and identical incline angle as indicated by L3 in Fig. 3.1(a). The distance between negative axicon L2 and positive axicon L3 is chosen such that the outer diameter of the annular-beam is smaller than the lens holder's clear aperture of 96.8 mm, and so

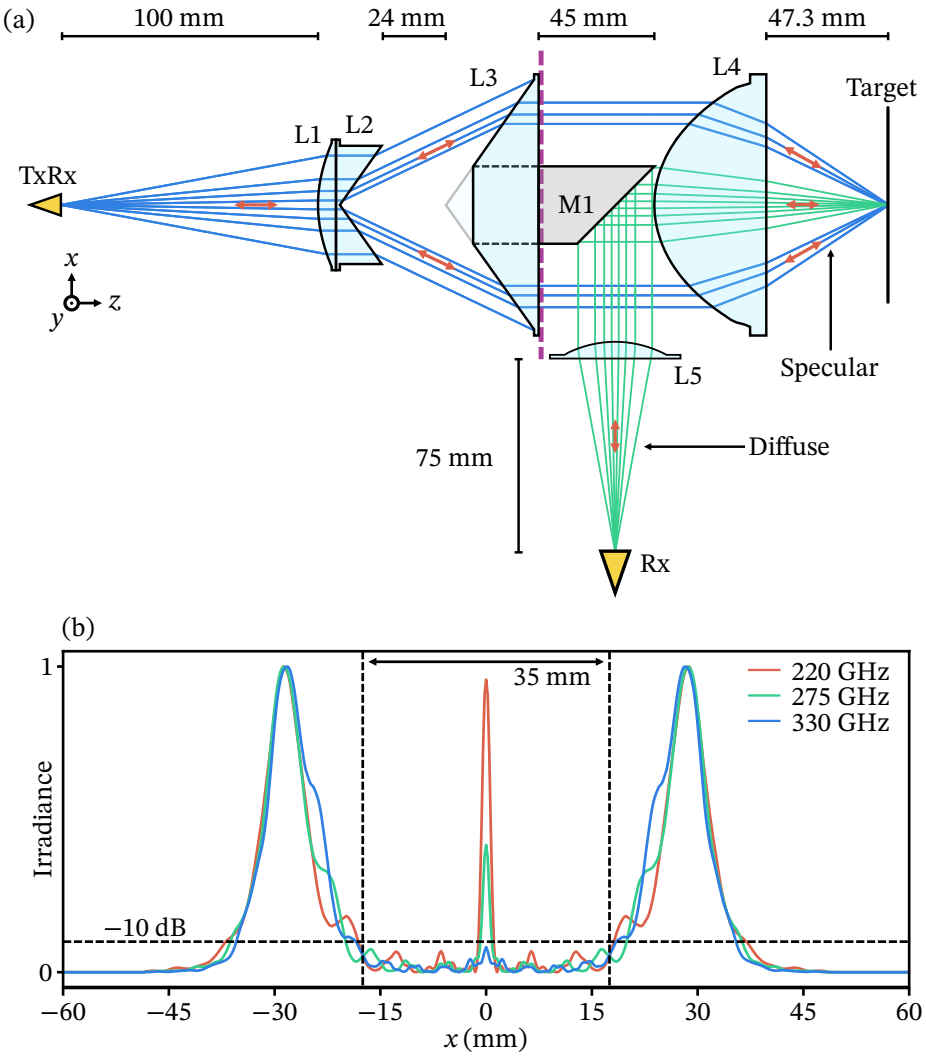

Figure 3.1: Lens train model of the imaging system. (a) Lens diagram showing the path from the transceiver to the target through L1: Horn collimating lens; L2: Diverging axicon lens; L3: Collimating axicon lens; L4: Objective lens M1: 45° mirror; L5: Collector collimating lens. (b) Cross section of collimated annular-beam, indicated by the purple dashed line, with 24 mm axicon separation, computed with the Physical Optics Propagation mode in ANSYS Zemax OpticStudio. All three frequencies have at least 36 mm centre null diameter at −10 dB.

that a mirror of 30 mm diameter can be placed inside the centre of the beam. This design optimization is performed by computing the cross section of the collimated annular beam at increasing separation distances. For a 24 mm separation between the axicons, at −10 dB from the peak of the ring, the centre null is approximately 35 mm wide at 220, 275 and 330 GHz, as shown in Fig. 3.1(b). Therefore, a 30 mm diameter cylinder is removed from the centre of the positive axicon, allowing mounting holes for the reflector to be incorporated onto the base. Since the axicon lenses are modelled as standard spherical surfaces with a near-zero radius of curvature, a small region in the centre of both axicon lenses is not perfectly conical. As such, the simulations show that a portion of the collimated beam passes directly down the optical axis, visible as a small null-central spot in Fig. 3.1(b).

For the objective lens, L4, a large aperture of 92.7 mm, and short focal length of 47.3 mm are chosen for a small spot size and steep angle of incidence on the target. The theoretical full width at half maximum (FWHM) of the focused annular-beam is [199],

$$\mathrm{FWHM} = \frac{0.36\lambda_0}{\mathrm{NA}} \,. \tag{3.1}$$

At 220, 275 and 330 GHz, the wavelength λ_0 equals 1.364, 1.091, 0.909 mm and numerical aperture NA = 0.75. Assuming approximately equal beam diameter of 70 mm from Fig. 3.1(b), the expected fwhm is therefore 0.655, 0.524, 0.436 mm respectively.

The cylindrical body of the 90° reflector is 3D-printed from PLA. Although PLA is lossy at terahertz frequencies [203], the body of the reflectors does not interact with the annular-beam, imposing no loss. A diameter of 30 mm is chosen to stay well within the centre null of the collimated annular-beam, to avoid unwanted shadowing and diffraction effects. This results in the dark-field imaging path having a numerical aperture of 0.32, limited by the diameter of the reflector. To construct the reflector, the elliptical profile is traced onto and cut from copper film with an adhesive backing. The PLA surface is sanded smooth and the copper tape is adhered to form a reflective surface. This assembly is mounted to the flat side of the positive axicon with M4 bolts. To capture the reflected waves, a plano-convex lens with an aperture of 40 mm and focal length of 75 mm is positioned off axis, focusing the scattered power to the horn antenna on the receiver unit.

3.3 Measurement of System Performance

3.3.1 Annular-beam Collimation

To ensure the annular-beam is collimated and the centre-null is compatible with the mirror, we use the near-field probe setup shown in Fig. 3.2(a) to take transmission raster scans of the xy plane at increasing distance z_d away from the tip of the reflector M1. Our raster scanning system typically requires 3.3 s/mm^2 for a mechanical step resolution of 0.15 mm. Improvements to the scan time could be made by fine tuning the control system for the scanning stage, as some sacrificial margin is typically added around the area of interest to avoid distortion from mechanical vibrations and instability during acceleration and deceleration movements. Over $z_d = 0$–60 mm, the beam stays approximately the same size, with very minor beam non-uniformity visible inside the null, which is not expected to impact performance. The beam features an approximate inner diameter of 68.09 mm and outer diameter of 94.59 mm measured at $z = 30$ mm, indicating reasonable collimation as shown in Fig. 3.2(b).

3.3.2 Focal Spot Size

In order to ensure the optical train is focusing the beam as expected, we place the objective L4 after the second axicon lens L3 and take a near-field xy raster scan of the focal plane with the apparatus shown in Fig. 3.2(c). From the plane shown in Fig. 3.2(d) we use the cross section shown in Fig. 3.2(e) to extract the FWHM spot sizes of 0.929, 0.763, 0.667 mm at 220, 275 and 330 GHz respectively. The shortening wavelength leads to this decrease in spot size, and a corresponding improvement in imaging resolution. These values approximately align with those calculated earlier, 0.655, 0.524, 0.436 mm. Some discrepancy is attributed to system misalignment and surface imperfections of the 3D-printed lenses.

3.3.3 Spatial Resolution

To assess the bright-field spatial resolution of the system, we configure the complete system as shown in Fig. 3.3(a) to image a resolution test target. Following the standard set in Chapter 2, we use the Siemens star target shown in Fig. 3.3(b) to extract the MTF from the bright-field time-domain image in Fig. 3.3(c) with the method detailed in [185]. The Siemens star features fifteen planar, triangular patches of copper, arranged in a circular pattern to form highly reflective “spokes.” We use the time-domain image here to avoid interference artifacts that are present at single frequencies, which can degrade the image. The time-domain image is obtained by performing an IFFT on the complex fre-

quency spectrum measured from 220–330 GHz, as described in [202]. As the spot moves closer towards the centre of the Siemens star, the dark-field image in Fig. 3.3(d) shows that power diffracts from the target as the spokes form a grating, corresponding to the expected decrease bright field contrast. We also note that the dark-field image resolves the subtle change in depth along the perimeter of the spokes where the edge scatters the incident wave. No information from the centre of the spokes is resolved in the dark-field image, since there are no changes in depth or absorption across the surface. The expected and opposite effect is seen in the bright-field image, where the uniform copper

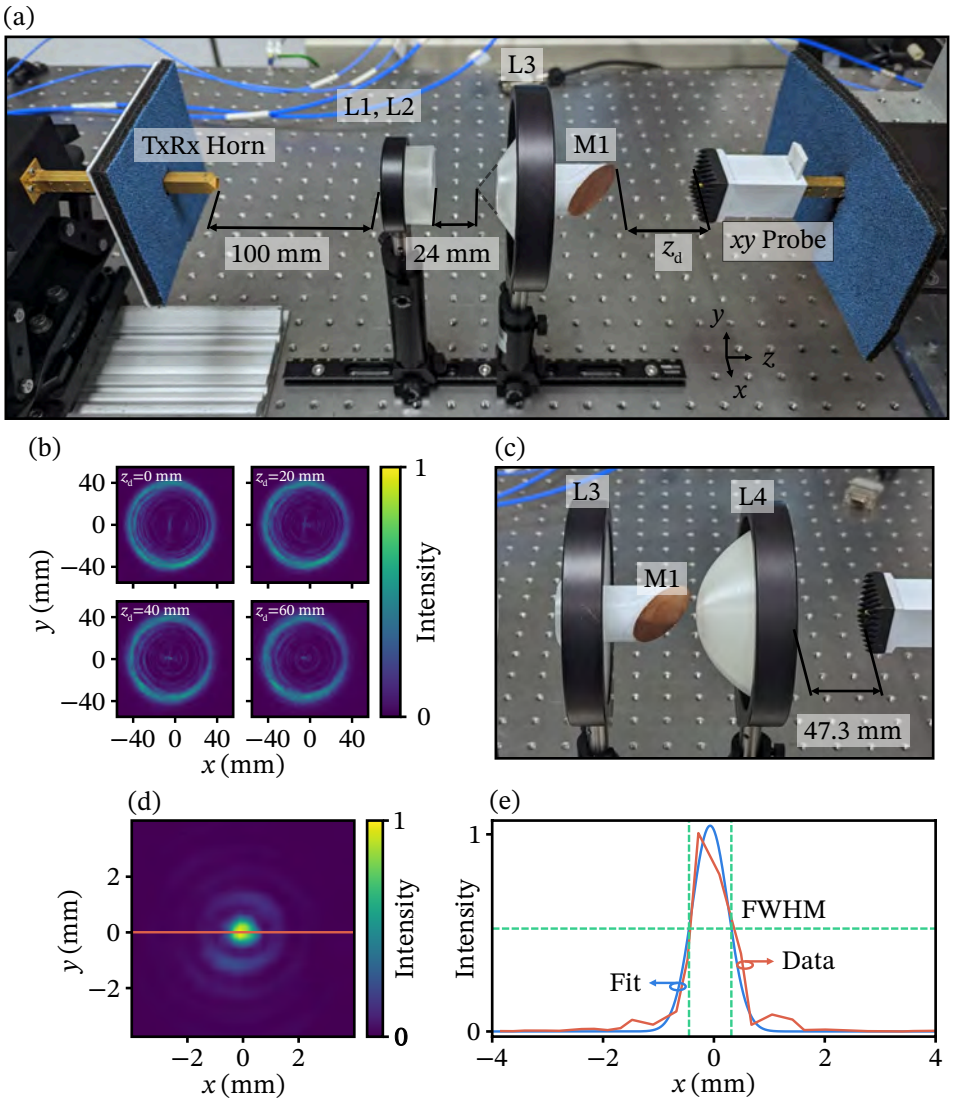

Figure 3.2: Near field scanning setup of the imaging system. (a) Photograph of scanning setup to observe the collimated annular-beam. L1: Horn collimating lens; L2: Diverging axicon lens; L3: Collimating axicon lens; M1: 45° mirror. The dark-field collector components are not included here. (b) Transmission raster scans along of the xy plane at z = 0–60 mm, showing the collimated ring at 275 GHz. (c) Photograph of the objective lens, L4, positioned after the second axicon, L3, with scanning setup to measure the spot size. (d) Transmission raster scan along the xy plane showing the location of the system focus at 275 GHz, cropped to ±4mm. (e) Cross section at $y = 0$, showing a FWHM of 0.763 mm, calculated from the fitted Gaussian curve.

regions appears bright and fine features appear darkened. The Siemens star target provides an intuitive demonstration of the expected dark- and bright-field results, showing where power is lost from the bright-field image due to scattering and diffraction. Measuring the MTF of the bright-field image at a radius of 0.1–24 mm, we obtain a MTF10 of 0.391 lp/mm and MTF50 of 0.192 lp/mm, indicated in Fig. 3.3(e). To improve the spatial resolution of the system, the dimensions of the lens components could be increased.

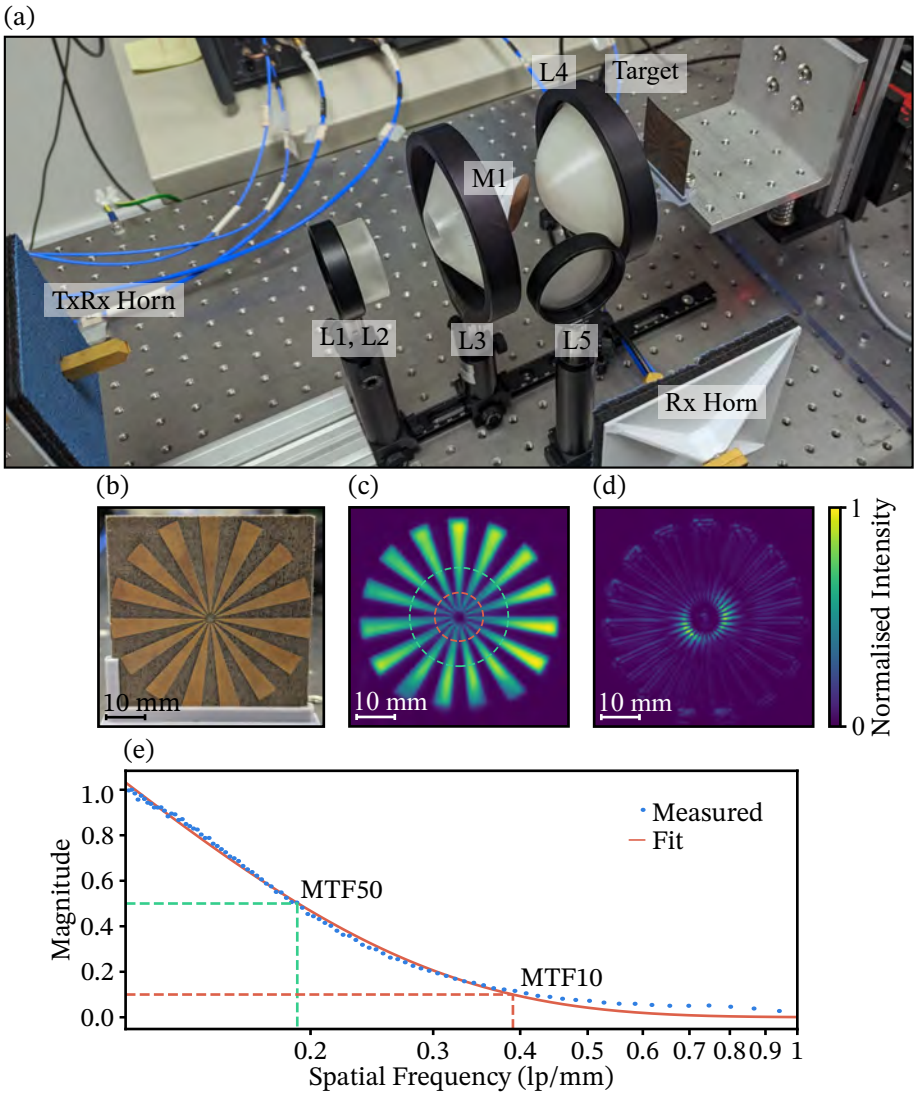

Figure 3.3: Spatial resolution test of the imaging system. (a) Photograph of the experimental imaging system with the resolution test target positioned at the focal plane of the objective. L1: Horn collimating lens; L2: Diverging axicon lens; L3: Collimating axicon lens; L4: Objective lens; M1: 45° mirror; L5: Collector collimating lens. (b) Photograph of the resolution test target. (c) Bright-field time domain image. (d) Dark-field time domain image. (e) Modulation transfer function of the bright-field scan, indicating a MTF10 of 0.391 lp/mm and MTF50 of 0.192 lp/mm.

3.3.4 Efficiency

A key motivation behind the development of the non-blocking design is to increase the power incident upon the target with the use of the axicon pair. To measure the system efficiency, we raster scan the output of the horn antenna at the location of the first lens L1, shown in Fig. 3.4(a), and compare it to the raster scan of the focal plane, shown in Fig. 3.4(b). For this measurement we use the same raster-scanning setup as Fig. 3.2(a). The raster scanning apparatus measures semi-continuously, recording the stage position when a new complex transmission measurement is available. Both scans do not share a common set of points along the x-axis, so both scans are interpolated to a common and regularly spaced Cartesian grid in order to integrate over the same number of pixels. For each of the 1000 frequencies in the span of 220–330 GHz, we integrate the intensity of the horn scan and the focus scan, and take the ratio of the two as the power efficiency for that frequency.

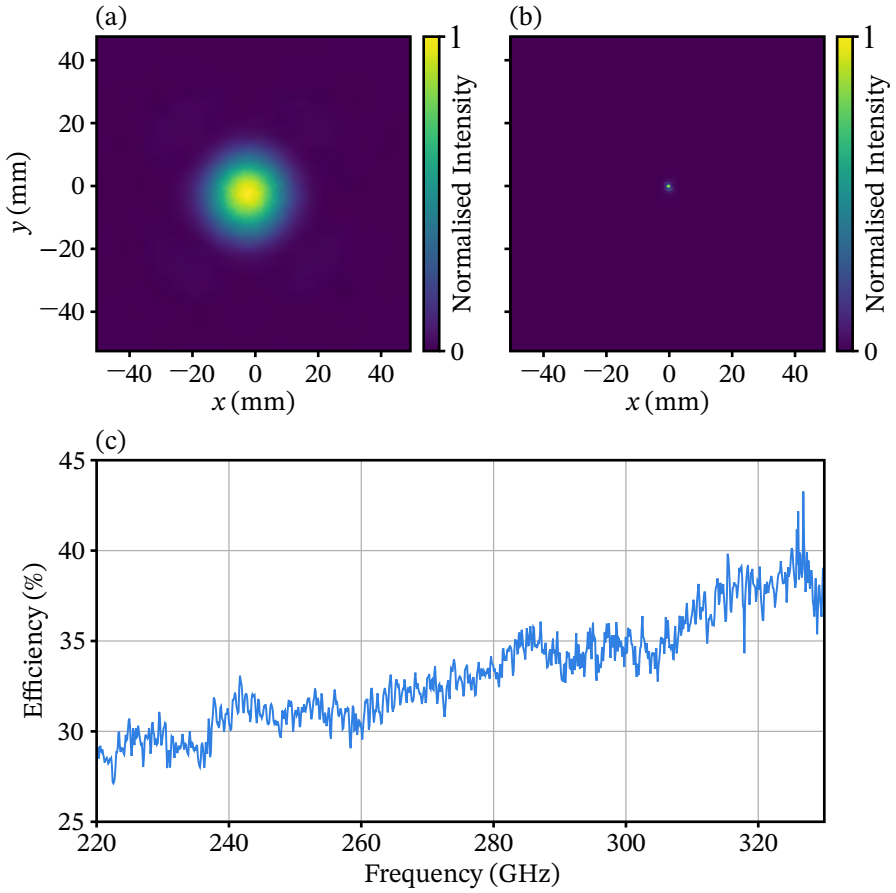

Figure 3.4: Power transmission efficiency of the optical train. (a) Transmission intensity at 275 GHz, measured 100 mm away from the horn antenna, without the dark-field system. (b) Transmission intensity at 275 GHz, measured at the focal plane of the dark-field system. (c) Percentage transmission efficiency at the focal plane relative to the horn antenna.

This result is displayed in Fig. 3.4(c), showing an increased efficiency at higher frequencies. This may be due to the beam divergence angle of the horn antenna decreasing proportional to wavelength; if the probe has minor misalignment along the optical axis, the longer Rayleigh range at higher frequency will better compensate for any error. An average efficiency of 33.15% is measured across the frequency range, lower than the 54.51% estimated in ANSYS Zemax OpticStudio, which accounts for Fresnel reflection losses. The lower efficiency is likely due to the fact that the diverging axicon is not modelled as a perfectly inverted cone but features a near-zero radius of curvature in the centre. Since the 3D-printer cannot reproduce such infinitesimal features, the apex of the inverted cone is larger than designed, which transmits more power than expected through to the centre of the collimating axicon. In the experimental setup, this additional unwanted power is blocked by the base of the reflector. Other losses are attributable to several factors including lens misalignment, lens surface roughness, and dissimilar coupling characteristics of the probe tip between the diverging horn beam and the focused spot. Despite the discrepancy between simulated and measured performance, our system still outperforms the <1% efficiency of conventional dark-field systems in the literature [192].

3.4 Demonstration of Simultaneous Bright- and Dark-field Imaging

3.4.1 Biological Sensing

To demonstrate the capture of scattered information by the dark-field imaging component of our system, we place the cut section of *Eucalyptus cladocalyx* branch shown in Fig. 3.5(a) at the focal plane of the system. We see in Fig. 3.5(b) that the bright-field image is able to capture the various growth rings from the section of branch. This bright-field image exhibits low contrast, indicating moderately uniform specular reflection across the sample. Observing the dark-field image in Fig. 3.5(c), we see a higher degree of contrast from the ring features. To exploit the merits of both modes of imaging, we clip the data to the central 95% intensity distribution of each monochrome image, map the intensity to the transparency channel of red and blue layers, and overlay the dark-field onto the bright-field to form the composite image shown in Fig. 3.5(d). While the biological origin of this scattering mechanism is outside the scope of this work, here we speculate that the interface between the lighter (less dense) and darker (more dense) regions of the wood essentially act as an abrupt change in refractive index, scattering the focused terahertz power. The red shows bright-field information, with darker regions indicating where power is lost to absorption or scattering. As expected, some of these nulls in the bright-field image are resolved as scattering in the dark-field layer, shown in blue. From these

results, the bright-field image contains the bulk of the information from the sample and the dark-field image detects subtle outlines and edges, forming a useful complimentary image capability.

3.4.2 Surface Defect Detection

To demonstrate the difficulty of imaging superficial sub-wavelength features and the enhanced contrast of the dark-field images, we present the acrylic block with several surface scratches shown in Fig. 3.6(a). An optical microscope is used to measure the approximate scratch width of 180 μm, as annotated in the inset Fig. 3.6(b). Since the acrylic substrate is smooth and flat, we expect the bright-field image to contain a high amount of reflected terahertz power. This is evident in Fig. 3.6(c), where the majority of the scanned area is brighter. The small feature size relative to the spot size makes the scratches difficult to distinguish, as the change in reflected power across the scratches is low. The dark-field image in Fig. 3.6(d) shows improved contrast, as the background level of scattered power from the smooth and flat substrate is low. This comparison demonstrates where the dark-field imaging is the most effective, for highly reflective targets which suppress the features of interest in a traditional bright-field scheme.

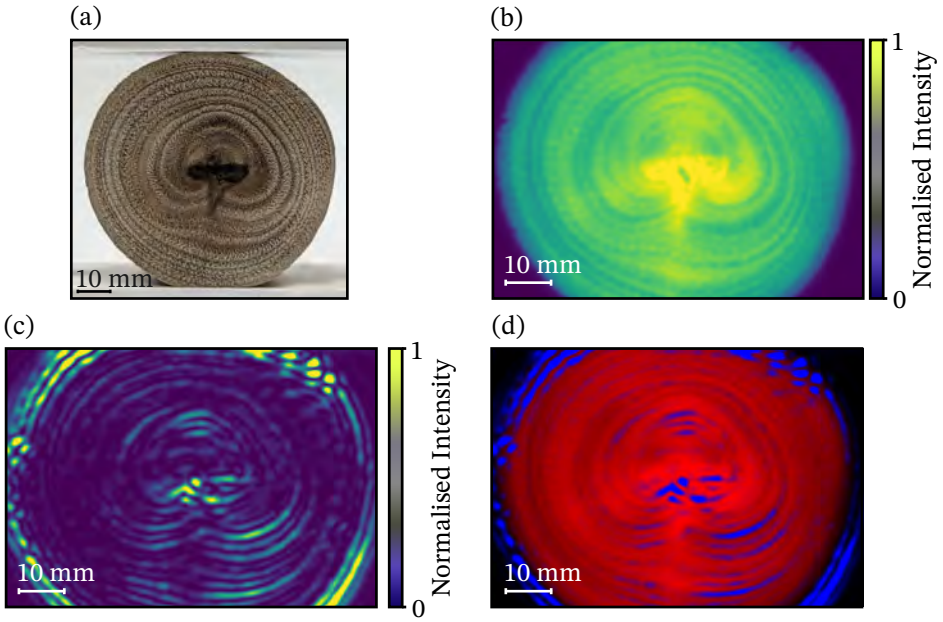

Figure 3.5: Detection of growth rings in cut *Eucalyptus cladocalyx* branch. (a) Photograph of the tree branch cross section. (b) Bright-field time domain image. (c) dark-field time domain image. (d) Composite image of bright and dark-field images mapped to red and blue colour channels respectively. We clip both images to the central 95% intensity distribution of data and map the intensity to the alpha channel of red and blue colour mattes, overlaying the dark-field onto the bright-field to form the composite.

3.4.3 Defect Detection in Composites

Since NDT of composite materials is a promising area for terahertz imaging technologies [154], we demonstrate the detection of intentionally introduced defects in two samples: a fibreglass and resin laminate block, shown in Fig. 3.7(a), and an aluminium honeycomb and carbon fibre sandwich panel, shown in Fig. 3.8(a). The fibreglass sample highlights the potential of the dark-field methodology for sub-surface feature extraction, offering additional insight into material composition beyond standard bright-field imaging. To simulate air-filled delaminations, holes of 1.0, 1.5, and 3.0 mm are drilled through the fibreglass block [154]. The block is placed in the imaging system, with the holes approximately at the focal plane. Scans are conducted using both vertical and horizontal polarizations to account for potential anisotropic material properties, with horizontal polarization achieved by introducing waveguide twists before both horn antennas

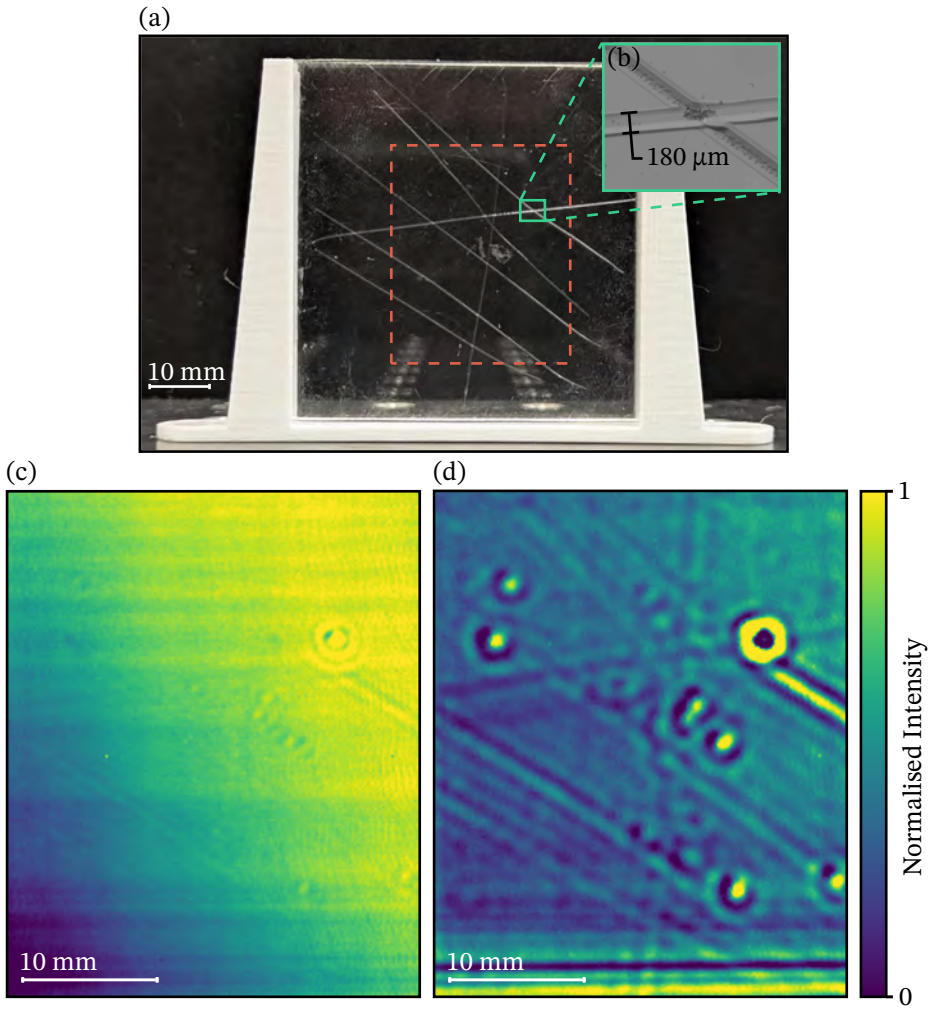

Figure 3.6: Detection of surface defects on acrylic substrate. (a) Photograph of the acrylic slab with several surface scratches. (b) Optical micrograph of surface defect, indicating the scratch defects are approximately 180 µm in width. (c) Bright-field time domain image. (d) Dark-field time domain image. We clip both images to the central 98% intensity distribution of data to remove any outliers.

and realigning the system. The three holes are detectable in the bright-field images in Fig. 3.7(b) and Fig. 3.7(c) as the terahertz waves are reflected at the fibreglass and air interface. Some vertical background artifacts are present, which we attribute to the glass fibre matrix. Notably, complementary regions are discernible in the bright-field images, with certain areas reflecting more strongly in vertical polarization and others in horizontal, suggesting polarization dependence due to the sample's construction. The dark-field images in Fig. 3.7(d) and Fig. 3.7(e) show strong scattering from the defects, with the vertical polarization showing the defects more clearly. This indicates a stronger scattering effect is present when using horizontal polarization, in agreement with the stronger contrast of the bright-field image seen in Fig. 3.7(b). Drawing conclusions on the nature of the internal fibre composition is outside the scope of this work, but we believe the acquisition of the dark field information is not negligible, and may aid in discerning the orientation of internal composite materials.

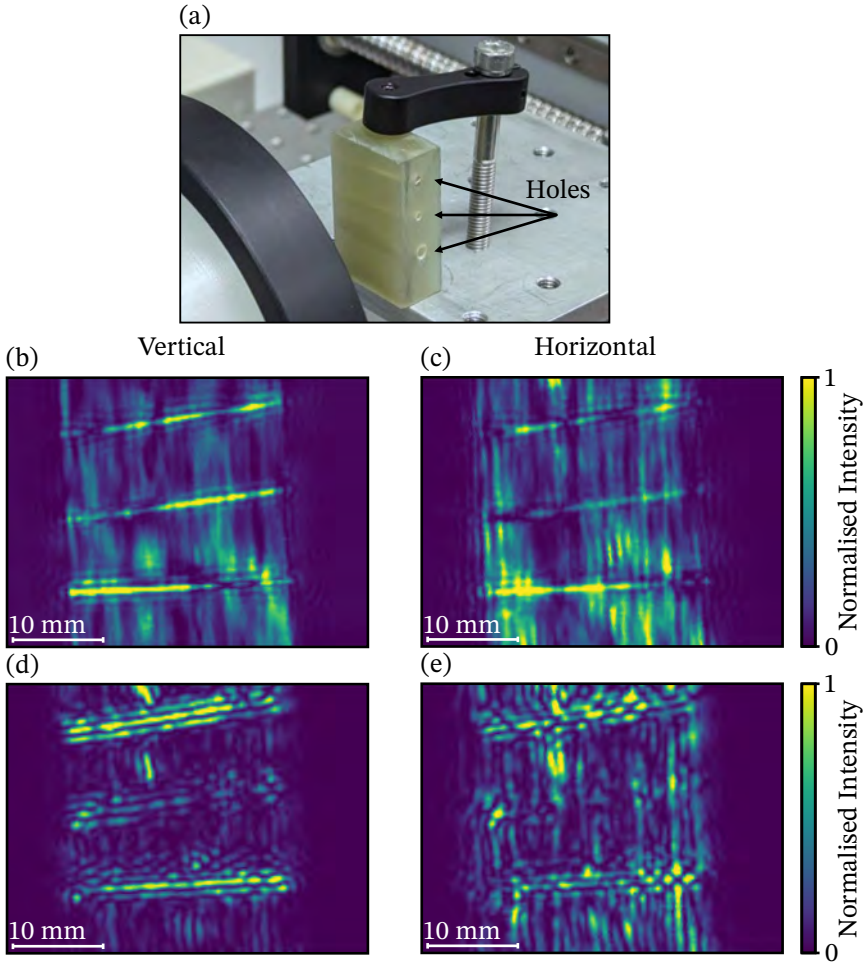

Figure 3.7: Defect detection in fibreglass block. (a) Photograph of the fibreglass sample on the scanning stage, with drilled holes aligned horizontally. (b) Bright-field time domain image with vertical polarization. (c) Bright-field time domain image with horizontal polarization. (d) Dark-field time domain image with vertical polarization. (e) Dark-field time domain image with horizontal polarization. We clip all images to the central 98% intensity distribution of data to remove any outliers.

To further demonstrate the improved detection of composite surface defects with dark-field imaging, the carbon fibre panel in Fig. 3.8(a) undergoes a three-point bend test, where mechanical force is applied to the central region of the panel. The test fractures the carbon and resin composite, with the fracture faintly visible in Fig. 3.8(a). We place the panel in the imaging system, with the surface at the focal plane. The bright-field image in Fig. 3.8(b) shows a reduction in reflected terahertz power around the area of the defect, likely due to surface deformation and subsequent deflection of the reflected beam at the conductive carbon surface. The dark-field image in Fig. 3.8(c) shows a reduction in scattered power at the location of the fracture, indicated by the darker vertical region. The dark-field image better localizes the fine fracture feature, while the bright-field image remains useful in finding the defect's approximate location. These two composite

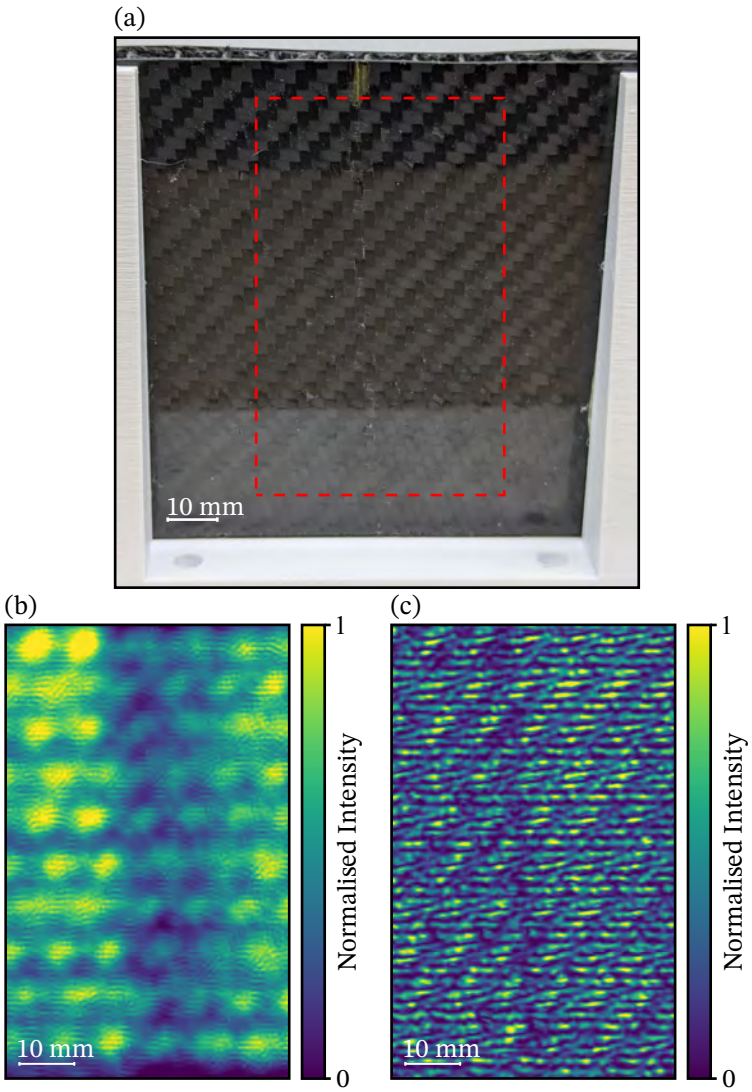

Figure 3.8: Defect detection on carbon fibre panel which has undergone a three-point bend test. (a) Photograph of the panel, with the vertical fracture approximately in the centre. (b) Bright-field time domain image. (c) Dark-field time domain image. We clip both images to the central 98% intensity distribution of data to remove any outliers.

samples show that although the bright-field method alone can detect and localize subsurface and superficial defects, the dark-field images provide additional insight into the nature of these defects and improves localization for surface features.

3.4.4 Crystalline Identification

The detection of illicit substances within postal facilities has been identified as an application suited for terahertz technology [16]. Many such substances have spectral fingerprints in the terahertz range, allowing terahertz TDS systems to classify chemical composition. The scattered power received from the crystalline target is proportional to the grain size, which permits dark-field techniques to assess the granularity [16]. The low received power and hence low signal to noise ratio of dark-field imaging inhibits accurate terahertz measurement at higher frequencies. In future work, by including the bright-field imaging path in our system, we hope to simultaneously perform parameter extraction in reflection mode, whilst maintaining the dark-field imaging system for the localization of crystalline substances. Figure 3.9(a) shows a photograph of an envelope concealing two sachets of sugar, with the leftmost having its contents replaced with finer "caster" sugar. By placing the envelope at the focal plane and acquiring an image, we reveal the sachets in both the bright- and dark-field images, shown in Fig. 3.9(b) and Fig. 3.9(c) respectively. The bright-field image shows a great degree of variation over the two sachets, providing limited information about their contents. On the other hand, the dark-field image shows a more uniform scattering profile, with the rightmost sachet containing larger granules showing an increase in scattered power as expected. This sample serves to reinforce the idea that the dual imaging modes of our system complement each other, providing additional information where one mode may not be as suitable.

3.5 Conclusion

Efficient systems are needed for terahertz imaging applications to conserve and concentrate the limited available power over a wide bandwidth. For targets with features that are sub-wavelength or have low index contrast such as indentations and bubbles, dark-field techniques are generally more suitable than bright-field ones, but traditional dark-field setups suffer from low power transmission. By using a double-axicon beam expander, we increase the terahertz power at the target, from $< 1\%$ with a typical setup [192] to an average of 33.15% with ours. Further efficiency gains can be achieved with anti-reflective coatings, more precisely made optical components, and better alignment. We demonstrate a terahertz imaging system for the simultaneous acquisition of bright and dark-field images, observing the contrast in dark-field due to scattering from growth rings

in wood, hidden crystalline substances, and defects in composite and bulk materials. These samples show an improved contrast for fine sub-wavelength features when using dark-field imaging, especially in scenarios where such features are superficial and do not strongly vary in reflectivity. It is worth noting that, for the results obtained with the dark-field system, their interpretation is the direct result of speculative assessment given previous terahertz NDE experience. The assistance of subject-matter experts, such as those in the wood and forestry industry in the case of the branch cross-section, would be necessary to provide more detailed and substantial claims on the underlying scattering physics. Scope remains for future work in investigating the scattering mechanisms for the composite materials and their polarization dependence. The experimental demonstrations included in this work intend to show that this system will likely permit improvements to terahertz imaging systems, especially those used for imaging samples which have proven challenging with traditional bright-field techniques. We believe samples with high mois-

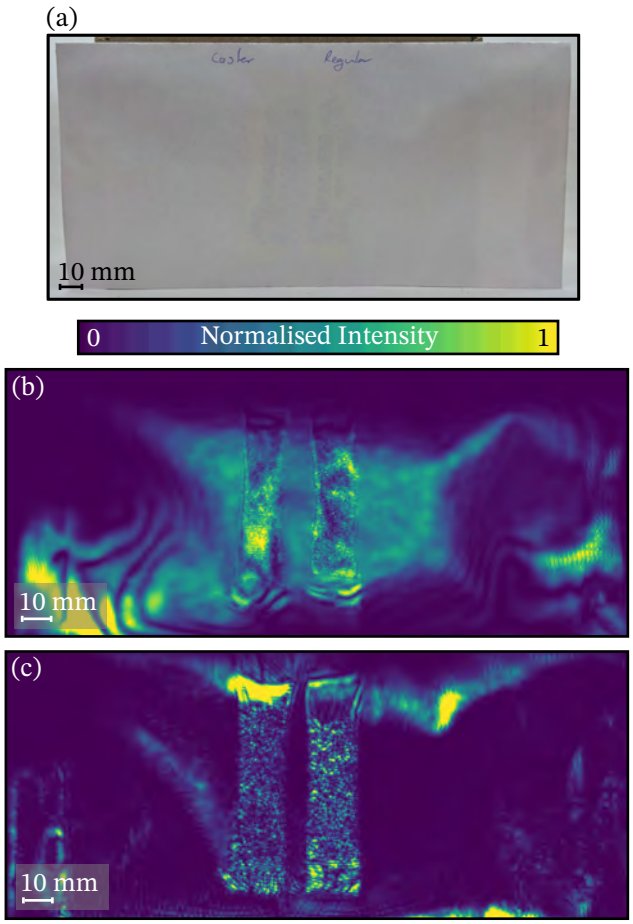

Figure 3.9: Detection of concealed granular substance in paper envelope. (a) Photograph of the envelope, with the sachets containing caster and regular sugar slightly visible through the paper. (b) Bright-field time domain image of the envelope. (c) Dark-field time domain image of the envelope. The smaller grain size of the caster sugar scatters less terahertz power, as is evident in the dark-field image. We clip both images to the central 98% intensity distribution of data to remove any outliers.

ture content or lossy materials, along with low index contrast will benefit most, such as biological tissues or composite materials.

Chapter 4

Non-contact Probing of Active Semiconductor Devices Using Terahertz Waves

Abstract

Terahertz waves are sensitive to changes in free carriers within semiconductor materials. To date, research in this area has focused on spectroscopic analysis of exposed wafers and inactive devices. In principle, terahertz waves should be able to probe packaged and active semiconductor devices subjected to bias signals, which induce changes in the carrier density across a PN junction. A challenge lies in a discrepancy between the probing spot size on the order of millimetres at 275 GHz, and the sub-wavelength footprint of a PN junction, which results in small changes of any reflected terahertz waves. Although normally buried underneath the phase noise of the terahertz oscillator, these minuscule changes in carrier density can be observed as a baseband signal in complex reflection measurements using a homodyne quadrature receiver. Due to the high sensitivity of this transceiver, sub-wavelength targets can be effectively monitored with conventional terahertz optics. These experimental results demonstrate the ability of terahertz waves to non-invasively monitor semiconductor device activity without physical contact. We anticipate that this work will be a precursor for non-destructive inspection of chips during production and the covert monitoring of operational devices.

Statement of Authorship

Title of Paper	Non-contact Probing of Active Semiconductor Devices Using Terahertz Waves
Publication Status	Published
Publication Details	**B. Chung**, H. Lees, J. Hesler, C. Chuengsatiansup, and W. Withayachumnankul, IEEE Journal of Microwaves, vol. 6, no. 2, pp. 324–333, 17 March 2026, DOI:10.1109/JMW.2026.3653411.

Principal Author

Principal Author	Bryce Chung
Contribution to Paper	Theoretical analysis, experiment design and execution, data processing, and manuscript writing.
Overall Percentage (%)	80%
Certification	This paper reports on original research I conducted during the period of my research degree candidature and is not subject to any obligations or contractual agreements with a third party that would constrain its inclusion in this thesis. I am the primary author of this paper.
Signature	.....
Date	.....

Co-Author Contributions

By signing this Statement of Authorship, each author certifies that:

I. The candidate's stated contribution to the publication is accurate (as detailed above),

II. Permission is granted for the candidate to include the publication in the thesis; and

III. The sum of all co-author contributions is equal to 100% less the candidate's stated contribution.

Name of Co-Author	Harrison Lees
Contribution to Paper	Conceptualization, drafting
Signature	.....
Date	.....

Name of Co-Author	Jeffrey Hesler (deceased)
Contribution to Paper	Conceptualization, experiment design, drafting

Name of Co-Author	Chitchanok Chuengsatiansup
Contribution to Paper	Conceptualization, drafting, resources
Signature	.....
Date	.....

Name of Co-Author	Withawat Withayachumnankul
Contribution to Paper	Conceptualization, drafting, resources
Signature	.....
Date	.....

4.1 Introduction

The effects of charge carrier injection on the electromagnetic properties of silicon have been thoroughly studied [204] and terahertz testing of semiconductor materials has been conducted since the inception of terahertz TDS [9]. This early research sought to find suitable materials to build terahertz components, to support the development of electronic systems operating in the terahertz range, between 0.1 and 10 THz [3]. Due to wavelength, terahertz waves are sensitive to free carriers but not the crystalline structure in semiconductors [205]. The carrier density and carrier mobility of semiconductors are relevant to the plasma frequency and damping rate, which for moderately doped semiconductors falls into the terahertz region. To date, a large number of terahertz spectroscopic studies have been conducted on homogeneous semiconductors over a broad range of doping levels [12], [206], [207], [208], [209], [210], [211]. Terahertz near-field nanoscopy has been applied to unbiased transistors to reveal their doping profiles, showing terahertz waves are more sensitive than infrared waves for a typical range of carrier concentrations between 10^{16} and 10^{19} cm^{-3} [11], [212], though the use of an oscillating probe requires physical access to the semiconductor. Extending the concept of TDS, terahertz ellipsometry has been used to spatially map the conductivity, carrier density, and carrier mobility of silicon carbide wafers [213]. Using optical-pump terahertz-probe (OPTP) spectroscopy, both organic and inorganic semiconductors were subject to an optical stimulus above their energy band gap to further study carrier dynamics, particularly the recombination time [214], [215], [216], [217]. In laser emission terahertz microscopy (LTEM), femtosecond laser pulses were fired at exposed semiconductor chips, which, through a nonlinear response, generates bursts of terahertz waves [218], [219]. These terahertz spectroscopic studies were not conducted with active semiconductor devices under their normal operation conditions, and require devices be physically exposed for electrical contact or near-field coupling, not amenable for non-destructive testing of active devices. For the purpose of this work, we define active semiconductor devices as those typically subject to applied voltage bias.

In this article we study the behaviour and properties of packaged semiconductor devices in the low- or sub-terahertz region due to electrical stimulus during low frequency operation. The physical size of carrier-active sites within devices are typically sub-wavelength over the WR3.4 band of 220–330 GHz, necessitating sensitive detection schemes to observe the changes in the reflected terahertz spectra. Although a VNA configuration is highly sensitive, the sampling rate and bandwidth is too low to observe a sideband modulated onto a reflected terahertz wave by rapidly oscillating charge carriers. In addition to sampling challenges, weak sidebands close to a terahertz carrier are typically difficult to resolve due to the poor phase noise performance of multiplier-based terahertz sources.

To overcome these challenges, we opt for a highly sensitive down-mixing scheme in the form of a homodyne quadrature receiver, permitting real-time acquisition of reflected terahertz sidebands, down-mixed to baseband relative to the terahertz carrier. In this work we observe a moderately strong response from carrier injection or depletion within the PN junction of a diode, due to the sensitive detection system and the strong electron plasma resonance over 220–330 GHz. This is observable in our prior preliminary work [220]. We show this phenomena is valid for a variety of semiconductor components, and also confirm that the modulation effects are not thermo-optic in nature.

4.2 Low Frequency Operation

A PN junction relies on the interaction of carriers between an N-type semiconductor and a P-type semiconductor, each doped to increase the number of electrons (in the N-type) or holes (in the P-type) in the material [221]. Under forward-bias conditions, the depletion region of a diode narrows and current flows through the device, transported by majority carrier drift. This phenomena is commonly leveraged to realize silicon optical modulators [222] and programmable terahertz metamaterials [223], both of which demanded customized waveguide or antenna designs to enhance the effects to the interacting waves.

4.2.1 Fresnel and Drude Modelling

At the forward-bias condition, there is sufficient increase in the carrier concentration for the material to take on conductive properties [224]. For this work, a 1D PN junction model in COMSOL multiphysics [225] is used to calculate the voltage dependent electron and hole concentrations at the centre of the junction, which are shown in Fig. 4.1(a). We note that the concentrations are equal due to identical acceptor and donor concentrations. The applied voltage V_a is stepped from 0–2 V_{DC}, over 50 points. We use a Drude model to describe the response of injected free carriers to an incident terahertz waves according to the complex permittivity function [208], [226]

$$\varepsilon_{\mathrm{D}} = \varepsilon_{\infty} - \frac{\omega_{pe}^2}{\omega^2 + i\gamma_e\omega} - \frac{\omega_{ph}^2}{\omega^2 + i\gamma_h\omega}\,, \tag{4.1}$$

where $\varepsilon_{\infty} = 11.7$ is the dielectric constant of silicon, ω is the angular frequency of the terahertz wave, $\gamma_x = q/m_x^*\mu_x$ is the inverse carrier collision time, and $\omega_{px} = \sqrt{N_x q^2/\varepsilon_0 m_x^*}$ is the plasma frequency, with subscripts $x = e, h$ denoting electrons and holes. q denotes the fundamental charge, $m_e^* = 0.26m_e$ and $m_h^* = 0.38m_e$ are the effective electron and hole masses in silicon [226], $\mu_e = 1364.7\ \mathrm{cm^2V^{-1}s^{-1}}$ and $\mu_h = 465.7\ \mathrm{cm^2V^{-1}s^{-1}}$ are

the carrier mobilities in silicon [225], and N_x is the carrier concentration. The applied voltage, electron and hole mobilities, and the voltage dependent electron and hole concentrations are exported from COMSOL into a Python script for use within the Fresnel model. The carrier mobility is approximated using a method [227] which assumes the mobility is dependent on the temperature and dopant concentrations [228].

Figures 4.1(b) and 4.1(c) display the simulated relationship between bias voltage and complex permittivity components over 0.1–1.0 THz. As the bias voltage reaches approximately 0.5 V_{DC}, the PN junction approaches a conductive state and the complex per-

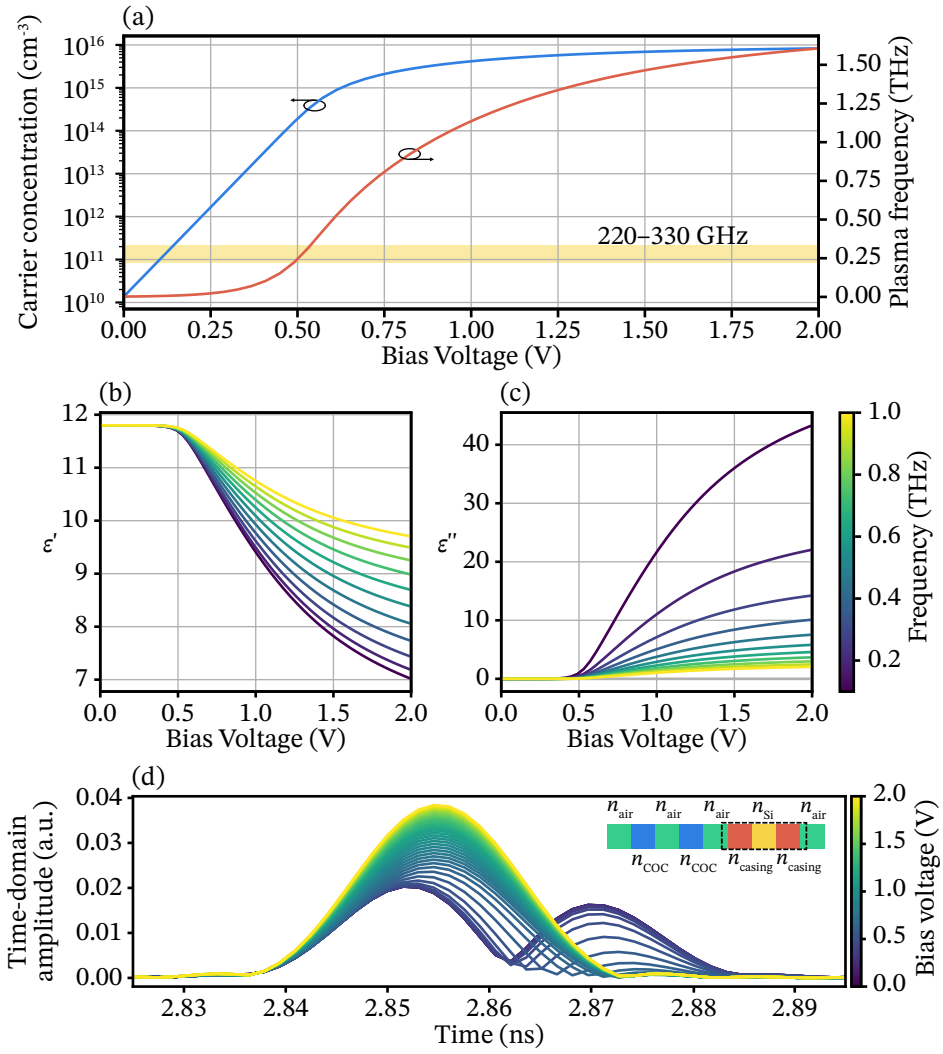

Figure 4.1: Simulation of terahertz interaction with free carriers in the PN junction. (a) Simulated electron and hole concentration over bias voltage steps, equal at the centre of the depletion region, and the resultant calculated electron plasma frequency. (b) Real and (c) imaginary components of the permittivity at the centre of the depletion region. (d) Absolute amplitude of calculated terahertz time-domain signals with a bandwidth between 220 and 330 GHz upon reflection from a packaged PN junction over bias steps of 0–2 V_{DC}, with the peaks corresponding to the reflections from the air, diode casing, and silicon interfaces. The inset shows the configuration used for the Fresnel model calculations, where refractive indexes n_{air}=1, n_{COC}=1.53, and n_{casing}=1.5, and the distances used to construct the model are [210, 15, 80, 43.546, 47.9, 0.25, 0.5, 0.25, 100] mm.

mittivity changes abruptly as the excess of majority carriers diffuse across the narrowed depletion region. This sudden change coincides with the plasma frequency exceeding the frequency of the incident wave as the carrier concentration increases. We observe a stronger response at the lower end of the frequency range as the electron plasma resonance tapers off proportionally to the total number of injected carriers [229], as shown in Fig. 4.1(a). This frequency-dependent response is evident in the swing in complex permittivity in Fig. 4.1(b) and Fig. 4.1(c), where the deviation from the intrinsic values at zero-bias is greater at lower frequencies. This in turn causes the material to take on more reflective properties, as a material will exhibit metal-like properties at frequencies below the plasma frequency, and exhibit dielectric-like properties above the plasma frequency [229]. We further demonstrate this effect in Fig. 4.2 by calculating the reflectivity [179] of the centre of the PN junction in air, using the complex permittivity calculated in Fig. 4.1(b) and Fig. 4.1(c).

Having established a simplified model of the complex permittivity of the PN junction, we turn our attention to modelling the quasi-optical system used in this work, for which we employ a frequency-domain Fresnel interference model [7] to calculate the time-domain response of a PN junction with varying carrier concentration. For this model we make the assumption that the plane-wave model should be sufficient for the system operating close to the diffraction limit, where the interaction is mostly limited to the material of interest, in this case the depletion region of a PN junction. Neglecting Fabry-Perot reflections, we model the complex spectrum from multiple interfaces and their response according to the method detailed in [7]. An inverse Fourier transform is applied to the spectral response to resolve the time-domain; this method is analogous to measuring the complex S_{11} with the VNA to recover the time-domain. The model follows a collimator

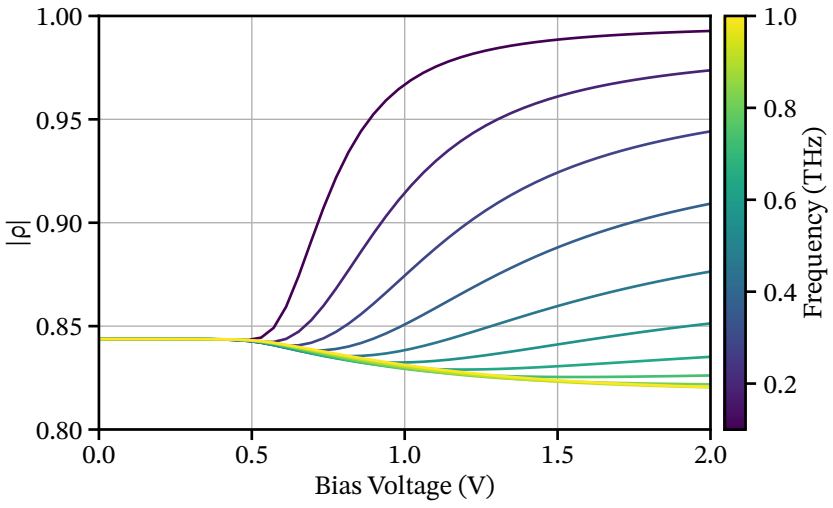

Figure 4.2: Change in reflectivity of modelled material between 0.1–1 THz. Fresnel reflectivity coefficient for a normally incident wave incident upon the material modelled by Fig. 4.1(b) and (c), referenced to a refractive index of 1.

and objective lens setup, used to focus the terahertz beam down onto the diode which is modelled as silicon encapsulated by plastic. Fresnel coefficients are computed at defined material interfaces as illustrated by the inset of Fig. 4.1(d), with the reflected time-domain response calculated at each bias voltage. From structural information obtained via X-ray computed tomography, the physical structure of the diode is simply modelled as a one dimensional, multi layer device, with an inner 0.5 mm thick silicon layer encapsulated by 0.25 mm plastic casing layers.

The modelled PN junction approximates that of the rectifier diode, as the actual doping profiles are proprietary and thus unknown. As such, we do not expect the model to agree perfectly with experimental results, but instead exhibit a highly similar response due to carrier injection and depletion. We note that the model assumes a bandwidth of 110 GHz as used in the experimental setup, indicated by the yellow region of Fig. 4.1(a), and a uniform depletion region across the PN junction.

We evaluate this model over the same 50 point bias voltage steps using in Fig. 4.1(a), computing a time-domain trace at each bias voltage and thus carrier concentration values for the PN junction. The time-domain representation of the shallow diode surfaces is smeared into two main peaks due to the depth resolution of 1.25 mm [7], limited to the bandwidth capability of the experimental system. Observing the portion of the time-domain corresponding to the diode, we show in Fig. 4.1(d) a positive change in reflection at the casing-silicon interface of the diode, and a corresponding negative change in reflected power off the silicon-casing interface. The front reflection increases with bias voltage and effectively shadows the back interface at approximately 2.87 ns in the time-domain. Overall, this trend is a result of increasing conductivity of the silicon with increasing bias voltage.

4.2.2 Experimental Validation

To experimentally validate this model, a 1N4007 silicon rectifier diode is exposed to focused terahertz waves through 3D-printed COC collimator and objective lenses shown in Fig. 4.3(a) and Fig. 4.3(b), with a $1/e^2$ spot size of approximately 1.3 mm at 275 GHz, and an expected sub-millimetre depth of focus [230]. For the quadrature receiver shown in Fig. 4.3(a), a WR3.4 TxRx vector network analyzer extender (SNR) from Virginia Diodes Inc. attached to a Keysight N5222B VNA is used to multiply high-frequency signals in the range of 9.1–18.4 GHz up to 220–330 GHz, and down-mix them to an intermediate frequency of 279 MHz for demodulation. Two terahertz signals are generated inside the SNR to achieve this; one, a RF signal at the terahertz carrier frequency to be transmitted, and two, a local oscillator (LO) offset from the terahertz carrier by 279 MHz.

As an example, to probe the target at 275 GHz, a 275 GHz RF signal is generated by the SNR to both probe the target and serve as a reference, and the 275.279 GHz LO is generated to down-mix the RF signals to the intermediate frequency (IF) frequency. The two copies of the LO are fed into down-converting mixers, one with the original RF signal to serve as a reference, and the other with the transceived RF signal containing any static reflections from lenses, reflective interfaces, and modulation from the target. This produces two 279 MHz signals at the output of the SNR; the 'Ref' which acts as an intermediate LO and the 'Meas' which acts as an intermediate RF. These LO and RF signals are each amplified by a MiniCircuits ZFL-500HLN low noise amplifier and drive a SigaTek QD54A10 in-phase and quadrature (IQ) demodulator. The demodulator

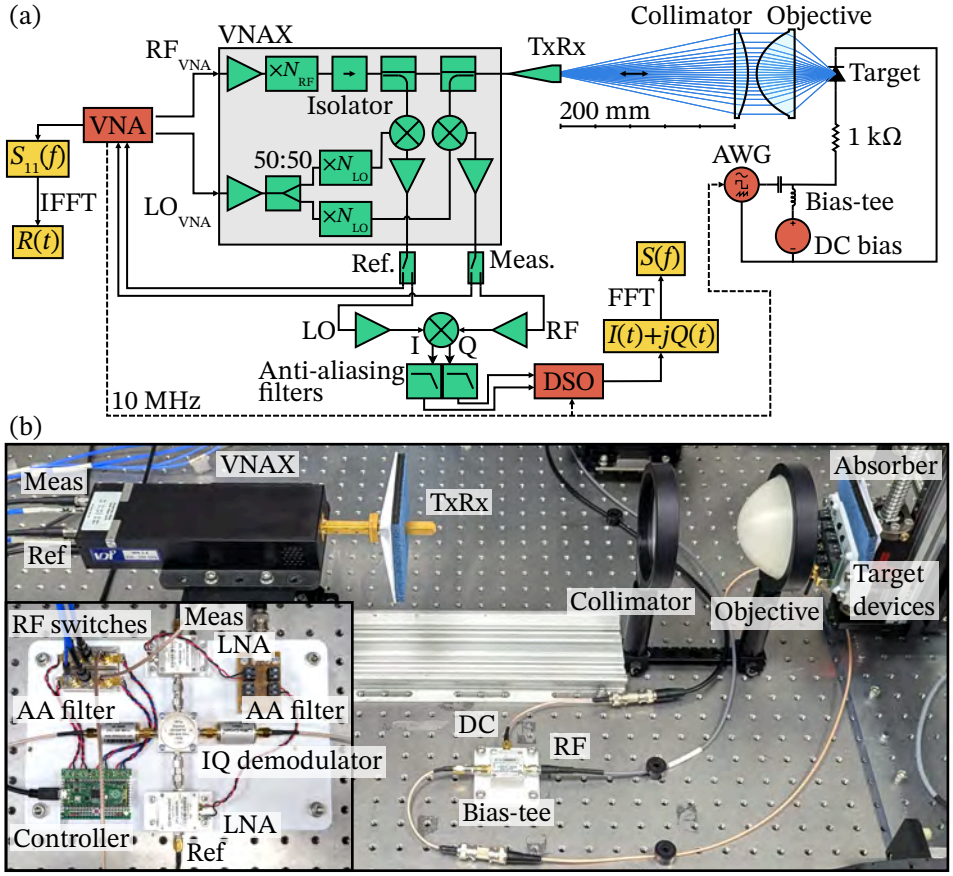

Figure 4.3: Integrated quadrature receiver system. (a) Diagram of the experimental setup used to measure complex reflection over 220–330 GHz. A vector network analyzer (VNA) extension module (VNAX) [231] is used to down-convert the terahertz carrier to an intermediate frequency, providing a reference (Ref.) of the transmitted signal, and a measurement (Meas.) signal encoded with the modulation from the target. RF switches are used to switch data acquisition between the VNA and the custom IQ demodulator attached to the digital storage oscilloscope (DSO) for digital signal processing; the VNA configuration is used for imaging, and the DSO configuration is used for observing carrier sidebands and temporal measurements. The VNA provides the 10 MHz reference clock for the DSO and the AWG (used for megahertz frequency bias). (b) Annotated photograph of the setup. The inset shows the IQ demodulator with LO and RF low noise amplifiers (LNA), and the anti-aliasing filters for the I and Q signals. 3D printed cyclic olefin copolymer lenses collimate and focus the beam from the horn antenna to an approximately 1.3-mm spot on the diode. The diode is retained in a screw terminal block and held 47.3 mm away from the objective lens.

features a maximum amplitude and phase imbalance of 0.6 dB and 6° respectively, important for maintaining signal-to-noise ratio [232], [233]. Anti-aliasing filtering of the IQ signals is achieved with MiniCircuits SLP-100+ low-pass filters, limiting the baseband output to DC–98 MHz. Two MiniCircuits ZX80-DR230-S+ SPDT RF switches are included to switch the Ref and Meas signals from the SNR between the custom IQ demodulator and the VNA, enabling complex reflection measurement over 220–330 GHz via either the conventional VNA method for capturing broadband S_{11} at a low temporal resolution, or the custom homodyne quadrature receiver for capturing S_{11} at a single frequency, at high temporal resolution. The two modes can be selected, typically depending on whether the desired measurement is mostly static and requires broadband observation, such as an offline target device, or if there are high-frequency dynamics that need to be captured at a higher sampling rate, such as an operating target device. Topologies similar to the quadrature receiver are common for sensitive measurements [234], such as vital sign detection [235], [236], nanoscopy [212] and vibrometry [237]. With either acquisition mode, the complex reflection data can be registered in broadband over 220–330 GHz, and can be converted to a time-domain trace via an inverse Fourier transform.

The frequency extension modules utilize frequency multiplication to produce terahertz waves, which degrades phase noise by $20\log_{10} N$ [dB] [238], resulting in spectral broadening. In turn, this decreases the coherence time of the terahertz radiation, limiting the range at which targets can be coherently detected. By homodyning the measured RF signal with a coherent LO, the adverse effects of phase noise exacerbated by the multiplier-based sources are reduced, permitting highly sensitive measurement at high speed without the need for averaging.

To reinforce the concept of operation, we include a mathematical description of the demodulator system. For simplicity, we do not account for the time delay accrued on the measurement arm due to propagation and thus the de-correlation of phase noise, as well as the loss incurred on the transmitted and received signal. To describe the generated terahertz RF and LO signals, let

$$\begin{aligned} E_{\mathrm{RF}}(t) &= A_{\mathrm{RF}}(t)\sin(\omega_{\mathrm{RF}}t + \phi_{\mathrm{RF}}(t)) \text{ and} \\ E_{\mathrm{LO}}(t) &= A_{\mathrm{LO}}(t)\sin(\omega_{\mathrm{LO}}t + \phi_{\mathrm{LO}}(t)) \,, \end{aligned} \tag{4.2}$$

where for both RF and LO multiplier chains $\omega_{\mathrm{RF,LO}}$ is the angular frequency of the terahertz carrier, $A_{\mathrm{RF,LO}}(t)$ is the amplitude noise and $\phi_{\mathrm{RF,LO}}(t)$ is phase noise. Applying time dependent amplitude $A_{\mathrm{PN}}(t)$ and phase modulation $\phi_{\mathrm{PN}}(t)$ to the measured RF signal by

reflecting $E_{\mathrm{RF}}(t)$ off of the PN junction, let

$$\begin{aligned} E_{\mathrm{RFMod}}(t) &= A_{\mathrm{PN}}(t)A_{\mathrm{RF}}(t) \\ &\quad \times \sin(\omega_{\mathrm{RF}}t + \phi_{\mathrm{RF}}(t) + \phi_{\mathrm{PN}}(t)) \,. \end{aligned} \tag{4.3}$$

To generate the reference signal E_{Ref} for the IQ demodulator, the terahertz LO and RF are multiplied:

$$\begin{aligned} E_{\mathrm{Ref}}(t) &= E_{\mathrm{RF}}(t) \times E_{\mathrm{LO}}(t) \\ &= \frac{A_{\mathrm{RF}}(t)A_{\mathrm{LO}}(t)}{2} \\ \times\Big(&\cos(\omega_{\mathrm{RF}}t + \phi_{\mathrm{RF}}(t) - \omega_{\mathrm{LO}}t - \phi_{\mathrm{LO}}(t)) \\ -&\cos(\omega_{\mathrm{RF}}t + \phi_{\mathrm{RF}}(t) + \omega_{\mathrm{LO}}t + \phi_{\mathrm{LO}}(t))\Big) \,. \end{aligned} \tag{4.4}$$

To generate the measure signal E_{Meas} for the IQ demodulator, the terahertz LO and modulated RF are multiplied:

$$\begin{aligned} E_{\mathrm{Meas}}(t) &= E_{\mathrm{RFMod}}(t) \times E_{\mathrm{LO}}(t) \\ &= \frac{A_{\mathrm{PN}}(t)A_{\mathrm{RF}}(t)A_{\mathrm{LO}}(t)}{2} \\ \times\Big(&\cos(\omega_{\mathrm{RF}}t + \phi_{\mathrm{RF}}(t) + \phi_{\mathrm{PN}}(t) - \omega_{\mathrm{LO}}t - \phi_{\mathrm{LO}}(t)) \\ -&\cos(\omega_{\mathrm{RF}}t + \phi_{\mathrm{RF}}(t) + \phi_{\mathrm{PN}}(t) + \omega_{\mathrm{LO}}t + \phi_{\mathrm{LO}}(t))\Big) \,. \end{aligned} \tag{4.5}$$

Ignoring the cosine terms with the frequency sum of $\omega_{\mathrm{RF}}t + \omega_{\mathrm{LO}}t$, and letting intermediate components $A_{\mathrm{Ref}}(t) = A_{\mathrm{Meas}}(t) = A_{\mathrm{RF}}(t)A_{\mathrm{LO}}(t)$, $\omega_{\mathrm{IF}} = \omega_{\mathrm{RF}} - \omega_{\mathrm{LO}}$, and $\phi_{\mathrm{IF}}(t) = \phi_{\mathrm{RF}}(t) - \phi_{\mathrm{LO}}(t)$ we are left with

$$\begin{aligned} E_{\mathrm{Ref}}(t) &= \frac{A_{\mathrm{Ref}}(t)}{2} \times \cos(\omega_{\mathrm{IF}}t + \phi_{\mathrm{IF}}(t)) \text{ and} \\ E_{\mathrm{Meas}}(t) &= \frac{A_{\mathrm{PN}}(t)A_{\mathrm{Meas}}(t)}{2} \\ &\quad \times \cos(\omega_{\mathrm{IF}}t + \phi_{\mathrm{IF}}(t) + \phi_{\mathrm{PN}}(t)) \,. \end{aligned} \tag{4.6}$$

The in-phase (I) component from the IQ demodulator is simply

$$\begin{aligned} E_{\mathrm{I}}(t) &= E_{\mathrm{Ref}}(t)E_{\mathrm{Meas}}(t) \\ &= \frac{A_{\mathrm{Ref}}(t)A_{\mathrm{PN}}(t)A_{\mathrm{Meas}}(t)}{4} \\ &\quad \times \Big(\cos(2\omega_{\mathrm{IF}}t + 2\phi_{\mathrm{IF}}(t) + \phi_{\mathrm{PN}}(t)) \\ &\quad + \cos(-\phi_{\mathrm{PN}}(t))\Big) \,. \end{aligned} \tag{4.7}$$

The quadrature (Q) component from the IQ demodulator is similar to I, but $E_{\mathrm{Ref}}(t)$ un-

dergoes a $\pi/2$ phase shift such that

$$E_{\mathrm{Ref}\,\pi/2}(t) = \frac{A_{\mathrm{Ref}}(t)\sin(\omega_{\mathrm{IF}}t + \phi_{\mathrm{IF}}(t))}{2}\,, \tag{4.8}$$

and thus

$$\begin{aligned} E_{\mathrm{Q}}(t) &= E_{\mathrm{Ref}\,\pi/2}(t)E_{\mathrm{Meas}}(t) \\ &= \frac{A_{\mathrm{Ref}}(t)A_{\mathrm{PN}}(t)A_{\mathrm{Meas}}(t)}{4} \\ &\quad\times\Big(\sin(2\omega_{\mathrm{IF}}t + 2\phi_{\mathrm{IF}}(t) + \phi_{\mathrm{PN}}(t)) \\ &\quad+ \sin(-\phi_{\mathrm{PN}}(t))\Big)\,. \end{aligned} \tag{4.9}$$

The $2\omega_{\mathrm{IF}}$ sinusoid and associated noise are filtered out by the anti-aliasing filters, and by letting $A_{\mathrm{IQ}}(t) = A_{\mathrm{Ref}}(t)A_{\mathrm{Meas}}(t)$, we are left with

$$\begin{aligned} E_{\mathrm{I}}(t) &= \frac{A_{\mathrm{IQ}}(t)A_{\mathrm{PN}}(t)}{4}\cos(-\phi_{\mathrm{PN}}(t)) \text{ and} \\ E_{\mathrm{Q}}(t) &= \frac{A_{\mathrm{IQ}}(t)A_{\mathrm{PN}}(t)}{4}\sin(-\phi_{\mathrm{PN}}(t))\,. \end{aligned} \tag{4.10}$$

This leaves us with the demodulated amplitude containing

$$\begin{aligned} A(t) &= \sqrt{E_{\mathrm{I}}(t)^2 + E_{\mathrm{Q}}(t)^2} \\ &= \frac{A_{\mathrm{IQ}}(t)A_{\mathrm{PN}}(t)}{4}\,, \end{aligned} \tag{4.11}$$

and phase

$$\begin{aligned} \phi(t) &= \tan^{-1}(E_{\mathrm{Q}}(t)/E_{\mathrm{I}}(t)) \\ &= \tan^{-1}\left(\frac{\sin(-\phi_{\mathrm{PN}}(t))}{\cos(-\phi_{\mathrm{PN}}(t))}\right) \\ &= -\phi_{\mathrm{PN}}(t)\,. \end{aligned} \tag{4.12}$$

Additionally, by delaying the reference arm by the same amount of time, the phase noise is more closely correlated to the received signal when undergoing demodulation, resulting in lower phase noise, increasing sensitivity at lower carrier offset frequencies. For an offset frequency f and round-trip time-delay τ_d, the phase noise suppression is $10\log_{10}(4\sin^2(\pi f\tau_d))$ [238], within the coherence time. For our uncompensated system, we still expect reasonable phase noise suppression of -34.87 dB at a 1 MHz offset frequency and $\tau_d = 2.86$ ns time-delay obtained from Fig. 4.1(d).

Since the region of interest corresponding to the semiconductor region is approximately 0.3 mm wide, as seen in the X-ray image of Fig. 4.4(a), we mount the diode on a scanning stage and acquire a 2D complex S_{11} image with the VNA mode. In the interest of decreas-

ing acquisition time to capture the entire frequency domain in one measurement for each pixel, the IQ demodulator is unnecessary for such a raster image, as we are not interested in observing the 2D images over time. Performing an inverse Fourier transform on the complex S_{11} pixels, we obtain the time-domain signal where peaks correspond to the strong reflection of terahertz waves from objects in the optical path. Figure 4.4(b) shows the 2D response of this scan at the time delay corresponding to the diode. From this information, we move the focal spot to the centre of the diode, illuminating the PN junction region with the focused terahertz wave. The RF switches shown in Fig. 4.3(a) are toggled to drive the IQ demodulator, as we now want to observe a single pixel over time at a higher sampling rate. For 1001 terahertz carrier frequencies in the range of 220–330 GHz, the bias voltage across the diode is stepped 50 points from 0–2 V_{DC} each point held for approximately 0.086 s, with 10,000 IQ samples acquired at 1 kS/s to capture the entire duration. Filtered IQ signals from the demodulator are digitized using a Keysight UXR0402AP in High-Resolution mode for effective 12-bit resolution. The bias voltage steps are triggered at the beginning of the IQ acquisition on the oscilloscope. From this measurement we extract the changing time-domain response over the bias voltage steps by applying an inverse Fourier transform to the complex frequency domain data at each voltage step, shown in Fig. 4.4(c). Due to the internal features of the diode being smaller than the bandwidth limited depth resolution of 1.25 mm [7] the diode layers are unresolvable. By observing the measured time-domain trace at the centre and rear of the diode structure, marked by the two dashed lines in Fig. 4.4(c), we show in Fig. 4.4(d) that the reflection corresponding to the junction increases with bias voltage, and that the reflection corresponding to the rear of the device decreases. These results support our model shown in Fig. 4.1(d), which predicts the the front interface of the junction increasing in reflectivity as the silicon becomes conductive, decreasing the power reflected from the rear of the device. We note that this experiment is conducted over several hours and is not real-time, and serves to show the material changes are observed in the junction region of the diode.

4.3 High Frequency Operation

Having established that the change in carrier concentration inside a PN junction is detectable with terahertz waves, a range of discrete semiconductor components with more complex geometries, as listed in Table 4.1, are biased with megahertz frequency signals, and probed at 275 GHz with the IQ demodulator configuration. Given that carrier concentration in semiconductor materials is dependent on temperature [239], it is possible that the observed changes in reflectivity are purely the result of thermal excitation [240]; this experiment serves to refute that hypothesis and show the effect is specific to carrier

concentration of the device. The modulation speed due to the thermo-optic effect in silicon is typically limited to the order of kilohertz [241], [242], so a megahertz bias signal is used to exclude thermal modulation. In addition, the thermal expansion properties of silicon are low enough that we ignore their effect for the purpose of this work [243]. It is expected that the increase and decrease of free carriers occurs within the component, proportional to bias current. A change in carrier-dependent reflectivity modulates the reflected terahertz power. This creates detectable side-bands, offset from the carrier by the modulation frequency.

The discrete semiconductor components shown in Fig. 4.5(a) are fixed in place by a screw terminal. Each device is connected in series with a 1 kΩ resistor and biased by a 1 V_{PP}, 3.14 MHz sinusoidal AC signal, and 0.5 V_{DC}. The bias is applied at the P-side of the junction in each device. The devices are mounted on a 2D translation stage, positioned at the

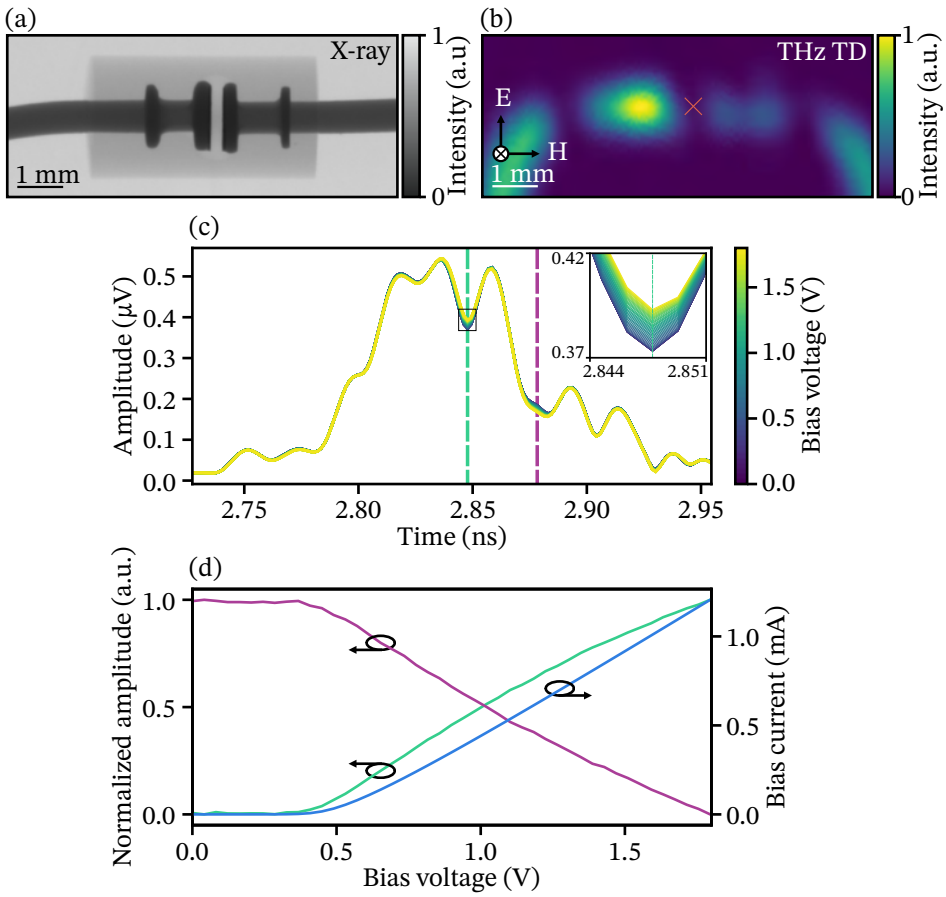

Figure 4.4: Bias voltage ramping at low frequency showing the change in the reflected time-domain signal. (a) X-ray image of the 1N4007 diode. (b) Terahertz time-domain raster image of the diode, obtained with VNA configuration. The wire leads are bent downwards for mounting. The red cross indicates the location of the focal spot for the measurement. (c) Time-domain trace of the central pixel corresponding to the PN junction of the diode, obtained with the IQ configuration. The inset highlights the change in reflectivity from the PN junction. The time, i.e., depth, axis is perpendicular to the plane of (a) and (b). (d) Voltage-dependent amplitude of (c) at the time-domain points indicated by the dashed lines, corresponding to the front and back of the PN junction.

focal point of the objective lens, and raster scanned 10×10 mm^2 in 0.25 mm steps; each scan takes approximately 30 minutes. Each pixel represents 1 million IQ samples, sampled at 7.81 MS/s by a Tektronix DPO70604C real-time oscilloscope operating in High-Resolution mode, with a Hanning window and Fourier transform applied; the IQ magnitude at DC corresponds to the reflected terahertz carrier, while the strongest sideband is at 3.14 MHz. At a sampling rate of 7.81 MS/s, the DPO achieves an effective resolution of 13.82 bits, at a 3.4 MHz bandwidth due to digital boxcar filtering [244].

At the carrier frequency of 275 GHz, the components are identified in Fig. 4.5(b–e), with some internal metallic structure visible. Observing the IQ spectrum with the bias frequency offset relative to the carrier, we show in Fig. 4.5(f–i) that the junction regions are modulating the terahertz carrier at 3.14 MHz. To further illustrate the result of this experiment, Fig. 4.5(j–m) shows the IQ spectrum of the most intense pixel from Fig. 4.5(f–i), along with a background pixel which serves as a reference to calculate the noise floor. We note that the noise floor is low due to the homodyne demodulation scheme and consequent phase noise suppression.

The SNR of each device is shown in Table 4.1. A higher SNR is measured for the two transistor devices, which we attribute to the epitaxial structure facing the incident beam, resulting in a greater area for the terahertz waves to interact. The comparatively low SNR of the two diode devices may be attributable to the metallic bonding structures, visible in Fig. 4.4(a), with the vertical orientation of the electrical contact pads shown in the X-ray image likely limiting the propagation of the vertically polarized terahertz wave. These results show that the observed low-frequency modulation is not thermo-optic, as the modulation speed exceeds kilohertz range, and is the result of carrier injection and depletion within the device junctions. We expect this non-destructive testing method to be beneficial for component manufacturers looking to assess the operational performance during the manufacturing process, as well as serving as a troubleshooting and diagnostic tool for live RF circuits.

Table 4.1: Discrete semiconductor components under test. Forward voltage values measured with a multimeter.

Model	Description	Forward Voltage	SNR
1N4007	General rectifier diode	0.569 V	17.82 dB
1N4148	Signal switching diode	0.583 V	16.80 dB
2N5485	N-Channel JFET	0.763 V	38.81 dB
BC548B	NPN Transistor	0.734 V	40.69 dB

4.4 Discussion

4.4.1 Model Assumptions and Validity

High system sensitivity is needed to overcome the high expected losses from scattering and diffraction from the metal within the semiconductor components. These effects are considered and full-wave simulations in CST Microwave Studio (CST) performed to understand the impact on the experiment, however, the results of these simulations are

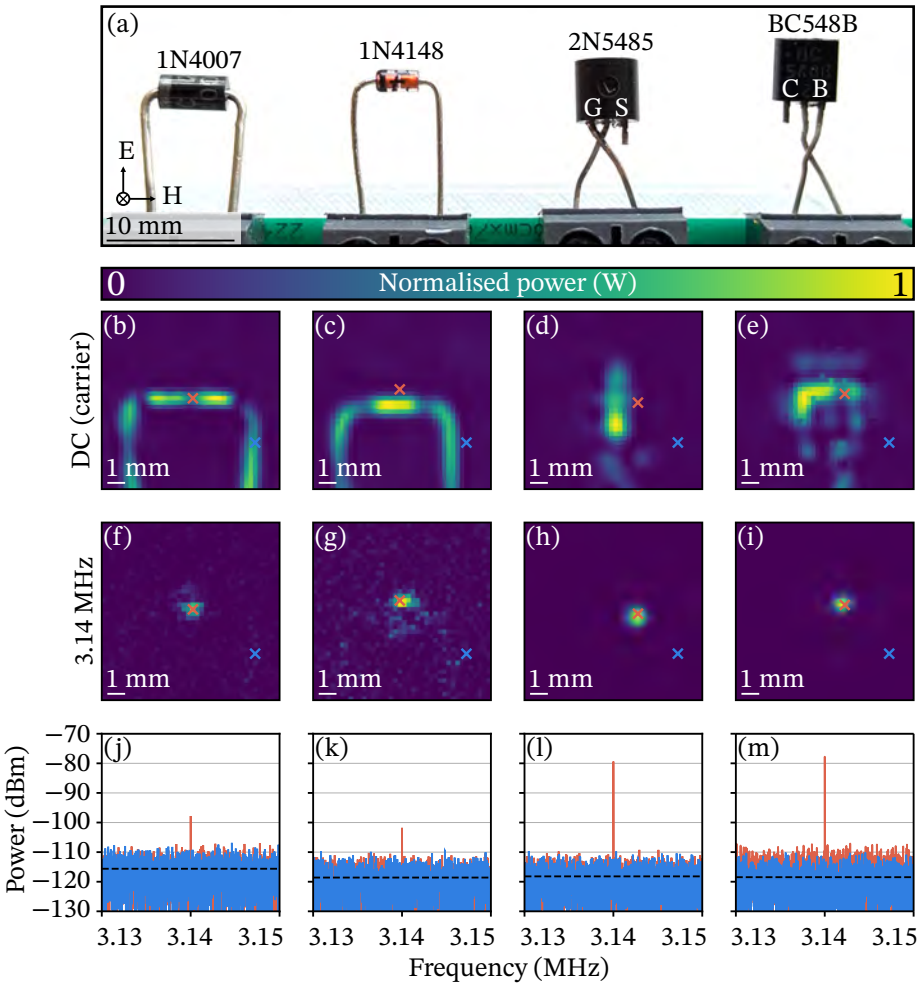

Figure 4.5: Localization of PN junctions in semiconductor components. (a) Photograph of 1N4007, 1N4148, 2N5485, and BC548B (left to right). The legs of the two rightmost devices are twisted for correct polarity. (b–e) Frequency domain raster-scans at 275 GHz. (f–i) Frequency domain raster-scans at 3.14 MHz offset frequency from the 275 GHz carrier. (j–m) Spectra of the four components, corresponding to the marked positions in the raster-scans. The pixels marked in red are the highest power pixels in the 3.14 MHz images, corresponding to the semiconductor region responsible for the sideband modulation, and those marked in blue are reference pixels. The black dashed lines indicates the mean of the spectra at the reference pixel and serve as the noise floor for SNR calculations [245]. The peak power spots in (b–e) differ from those marked in (f–i) due to the stronger reflection at the carrier frequency, which reveals internal metallic structures.

inconclusive, and it was decided to omit this portion of the work from the article. Further study could be done on modelling these contacts as small parallel-plate waveguides coupled via free-space terahertz beams, but the desire to investigate relatively large components such as discrete rectifier diodes in this manner is dwarfed by the small and more dense semiconductor circuits with many more sites for carrier interactions, where this analysis approach would be less relevant.

Regarding the validity of the 1D time-domain reflection model, it is expressed in the article that the model does not intend to fully capture the scattering effects of the physical geometry but is instead used to explain the changes in semiconductor materials in isolation. A deeper explanation and discussion on how these effects affect the model would be of interest but is beyond the scope of the work. Future work could incorporate scattering and diffraction effects into a more complex model but would require significantly more time and resources.

4.4.2 Experimental Considerations

The low-frequency bias ramping experiment takes several hours to obtain full spectrum measurements of the devices and thus capture the time domain response. For a more practical implementation, the time domain results could be substituted by a CW approach, only measuring the reflection coefficient at a single frequency. This would significantly reduce acquisition time, while also reducing the impact of component thermal drift. It is worth noting that the experimental setup is left for several hours to come to equilibrium, according to the manufacturer's specifications. The laboratory is also climate controlled, reducing significant changes in temperature. Phase-stable cables are used between the VNA and the frequency extenders, where the operating frequency is significantly higher. The use of phase stable cables on the IF stage of the setup would be recommended moving forward, but the impact should be reasonably low given the low frequency of IF components and thus long wavelength relative to thermal changes.

4.4.3 Polarization Dependence of Packaged Diodes

The SNR of the high-frequency diode results may have been hampered by the metallic contacts forming a polarization-sensitive scattering structure. Future work should investigate the outcome of rotating the diode 90° and comparing the response; this experiment was omitted from the article due to time constraints and an already high amount of data. It would be worthwhile revisiting this concept with the same system, to improve experimental methodology and potentially gain a deeper understanding of how these devices interact with terahertz radiation. Further analysis of the scattering characteristics

of these structures would be beneficial, in addition to the work done on the semiconductor modelling and design of the data acquisition.

4.5 Conclusion

The properties of offline semiconductor materials and components have been well-studied by terahertz spectroscopy systems over the past few decades, but yet this has not been extended to active devices. From this basis we established our study into probing active devices and observe their behaviour in real-time. By combining Drude and Fresnel models, we show the expected changes in reflection from a packaged PN junction over a range of forward-bias voltages. The model is confirmed experimentally, using a common rectifier diode and a low-terahertz VNA system, to show an increase in reflection as carriers are injected into the junction and the semiconducting material becomes more conductive. This effect is also observed by injecting an AC bias signal into the semiconductor device and observing a weak sideband, modulated onto the terahertz carrier. The presence of the modulated sideband dispels our hypothesis that the observed effect may be thermal in nature as the experiment is performed at megahertz frequency bias, too fast for any thermo-optic effects. The localization of this modulation is shown in both the low- and high-frequency experiments, demonstrating that the observed signals are localized to carrier-dynamic regions of devices and are not due to signal leakage. We anticipate that this work is foundational for future non-destructive testing tools for the semiconductor industry and non-invasive probing for security applications.

Part III

The End

Chapter 5

Conclusion and Outlook

5.1 Thesis Conclusion

In summary, emerging terahertz technologies are versatile, with strong motivations presented for ranging, NDT, and communications applications. It is worth noting that although the coverage of photonics and optics research in this thesis is brief relative to electronics, it does not diminish the level of importance that such contributions have towards the advancement of terahertz science. Photonic devices have a key role to play in the development of compact spectroscopy systems, as well as ultra-stable metrology equipment. Existing fibreoptic communications systems may benefit from short wireless jumps, enabled by terahertz technologies in the years to come. 3D-printed quasi-optical components are a catalyst, accelerating research activities in laboratory environments by permitting the rapid iterative prototyping of systems in-house, evident in the effectiveness of the Risley-prism scanner, dark-field imaging system, and the optical train for probing semiconductors. The Risley-prism scanner emphasises the low-cost aspect of 3D-printing, forming an affordable yet capable imaging system, neglecting the attached vector network analyzer. The dark-field imaging system highlights the versatility offered by 3D-printing, allowing for lens components with complex geometries that would be difficult and time consuming to produce with conventional techniques. The work on semiconductor probing shows how 3D-printed lenses can be used in a laboratory setting, but it better showcases an emerging and unique application for the terahertz region, enabled by the recent development of sources and detectors. In the future, it is hoped that development of cheap on-chip transceivers will enable systems like these three to be implemented for portable and affordable applications. All of this would be difficult if not impossible without COC, which serves as the cornerstone of the work contained within this thesis.

5.2 Future Work

While the original contributions in this thesis have shown that 3D-printed quasi-optics are suitable for integration into functional systems, there remain significant challenges. Future work should take advantage of controllable infill parameters to add more substance to quasi-optical components, moving them beyond what could be possible with conventional manufacturing, as was mentioned briefly at the end of Chapter 1. I had spent some time in the early stages of my candidature working on 3D-printed anti-reflective coatings to mitigate the reflection losses inherent to the COC lenses, but abandoned the work due to delays and stalling progress. This is an area that I still think shows great promise, perhaps better suited for new 3D-printing technologies that may come in the next several years.

There is also much more to be done with the sensing of active semiconductor components. My work was limited to relatively large devices, and I expect with more research that eventually some promising results may come from targeting processors and other integrated circuits with much smaller internal circuitry. This development will likely be enabled by high power source advancement, improved optical trains or probing networks, as well as minor improvements in detection schemes.

5.3 Outlook

To conclude the four years of my PhD candidature, my outlook for the future of terahertz research is grim optimism for the progression of the field. I have remained hopeful yet sceptical over the practical implementation of terahertz technology, which I think is appropriate given the many areas are still mostly in the stage of fundamental research and only beginning to venture into commercialisation. There are many challenges to overcome, but I expect within the next ten years that backhaul communication links will become common amongst terrestrial and extraterrestrial network providers, and potentially short-range radar systems taken up by autonomous driving or armed conflict. I expect 3D-printed quasi-optics have some role to play in future research and development, paving the way for mass scale COC components.

Bibliography

[1] J. D. Hunter, "Matplotlib: A 2D graphics environment," *Computing in Science & Engineering*, vol. 9, no. 3, pp. 90–95, Jun. 2007. DOI: 10.1109/MCSE.2007.55

[2] C. R. Harris et al., "Array programming with NumPy," *Nature*, vol. 585, no. 7825, pp. 357–362, Sep. 2020. DOI: 10.1038/s41586-020-2649-2

[3] B. Ferguson and X.-C. Zhang, "Materials for terahertz science and technology," *Nature Materials*, vol. 1, no. 1, pp. 26–33, Sep. 2002. DOI: 10.1038/nmat708

[4] T. Nagatsuma, "Terahertz technologies: Present and future," *IEICE Electronics Express*, vol. 8, no. 14, pp. 1127–1142, 2011. DOI: 10.1587/elex.8.1127

[5] D. M. Mittleman, "Twenty years of terahertz imaging," *Optics Express*, vol. 26, no. 8, pp. 9417–9431, Apr. 2018. DOI: 10.1364/OE.26.009417

[6] W. Jiang et al., "Terahertz communications and sensing for 6G and beyond: A comprehensive review," *IEEE Communications Surveys & Tutorials*, vol. 26, no. 4, pp. 2326–2381, 2024. DOI: 10.1109/COMST.2024.3385908

[7] H. Lees, C. Hayes, and W. Withayachumnankul, "Terahertz coherence tomography for in-container liquid characterization," *IEEE Journal of Selected Topics in Quantum Electronics*, vol. 29, no. 5: Terahertz Photonics, p. 8 600 408, Jul. 2023. DOI: 10.1109/JSTQE.2023.3294875

[8] G. Ciattaglia et al., "Displacement evaluation by mmwave FMCW radars: Method and performance metrics," *IEEE Transactions on Instrumentation and Measurement*, vol. 73, pp. 1–13, 2024. DOI: 10.1109/TIM.2024.3421440

[9] D. Grischkowsky, S. Keiding, M. van Exter, and C. Fattinger, "Far-infrared time-domain spectroscopy with terahertz beams of dielectrics and semiconductors," *Journal of the Optical Society of America B*, vol. 7, no. 10, pp. 2006–2015, Oct. 1990. DOI: 10.1364/JOSAB.7.002006

[10] T.-I. Jeon and D. Grischkowsky, "Characterization of optically dense, doped semiconductors by reflection THz time domain spectroscopy," *Applied Physics Letters*, vol. 72, no. 23, pp. 3032–3034, Jun. 1998. DOI: 10.1063/1.121531

[11] A. J. Huber, F. Keilmann, J. Wittborn, J. Aizpurua, and R. Hillenbrand, "Terahertz near-field nanoscopy of mobile carriers in single semiconductor nanodevices," *Nano Letters*, vol. 8, no. 11, pp. 3766–3770, Oct. 2008. DOI: 10.1021/nl802086x

[12] M. Herrmann, M. Tani, K. Sakai, and R. Fukasawa, "Terahertz imaging of silicon wafers," *Journal of Applied Physics*, vol. 91, no. 3, pp. 1247–1250, Feb. 2002. DOI: 10.1063/1.1429772

[13] J. B. Baxter and G. W. Guglietta, "Terahertz spectroscopy," *Analytical Chemistry*, vol. 83, no. 12, pp. 4342–4368, 2011. DOI: 10.1021/ac200907z

[14] C. Fattinger and D. Grischkowsky, "Terahertz beams," *Applied Physics Letters*, vol. 54, no. 6, pp. 490–492, Feb. 1989. DOI: 10.1063/1.100958

[15] M. Kato, S. R. Tripathi, K. Murate, K. Imayama, and K. Kawase, *Optics Express*, vol. 24, no. 6, pp. 6425–6432, Mar. 2016. DOI: 10.1364/OE.24.006425

[16] H. Hoshina, Y. Sasaki, A. Hayashi, C. Otani, and K. Kawase, "Noninvasive mail inspection system with terahertz radiation," *Applied Spectroscopy*, vol. 63, no. 1, pp. 81–86, Jan. 2009. DOI: 10.1366/000370209787169713

[17] P. Bawuah and J. A. Zeitler, "Advances in terahertz time-domain spectroscopy of pharmaceutical solids: A review," *TrAC Trends in Analytical Chemistry*, vol. 139, p. 116 272, 2021. DOI: 10.1016/j.trac.2021.116272

[18] L. Thrane, R. Jacobsen, P. Uhd Jepsen, and S. Keiding, "THz reflection spectroscopy of liquid water," *Chemical Physics Letters*, vol. 240, no. 4, pp. 330–333, 1995, ISSN: 0009-2614. DOI: 10.1016/0009-2614(95)00543-D

[19] P. U. Jepsen, J. K. Jensen, and U. Møller, "Characterization of aqueous alcohol solutions in bottles with thz reflection spectroscopy," *Optics Express*, vol. 16, no. 13, pp. 9318–9331, Jun. 2008. DOI: 10.1364/OE.16.009318

[20] J. W. Waters et al., "Stratospheric cio and ozone from the microwave limb sounder on the upper atmosphere research satellite," *Nature*, vol. 362, no. 6421, pp. 597–602, Apr. 1993. DOI: 10.1038/362597a0

[21] T. Crowe, W. Bishop, D. Porterfield, J. Hesler, and R. Weikle, "Opening the terahertz window with integrated diode circuits," *IEEE Journal of Solid-State Circuits*, vol. 40, no. 10, pp. 2104–2110, 2005. DOI: 10.1109/JSSC.2005.854599

[22] C. Kulesa, "Terahertz spectroscopy for astronomy: From comets to cosmology," *IEEE Transactions on Terahertz Science and Technology*, vol. 1, no. 1, pp. 232–240, 2011. DOI: 10.1109/TTHZ.2011.2159648

[23] T. Shuro et al., "The first radioastronomical observation with photonic local oscillator," *Publications of the Astronomical Society of Japan*, vol. 55, no. 4, pp. L53–L56, Aug. 2003. DOI: 10.1093/pasj/55.4.L53

[24] I. C. Mayorga, A. Schmitz, T. Klein, C. Leinz, and R. Gusten, "First in-field application of a full photonic local oscillator to terahertz astronomy," *IEEE Trans-*

actions on Terahertz Science and Technology, vol. 2, no. 4, pp. 393–399, 2012. DOI: 10.1109/TTHZ.2012.2191286

[25] B. Chung, H. Lees, J. L. Hesler, C. Chuengsatiansup, and W. Withayachumnankul, "Non-contact probing of active semiconductor devices using terahertz waves," *IEEE Journal of Microwaves*, vol. 6, no. 2, pp. 324–333, 2026. DOI: 10.1109/JMW.2026.3653411

[26] Y. Cai, Z. Wang, R. Dias, and D. Goyal, "Electro optical terahertz pulse reflectometry — an innovative fault isolation tool," in *2010 Proceedings 60th Electronic Components and Technology Conference (ECTC)*, 2010, pp. 1309–1315. DOI: 10.1109/ECTC.2010.5490646

[27] M. Y. Tay et al., "Advanced fault isolation technique using electro-optical terahertz pulse reflectometry," in *2012 19th IEEE International Symposium on the Physical and Failure Analysis of Integrated Circuits*, 2012, pp. 1–5.

[28] C. Zhang and J. Aguada, "High-precision pulse reflectometry-based fault localization approach for advanced chip package failures," in *ISTFA 2023: Conference Proceedings from the 49th International Symposium for Testing and Failure Analysis*, ser. ISTFA2023, vol. 84741, ASM International, Nov. 2023, pp. 285–290. DOI: 10.31399/asm.cp.istfa2023p0285

[29] J. Y. Liao, K. Giang, T. Pham, and H. L. Marks, "Incorporating time-domain reflectometry in chip-level failure analysis workflow: Case studies," in *ISTFA 2023: Conference Proceedings from the 49th International Symposium for Testing and Failure Analysis*, ser. ISTFA2023, vol. 84741, ASM International, Nov. 2023, pp. 145–150. DOI: 10.31399/asm.cp.istfa2023p0145

[30] J. J. Young, A. I. Hernandez-Serrano, J. Hardwicke, and E. Pickwell-MacPherson, "In vivo terahertz sensing of psoriasis and eczema patients," *Scientific Reports*, vol. 14, no. 1, Jul. 2024. DOI: 10.1038/s41598-024-68106-2

[31] A. Dogra et al., "Towards autonomous robotic THz-based in vivo skin sensing: The PicoBot," *Scientific Reports*, vol. 15, no. 1, Feb. 2025. DOI: 10.1038/s41598-025-88718-6

[32] R. M. Woodward et al., "Terahertz pulse imaging in reflection geometry of human skin cancer and skin tissue," *Physics in Medicine & Biology*, vol. 47, no. 21, p. 3853, Oct. 2002. DOI: 10.1088/0031-9155/47/21/325

[33] P. C. Ashworth et al., "Terahertz pulsed spectroscopy of freshly excised human breast cancer," *Optics Express*, vol. 17, no. 15, pp. 12 444–12 454, Jul. 2009. DOI: 10.1364/OE.17.012444

[34] J. J. Young, B. G. Page, A. I. Hernandez-Serrano, J. Hardwicke, and E. Pickwell-MacPherson, "In vivo terahertz sensing of skin cancer patients," *Advanced Photonics Research*, vol. 6, no. 6, p. 2 400 195, 2025. DOI: 10.1002/adpr.202400195

[35] G. Ok, K. Park, H. J. Kim, H. S. Chun, and S.-W. Choi, "High-speed terahertz imaging toward food quality inspection," *Applied Optics*, vol. 53, no. 7, pp. 1406–1412, Mar. 2014. DOI: 10.1364/AO.53.001406

[36] S.-T. Han, W. K. Park, Y.-H. Ahn, W.-J. Lee, and H. S. Chun, "Development of a compact sub-terahertz gyrotron and its application to t-ray real-time imaging for food inspection," in *2012 37th International Conference on Infrared, Millimeter, and Terahertz Waves*, 2012, pp. 1–2. DOI: 10.1109/IRMMW-THz.2012.6380390

[37] C. Jördens, "Detection of foreign bodies in chocolate with pulsed terahertz spectroscopy," *Optical Engineering*, vol. 47, no. 3, p. 037 003, 2008. DOI: 10.1117/1.2896597

[38] A. V. Shchepetilnikov, A. M. Zarezin, V. M. Muravev, P. A. Gusikhin, and I. V. Kukushkin, "Quantitative analysis of water content and distribution in plants using terahertz imaging," *Optical Engineering*, vol. 59, no. 6, p. 061 617, 2020. DOI: 10.1117/1.OE.59.6.061617

[39] X. You, V. Pagay, and W. Withayachumnankul, "Non-contact monitoring of plant leaf water status using terahertz waves," *Journal of Infrared, Millimeter, and Terahertz Waves*, vol. 46, no. 8, Aug. 2025. DOI: 10.1007/s10762-025-01074-4

[40] W. S. L. Lee, A. Ferrante, W. Withayachumnankul, and J. A. Able, "Assessing frost damage in barley using terahertz imaging," *Optics Express*, vol. 28, no. 21, pp. 30 644–30 655, 2020. DOI: 10.1364/OE.404618

[41] M. Skolnik, "Fifty years of radar," *Proceedings of the IEEE*, vol. 73, no. 2, pp. 182–197, 1985. DOI: 10.1109/PROC.1985.13132

[42] B. P. Abbott et al., "Observation of gravitational waves from a binary black hole merger," *Physical Review Letters*, vol. 116, p. 061 102, 6 Feb. 2016. DOI: 10.1103/PhysRevLett.116.061102

[43] I. Kim et al., "Nanophotonics for light detection and ranging technology," *Nature Nanotechnology*, vol. 16, no. 5, pp. 508–524, May 2021. DOI: 10.1038/s41565-021-00895-3

[44] G. Vinci, S. Lindner, F. Barbon, R. Weigel, and A. Koelpin, "Promise of a better position," *IEEE Microwave Magazine*, vol. 13, no. 7, S41–S49, 2012. DOI: 10.1109/MMM.2012.2216710

[45] A. Stove, "Potential applications for low-tera-hertz radar," in *2015 16th International Radar Symposium (IRS)*, 2015, pp. 191–196. DOI: 10.1109/IRS.2015.7226264

[46] S. Rao, *Intro to mmWave Sensing: FMCW Radars*, Jun. 2017. [Online]. Available: https://training.ti.com/intro-mmwave-sensing-fmcw-radars-module-1-range-estimation

[47] B. Baumann, B. Gashi, D. Meier, and C. Zech, "High-resolution 400 GHz submillimeter-wave quasi-optical radar imaging system," *IEEE Microwave and Wireless Components Letters*, vol. 32, no. 3, pp. 226–229, 2022. DOI: 10.1109/LMWC.2022.3142354

[48] P. V. Brennan, Y. Huang, M. Ash, and K. Chetty, "Determination of sweep linearity requirements in FMCW radar systems based on simple voltage-controlled oscillator sources," *IEEE Transactions on Aerospace and Electronic Systems*, vol. 47, no. 3, pp. 1594–1604, 2011. DOI: 10.1109/TAES.2011.5937252

[49] S. Piper, "Homodyne FMCW radar range resolution effects with sinusoidal nonlinearities in the frequency sweep," in *Proceedings International Radar Conference*, 1995, pp. 563–567. DOI: 10.1109/RADAR.1995.522609

[50] Z. Wang, T. Chang, and H.-L. Cui, "Review of active millimeter wave imaging techniques for personnel security screening," *IEEE Access*, vol. 7, pp. 148 336–148 350, 2019. DOI: 10.1109/ACCESS.2019.2946736

[51] J. Grajal et al., "3-D high-resolution imaging radar at 300 GHz with enhanced FoV," *IEEE Transactions on Microwave Theory and Techniques*, vol. 63, no. 3, pp. 1097–1107, 2015. DOI: 10.1109/TMTT.2015.2391105

[52] T. Ikari, Y. Sasaki, and C. Otani, "275–305 GHz FM-CW radar 3D imaging for walk-through security body scanner," *Photonics*, vol. 10, no. 3, 2023. DOI: 10.3390/photonics10030343

[53] T. Ikari, Y. Sasaki, and C. Otani, "Development of a two-beam terahertz FMCW walk-through body scanner for seamless security screening," *IEEE Transactions on Terahertz Science and Technology*, vol. 15, no. 5, pp. 771–780, 2025. DOI: 10.1109/TTHZ.2025.3585672

[54] S. of Automotive Engineers International, *J3016: Taxonomy and definitions for terms related to driving automation systems for on-road motor vehicles*, Apr. 2021. [Online]. Available: https://www.sae.org/standards/content/j3016_202104/

[55] D. Jasteh, E. G. Hoare, M. Cherniakov, and M. Gashinova, "Experimental low-terahertz radar image analysis for automotive terrain sensing," *IEEE Geoscience and Remote Sensing Letters*, vol. 13, no. 4, pp. 490–494, 2016. DOI: 10.1109/LGRS.2016.2518579

[56] F. Norouzian, E. G. Hoare, E. Marchetti, M. Cherniakov, and M. Gashinova, "Next generation, low-THz automotive radar – the potential for frequencies above 100 GHz," in *2019 20th International Radar Symposium (IRS)*, 2019, pp. 1–7. DOI: 10.23919/IRS.2019.8767461

[57] L. Daniel, D. Phippen, E. Hoare, A. Stove, M. Cherniakov, and M. Gashinova, "Low-THz radar, lidar and optical imaging through artificially generated fog,"

in *International Conference on Radar Systems (Radar 2017)*, 2017, pp. 1–4. DOI: 10.1049/cp.2017.0369

[58] D. R. Vizard, M. Gashinova, E. Hoare, and M. Cherniakov, "Low THz automotive radar developments employing 300–600 GHz frequency extenders," in *2015 16th International Radar Symposium (IRS)*, 2015, pp. 209–214. DOI: 10.1109/IRS.2015.7226250

[59] C. Li, V. M. Lubecke, O. Boric-Lubecke, and J. Lin, "A review on recent advances in doppler radar sensors for noncontact healthcare monitoring," *IEEE Transactions on Microwave Theory and Techniques*, vol. 61, no. 5, pp. 2046–2060, May 2013. DOI: 10.1109/TMTT.2013.2256924

[60] D. T. Petkie, C. Benton, and E. Bryan, "Millimeter wave radar for remote measurement of vital signs," in *2009 IEEE Radar Conference*, 2009, pp. 1–3. DOI: 10.1109/RADAR.2009.4977021

[61] T. Nagatsuma, G. Ducournau, and C. C. Renaud, "Advances in terahertz communications accelerated by photonics," *Nature Photonics*, vol. 10, no. 6, pp. 371–379, May 2016. DOI: 10.1038/nphoton.2016.65

[62] M. Shehata, K. Wang, and W. Withayachumnankul, "Carrierless amplitude and phase modulation for terahertz communications," *IEEE Journal of Selected Topics in Quantum Electronics*, vol. 29, no. 5: Terahertz Photonics, p. 8 600 714, 2023. DOI: 10.1109/JSTQE.2023.3316886

[63] H.-J. Song and N. Lee, "Terahertz communications: Challenges in the next decade," *IEEE Transactions on Terahertz Science and Technology*, vol. 12, no. 2, pp. 105–117, 2022. DOI: 10.1109/TTHZ.2021.3128677

[64] I. Dan et al., "A 300-GHz wireless link employing a photonic transmitter and an active electronic receiver with a transmission bandwidth of 54 GHz," *IEEE Transactions on Terahertz Science and Technology*, vol. 10, no. 3, pp. 271–281, 2020. DOI: 10.1109/TTHZ.2020.2977331

[65] S. Nellen et al., "Coherent wireless link at 300 GHz with 160 Gbit/s enabled by a photonic transmitter," *Journal of Lightwave Technology*, vol. 40, no. 13, pp. 4178–4185, 2022. DOI: 10.1109/JLT.2022.3160096

[66] K. Maekawa, T. Yoshioka, T. Nakashita, T. Ohara, and T. Nagatsuma, "Single-carrier 220-Gbit/s sub-THz wireless transmission over 214 m using a photonics-based system," *Optics Letters*, vol. 49, no. 16, pp. 4666–4668, Aug. 2024. DOI: 10.1364/OL.527593

[67] D. W. Porterfield, "High-efficiency terahertz frequency triplers," in *2007 IEEE/MTT-S International Microwave Symposium*, 2007, pp. 337–340. DOI: 10.1109/MWSYM.2007.380439

[68] S. Makhlouf et al., "Terahertz sources and receivers: From the past to the future," *IEEE Journal of Microwaves*, vol. 3, no. 3, pp. 894–912, 2023. DOI: 10.1109/JMW.2023.3282875

[69] T. Reck, S. Durant, and J. Hesler, "Characterization of WM164 (1.1-1.5 THz) spectrum analyzer extenders," in *2024 49th International Conference on Infrared, Millimeter, and Terahertz Waves (IRMMW-THz)*, 2024, pp. 1–2. DOI: 10.1109/IRMMW-THz60956.2024.10697812

[70] I. Mehdi, J. V. Siles, C. Lee, and E. Schlecht, "THz diode technology: Status, prospects, and applications," *Proceedings of the IEEE*, vol. 105, no. 6, pp. 990–1007, 2017. DOI: 10.1109/JPROC.2017.2650235

[71] X. Zhang et al., "A 300-330 GHz frequency tripler with >100 mW output and >17% efficiency based on face-to-face topology and enhanced diode configuration," *IEEE Transactions on Terahertz Science and Technology*, vol. 16, no. 1, pp. 42–53, 2026. DOI: 10.1109/TTHZ.2025.3597197

[72] A. Maestrini et al., "Design and characterization of a room temperature all-solid-state electronic source tunable from 2.48 to 2.75 THz," *IEEE Transactions on Terahertz Science and Technology*, vol. 2, no. 2, pp. 177–185, 2012. DOI: 10.1109/TTHZ.2012.2183740

[73] J. V. Siles, K. Cooper, C. Lee, R. Lin, G. Chattopadhyay, and I. Mehdi, "A compact room-temperature 510-560 GHz frequency tripler with 30-mW output power," in *2018 15th European Radar Conference (EuRAD)*, 2018, pp. 333–336. DOI: 10.23919/EuRAD.2018.8546537

[74] J. V. Siles, K. B. Cooper, C. Lee, R. H. Lin, G. Chattopadhyay, and I. Mehdi, "A new generation of room-temperature frequency-multiplied sources with up to 10× higher output power in the 160-GHz-1.6-THz range," *IEEE Transactions on Terahertz Science and Technology*, vol. 8, no. 6, pp. 596–604, 2018. DOI: 10.1109/TTHZ.2018.2876620

[75] A. Maestrini et al., "A frequency-multiplied source with more than 1 mW of power across the 840-900-GHz band," *IEEE Transactions on Microwave Theory and Techniques*, vol. 58, no. 7, pp. 1925–1932, 2010. DOI: 10.1109/TMTT.2010.2050171

[76] A. Maestrini et al., "In-phase power-combined frequency triplers at 300 GHz," *IEEE Microwave and Wireless Components Letters*, vol. 18, no. 3, pp. 218–220, 2008. DOI: 10.1109/LMWC.2008.916820

[77] J. V. Siles, A. E. Maestrini, C. Lee, R. Lin, and I. Mehdi, "First demonstration of an all-solid-state room temperature 2-THz front end viable for space applications," *IEEE Transactions on Terahertz Science and Technology*, vol. 14, no. 5, pp. 607–612, 2024. DOI: 10.1109/TTHZ.2024.3430013

[78] T. W. Crowe, J. L. Hesler, S. A. Retzloff, and D. S. Kurtz, "Higher power multipliers for terahertz sources," in *2016 41st International Conference on Infrared, Millimeter, and Terahertz waves (IRMMW-THz)*, 2016, pp. 1–1. DOI: 10.1109/IRMMW-THz.2016.7758351

[79] E. Bryerton, S. Retzloff, and J. Hesler, "High-power submillimeter wave solid-state sources," in *2019 12th Global Symposium on Millimeter Waves (GSMM)*, 2019, pp. 29–31. DOI: 10.1109/GSMM.2019.8797648

[80] *Virginia Diodes Inc.* [Online]. Available: https://vadiodes.com/

[81] J. Treuttel et al., "A 520–620-GHz Schottky receiver front-end for planetary science and remote sensing with 1070 K-1500 K DSB noise temperature at room temperature," *IEEE Transactions on Terahertz Science and Technology*, vol. 6, no. 1, pp. 148–155, 2016. DOI: 10.1109/TTHZ.2015.2496421

[82] D. Moro-Melgar, V. L. Rubio, O. Cojocari, I. Opra, and A. Negrus, "600 - 900 GHz frequency sources with up to 4 mW output power based on flip-chip Schottky barrier diodes technology," in *2022 47th International Conference on Infrared, Millimeter and Terahertz Waves (IRMMW-THz)*, 2022, pp. 1–1. DOI: 10.1109/IRMMW-THz50927.2022.9895924

[83] O. Cojocari, I. Oprea, H. Gibson, and A. Walber, "Submm-wave multipliers by film-diode technology," in *2016 46th European Microwave Conference (EuMC)*, 2016, pp. 337–340. DOI: 10.1109/EuMC.2016.7824347

[84] D. Moro-Melgar, O. Cojocari, and I. Oprea, "High power high efficiency 475-520 GHz source based on discrete Schottky diodes," in *2020 50th European Microwave Conference (EuMC)*, 2021, pp. 607–610. DOI: 10.23919/EuMC48046.2021.9338081

[85] *Advanced Compound Semiconductor Technologies (ACST) GmbH*. [Online]. Available: https://acst.de/

[86] Y. Tian et al., "High efficiency 285 GHz tripler based on face-to-face differential configuration," *Journal of Infrared and Millimeter Waves*, vol. 41, no. 4, pp. 739–744, Aug. 2022. DOI: 10.11972/j.issn.1001-9014.2022.04.013

[87] Y. Tian et al., "A 325-GHz balanced frequency tripler based on novel three-port e-probe with individual groundings for RF and DC," *IEEE Microwave and Wireless Technology Letters*, vol. 33, no. 4, pp. 411–414, 2023. DOI: 10.1109/LMWT.2022.3224913

[88] Y. Tian et al., "A novel balanced frequency tripler with improved power capacity for submillimeter-wave application," *IEEE Microwave and Wireless Components Letters*, vol. 31, no. 8, pp. 925–928, 2021. DOI: 10.1109/LMWC.2021.3084622

[89] R. Li et al., "A 315-345 GHz quad-port balanced tripler with inherent suppressions on even-order harmonics using discrete Schottky diodes," *Microwave and Optical Technology Letters*, vol. 66, no. 4, e34151, 2024. DOI: 10.1002/mop.34151

[90] J. Jun et al., "Single-stage frequency quadrupler with SBD and four-octave LPF at 335 GHz," *IEEE Transactions on Terahertz Science and Technology*, vol. 7, no. 4, pp. 446–454, 2017. DOI: 10.1109/TTHZ.2017.2709720

[91] X. Song et al., "A 170-230 GHz high-power frequency doubler based on a GaAs MMIC process," *IEEE Microwave and Wireless Technology Letters*, vol. 33, no. 4, pp. 427–430, 2023. DOI: 10.1109/LMWT.2022.3220244

[92] Z. Liu et al., "High output power 340GHz frequency doubler design based on linear optimization method," Apr. 2024. DOI: 10.21203/rs.3.rs-4230538/v1

[93] F. Yang et al., "Near 1 THz biasless frequency tripler based on membrane technology," in *2020 International Conference on Microwave and Millimeter Wave Technology (ICMMT)*, 2020, pp. 1–3. DOI: 10.1109/ICMMT49418.2020.9386502

[94] X. Luo and Y. Zhang, "The design of a monolithic wideband GaN-based frequency doubler for G-band," in *2023 Cross Strait Radio Science and Wireless Technology Conference (CSRSWTC)*, 2023, pp. 1–3. DOI: 10.1109/CSRSWTC60855.2023.10427518

[95] J. L. Hesler and T. W. Crowe, "NEP and responsivity of THz zero-bias Schottky diode detectors," in *2007 Joint 32nd International Conference on Infrared and Millimeter Waves and the 15th International Conference on Terahertz Electronics*, 2007, pp. 844–845. DOI: 10.1109/ICIMW.2007.4516758

[96] T. Nagatsuma et al., "Terahertz wireless communications based on photonics technologies," *Optics Express*, vol. 21, no. 20, pp. 23 736–23 747, Oct. 2013. DOI: 10.1364/OE.21.023736

[97] T. Harter et al., "Generalized Kramers–Kronig receiver for coherent terahertz communications," *Nature Photonics*, vol. 14, no. 10, pp. 601–606, Sep. 2020. DOI: 10.1038/s41566-020-0675-0

[98] T. Nagatsuma, H. Ito, and T. Ishibashi, "High-power RF photodiodes and their applications," *Laser & Photonics Reviews*, vol. 3, no. 1–2, pp. 123–137, Feb. 2009. DOI: 10.1002/lpor.200810024

[99] S. Nellen et al., "Experimental comparison of UTC- and PIN-photodiodes for continuous-wave terahertz generation," *Journal of Infrared, Millimeter, and Terahertz Waves*, vol. 41, no. 4, pp. 343–354, Dec. 2019. DOI: 10.1007/s10762-019-00638-5

[100] G. Ducournau et al., "Highly coherent terahertz wave generation with a dual-frequency Brillouin fiber laser and a 1.55um photomixer," *Optics Letters*, vol. 36, no. 11, pp. 2044–2046, Jun. 2011. DOI: 10.1364/OL.36.002044

[101] S. Nellen et al., "Fiber-coupled, photoconductive receiver for heterodyne detection up to 1 THz stabilized by an optical frequency comb," in *2017 42nd International Conference on Infrared, Millimeter, and Terahertz Waves (IRMMW-THz)*, IEEE, Aug. 2017. DOI: 10.1109/irmmw-thz.2017.8067019

[102] T. Harter et al., "Wireless THz link with optoelectronic transmitter and receiver," *Optica*, vol. 6, no. 8, p. 1063, Aug. 2019. DOI: 10.1364/optica.6.001063

[103] Y. Hu, B. S. Marks, C. R. Menyuk, V. J. Urick, and K. J. Williams, "Modeling sources of nonlinearity in a simple p-i-n photodetector," *Journal of Lightwave Technology*, vol. 32, no. 20, pp. 3710–3720, Oct. 2014. DOI: 10.1109/jlt.2014.2315740

[104] S. E. J. Mahabadi, T. F. Carruthers, C. R. Menyuk, J. D. McKinney, and K. J. Williams, "Impact of nonlinearity including bleaching in MUTC photodetectors on RF-modulated electro-optic frequency combs," *Optics Express*, vol. 29, no. 8, pp. 11 520–11 532, Apr. 2021. DOI: 10.1364/OE.420096

[105] T. Liu et al., "Transient simulation of UTC-PD using drift-diffusion model," in *2017 International Conference on Numerical Simulation of Optoelectronic Devices (NUSOD)*, IEEE. DOI: 10.1109/nusod.2017.8010030

[106] S. E. J. Mahabadi, T. F. Carruthers, C. R. Menyuk, J. D. McKinney, and K. J. Williams, "Impact on frequency combs of nonlinearity including bleaching in p-i-n photodetectors," in *2020 IEEE Photonics Society Summer Topicals Meeting Series (SUM)*, IEEE, Jul. 2020. DOI: 10.1109/sum48678.2020.9161030

[107] J. Riemensberger et al., "Massively parallel coherent laser ranging using a soliton microcomb," *Nature*, vol. 581, no. 7807, pp. 164–170, May 2020. DOI: 10.1038/s41586-020-2239-3

[108] N. Couture, M. Lippl, W. Cui, A. Gamouras, N. Y. Joly, and J.-M. Ménard, "Performance analysis of tabletop single-pulse terahertz detection at rates up to 1.1 MHz," *Physical Review Applied*, vol. 21, art. no. 054020, 5 May 2024. DOI: 10.1103/PhysRevApplied.21.054020

[109] N. M. Burford and M. O. El-Shenawee, "Review of terahertz photoconductive antenna technology," *Optical Engineering*, vol. 56, no. 1, art. no. 010901, 2017. DOI: 10.1117/1.OE.56.1.010901

[110] F. Rettich, N. Vieweg, O. Cojocari, and A. Deninger, "Field intensity detection of individual terahertz pulses at 80 MHz repetition rate," *Journal of Infrared, Millimeter, and Terahertz Waves*, vol. 36, no. 7, pp. 607–612, May 2015. DOI: 10.1007/s10762-015-0162-8

[111] J. Hebling, K.-L. Yeh, M. C. Hoffmann, and K. A. Nelson, "High-power thz generation, thz nonlinear optics, and thz nonlinear spectroscopy," *IEEE Journal of*

Selected Topics in Quantum Electronics, vol. 14, no. 2, pp. 345–353, 2008. DOI: 10.1109/JSTQE.2007.914602

[112] P. Jepsen, D. Cooke, and M. Koch, "Terahertz spectroscopy and imaging - modern techniques and applications," *Laser & Photonics Reviews*, vol. 5, no. 1, pp. 124–166, 2011. DOI: 10.1002/lpor.201000011

[113] N. Kumar, U. Singh, A. Bera, and A. Sinha, "A review on the sub-THz/THz gyrotrons," *Infrared Physics & Technology*, vol. 76, pp. 38–51, 2016. DOI: 10.1016/j.infrared.2016.01.015

[114] S. Kumar, "Recent progress in terahertz quantum cascade lasers," *IEEE Journal of Selected Topics in Quantum Electronics*, vol. 17, no. 1, pp. 38–47, 2011. DOI: 10.1109/JSTQE.2010.2049735

[115] D. Headland, Y. Monnai, D. Abbott, C. Fumeaux, and W. Withayachumnankul, "Tutorial: Terahertz beamforming, from concepts to realizations," *APL Photonics*, vol. 3, no. 5, p. 051 101, 2018. DOI: 10.1063/1.5011063

[116] J. Ma, N. J. Karl, S. Bretin, G. Ducournau, and D. M. Mittleman, "Frequency-division multiplexer and demultiplexer for terahertz wireless links," *Nature Communications*, vol. 8, no. 1, Sep. 2017. DOI: 10.1038/s41467-017-00877-x

[117] H. Matsumoto, I. Watanabe, A. Kasamatsu, and Y. Monnai, "Integrated terahertz radar based on leaky-wave coherence tomography," *Nature Electronics*, vol. 3, no. 2, pp. 122–129, 2020. DOI: 10.1038/s41928-019-0357-4

[118] H. Lees, D. Headland, S. Murakami, M. Fujita, and W. Withayachumnankul, "Terahertz radar with all-dielectric leaky-wave antenna," *APL Photonics*, vol. 9, no. 3, p. 036 107, Mar. 2024. DOI: 10.1063/5.0180941

[119] H. Lees, B. Chung, D. Headland, and W. Withayachumnankul, "Simultaneous multi-target monitoring with terahertz leaky-wave radar," in *2024 49th International Conference on Infrared, Millimeter, and Terahertz Waves (IRMMW-THz)*, 2024, pp. 1–2. DOI: 10.1109/IRMMW-THz60956.2024.10697599

[120] D. M. Pozar, *Microwave Engineering*, English, Fourth edition. Hoboken, N.J: Wiley, 2012, ISBN: 9781118213636.

[121] H. Saeidi, S. Venkatesh, C. R. Chappidi, T. Sharma, C. Zhu, and K. Sengupta, "A 4×4 steerable 14-dBm EIRP array on CMOS at 0.41 THz with a 2-D distributed oscillator network," *IEEE Journal of Solid-State Circuits*, vol. 57, no. 10, pp. 3125–3138, 2022. DOI: 10.1109/JSSC.2022.3183163

[122] M. Yang and L. Wu, "A 298–334-GHz scalable injection-locked phased-array radiator with second-subharmonic-termination-assisted waveform formulation for power enhancement," *IEEE Journal of Solid-State Circuits*, pp. 1–12, 2025. DOI: 10.1109/JSSC.2025.3624563

[123] Z. B. Harris, A. Virk, M. E. Khani, and M. H. Arbab, "Terahertz time-domain spectral imaging using telecentric beam steering and an f-θ scanning lens: Distortion compensation and determination of resolution limits," *Optics Express*, vol. 28, no. 18, pp. 26 612–26 622, Sep. 2020. DOI: 10.1364/OE.398706

[124] Z. B. Harris, S. Katletz, M. E. Khani, A. Virk, and M. H. Arbab, "Design and characterization of telecentric F-θ scanning lenses for broadband terahertz frequency systems," *AIP Advances*, vol. 10, no. 12, 2020, 125313. DOI: 10.1063/5.0030110

[125] P. Rezapoor, A. Tamminen, J. Ala-Laurinaho, D. Ruan, and Z. Taylor, "A telecentric offset reflective imaging system (TORIS) for terahertz imaging and spectroscopy," *IEEE Transactions on Terahertz Science and Technology*, vol. 15, no. 5, pp. 787–799, 2025. DOI: 10.1109/TTHZ.2025.3579299

[126] K. Sato and Y. Monnai, "Terahertz beam steering based on trajectory deflection in dielectric-free Luneburg lens," *IEEE Transactions on Terahertz Science and Technology*, vol. 10, no. 3, pp. 229–236, 2020. DOI: 10.1109/TTHZ.2020.2983915

[127] B. Nie, H. Lu, T. Skaik, Y. Liu, and Y. Wang, "A 3D-printed subterahertz metallic surface-wave Luneburg lens multibeam antenna," *IEEE Transactions on Terahertz Science and Technology*, vol. 13, no. 3, pp. 297–301, 2023. DOI: 10.1109/TTHZ.2023.3242227

[128] Y. Monnai, K. Altmann, C. Jansen, H. Hillmer, M. Koch, and H. Shinoda, "Terahertz beam steering and variable focusing using programmable diffraction gratings," *Optics Express*, vol. 21, no. 2, pp. 2347–2354, 2013. DOI: 10.1364/OE.21.002347

[129] B. Scherger, C. Jördens, and M. Koch, "Variable-focus terahertz lens," *Optics Express*, vol. 19, no. 5, pp. 4528–4535, 2011. DOI: 10.1364/OE.19.004528

[130] B. Scherger, M. Scheller, C. Jansen, M. Koch, and K. Wiesauer, "Terahertz lenses made by compression molding of micropowders," *Applied Optics*, vol. 50, no. 15, pp. 2256–2262, May 2011. DOI: 10.1364/ao.50.002256

[131] J. Sun and F. Hu, "Three-dimensional printing technologies for terahertz applications: A review," *International Journal of RF and Microwave Computer-Aided Engineering*, vol. 30, no. 1, Oct. 2019. DOI: 10.1002/mmce.21983

[132] B. Zhang, Y.-X. Guo, H. Zirath, and Y. P. Zhang, "Investigation on 3-D-Printing technologies for millimeter- wave and terahertz applications," *Proceedings of the IEEE*, vol. 105, no. 4, pp. 723–736, Apr. 2017. DOI: 10.1109/jproc.2016.2639520

[133] T. Whittaker, S. Zhang, A. Powell, C. J. Stevens, J. Y. C. Vardaxoglou, and W. Whittow, "3D printing materials and techniques for antennas and metamaterials: A survey of the latest advances," *IEEE Antennas and Propagation Magazine*, vol. 65, no. 3, pp. 10–20, 2023. DOI: 10.1109/MAP.2022.3229298

[134] A. D. Squires, E. Constable, and R. A. Lewis, "3D printed terahertz diffraction gratings and lenses," *Journal of Infrared, Millimeter, and Terahertz Waves*, vol. 36, no. 1, pp. 72–80, Nov. 2014. DOI: 10.1007/s10762-014-0122-8

[135] E. Castro-Camus, M. Koch, and A. I. Hernandez-Serrano, "Additive manufacture of photonic components for the terahertz band," *Journal of Applied Physics*, vol. 127, no. 21, p. 210 901, Jun. 2020. DOI: 10.1063/1.5140270

[136] C. H. Brodie et al., "Comprehensive study of 3D printing materials over the terahertz regime: Absorption coefficient and refractive index characterizations," *Optics Materials Express*, vol. 12, no. 9, pp. 3379–3402, Sep. 2022. DOI: 10.1364/OME.465820

[137] S. F. Busch, M. Weidenbach, J. C. Balzer, and M. Koch, "THz optics 3D printed with TOPAS," *Journal of Infrared, Millimeter, and Terahertz Waves*, vol. 37, no. 4, pp. 303–307, 2015. DOI: 10.1007/s10762-015-0236-7

[138] S. F. Busch, M. Weidenbach, M. Fey, F. Schäfer, T. Probst, and M. Koch, "Optical properties of 3D printable plastics in the THz regime and their application for 3D printed THz optics," *Journal of Infrared, Millimeter, and Terahertz Waves*, vol. 35, no. 12, pp. 993–997, Oct. 2014. DOI: 10.1007/s10762-014-0113-9

[139] E. Castro-Camus, M. Koch, and A. I. Hernandez-Serrano, "Additive manufacture of photonic components for the terahertz band," *Journal of Applied Physics*, vol. 127, no. 21, p. 210 901, Jun. 2020. DOI: 10.1063/1.5140270

[140] G.-B. Wu, K. F. Chan, S.-W. Qu, and C. H. Chan, "A 2-D beam-scanning Bessel launcher for terahertz applications," *IEEE Transactions on Antennas and Propagation*, vol. 68, no. 8, pp. 5893–5903, 2020. DOI: 10.1109/TAP.2020.2988936

[141] L. Phillips et al., "Optical characterisation of stereolithography-printed composites for THz quasi-optical applications," in *2025 50th International Conference on Infrared, Millimeter, and Terahertz Waves (IRMMW-THz)*, 2025, pp. 1–2. DOI: 10.1109/IRMMW-THz61557.2025.11319737

[142] Z. Zhang, X. Weiand, C. Liu, K. Wang, J. Liu, and Z. Yang, "Rapid fabrication of terahertz lens via three-dimensional printing technology," *Chinese Optics Letters*, vol. 13, no. 2, pp. 022 201–22 204, Feb. 2015. DOI: 10.3788/col201513.022201

[143] E. Mavrona, J. Graf, E. Hack, and P. Zolliker, "Optimized 3D printing of THz waveguides with cyclic olefin copolymer," *Optical Materials Express*, vol. 11, no. 8, pp. 2495–2504, 2021. DOI: 10.1364/OME.428378

[144] T. Kubiczek, K. Kolpatzeck, T. Schultze, and J. C. Balzer, "A highly frequency-selective 3D-printed dielectric structure for the terahertz range," *Journal of Infrared, Millimeter, and Terahertz Waves*, Mar. 2024. DOI: 10.1007/s10762-024-00973-2

[145] A. Nieradka, M. Kaluza, H. Rudyk, P. Komorowski, and A. Siemion, "3D printed polarisers for THz spectral range," in *2024 25th International Microwave and Radar Conference (MIKON)*, 2024, pp. 238–240. DOI: 10.23919/MIKON60251.2024.10633982

[146] J. Bomba, J. Suszek, M. Makowski, A. Sobczyk, and M. Sypek, "3-D printed anti-reflection structures for the terahertz region," *Journal of Infrared, Millimeter, and Terahertz Waves*, vol. 39, no. 1, pp. 24–35, Sep. 2017. DOI: 10.1007/s10762-017-0435-5

[147] B. Yan et al., "Printing special surface components for THz 2D and 3D imaging," *Scientific Reports*, vol. 10, no. 1, Nov. 2020. DOI: 10.1038/s41598-020-77998-9

[148] M. S. Li, M. Abdullah, J. He, K. Wang, C. Fumeaux, and W. Withayachumnankul, "Frequency-diverse antenna with convolutional neural networks for direction-of-arrival estimation in terahertz communications," *IEEE Transactions on Terahertz Science and Technology*, vol. 14, no. 3, pp. 354–363, 2024. DOI: 10.1109/TTHZ.2024.3358735

[149] M. Kaluza, M. Walczakowski, P. Komorowski, and A. Siemion, "Influence of 3D printing parameters on the THz optical properties of COC material," in *2024 49th International Conference on Infrared, Millimeter, and Terahertz Waves (IRMMW-THz)*, 2024, pp. 1–2. DOI: 10.1109/IRMMW-THz60956.2024.10697561

[150] J. Huang, S. J. Chen, Z. Xue, W. Withayachumnankul, and C. Fumeaux, "Impact of infill pattern on 3D printed dielectric resonator antennas," in *2018 IEEE Asia-Pacific Conference on Antennas and Propagation (APCAP)*, 2018, pp. 233–235. DOI: 10.1109/APCAP.2018.8538296

[151] J. Huang, S. J. Chen, Z. Xue, W. Withayachumnankul, and C. Fumeaux, "Wideband endfire 3-D-printed dielectric antenna with designable permittivity," *IEEE Antennas and Wireless Propagation Letters*, vol. 17, no. 11, pp. 2085–2089, 2018. DOI: 10.1109/LAWP.2018.2857497

[152] M. Kaluza, M. Walczakowski, and A. Siemion, "Exploring the impact of 3D printing parameters on the THz optical characteristics of COC material," *Materials*, vol. 17, no. 20, 2024. DOI: 10.3390/ma17205104

[153] W. H. Southwell, "Gradient-index antireflection coatings," *Optics Letters*, vol. 8, no. 11, pp. 584–586, Nov. 1983. DOI: 10.1364/OL.8.000584

[154] M. E. Ibrahim, D. Headland, W. Withayachumnankul, and C. H. Wang, "Non-destructive testing of defects in polymer–matrix composite materials for marine applications using terahertz waves," *Journal of Nondestructive Evaluation*, vol. 40, no. 2, art. no. 37, 2021. DOI: 10.1007/s10921-021-00767-9

[155] C. Jansen et al., "Terahertz imaging: Applications and perspectives," *Applied Optics*, vol. 49, no. 19, pp. 48–57, 2010. DOI: 10.1364/AO.49.000E48

[156] G. Ok, K. Park, H. S. Chun, H.-J. Chang, N. Lee, and S.-W. Choi, "High-performance sub-terahertz transmission imaging system for food inspection," *Biomedical Optics Express*, vol. 6, no. 5, p. 1929, 2015. DOI: 10.1364/boe.6.001929

[157] C. M. Armstrong, "The truth about terahertz," *IEEE Spectrum*, vol. 49, no. 9, pp. 36–41, 2012. DOI: 10.1109/MSPEC.2012.6281131

[158] A. Dobroiu, K. Asama, S. Suzuki, M. Asada, and H. Ito, "Terahertz-wave three-dimensional imaging using a resonant-tunneling-diode oscillator," *Journal of Infrared, Millimeter, and Terahertz Waves*, vol. 43, no. 5–6, pp. 464–478, 2022. DOI: 10.1007/s10762-022-00863-5

[159] S. Mohammadzadeh et al., "Hand-guided mobile terahertz 3D imaging platform with aspherical telecentric f-θ optics," in *2021 18th European Radar Conference (EuRAD)*, 2022, pp. 377–380. DOI: 10.23919/EuRAD50154.2022.9784526

[160] T. Sagisaka et al., "Integrated terahertz optics with effective medium for 600-GHz-band imaging," in *2020 International Topical Meeting on Microwave Photonics (MWP)*, 2020, pp. 62–65. DOI: 10.23919/MWP48676.2020.9314570

[161] J. S. Yahng, C.-S. Park, H. D. Lee, C.-S. Kim, and D.-S. Yee, "High-speed frequency-domain terahertz coherence tomography," *Optics Express*, vol. 24, no. 2, pp. 1053–1061, Jan. 2016. DOI: 10.1364/OE.24.001053

[162] S. Katletz et al., "Efficient terahertz en-face imaging," *Optics Express*, vol. 19, no. 23, pp. 23 042–23 053, Nov. 2011. DOI: 10.1364/OE.19.023042

[163] D.-S. Yee, K. H. Jin, J. S. Yahng, H.-S. Yang, C. Y. Kim, and J. C. Ye, "High-speed terahertz reflection three-dimensional imaging using beam steering," *Optics Express*, vol. 23, no. 4, pp. 5027–5034, Feb. 2015. DOI: 10.1364/OE.23.005027

[164] N. Oda et al., "Microbolometer terahertz focal plane array and camera with improved sensitivity in the sub-terahertz region," *Journal of Infrared, Millimeter, and Terahertz Waves*, vol. 36, no. 10, pp. 947–960, 2015. DOI: 10.1007/s10762-015-0184-2

[165] H. Lu, S. Zhu, T. Skaik, B. Nie, Y. Liu, and Y. Wang, "Sub-terahertz metallic multi-beam antenna based on a sliding aperture technique," *IEEE Transactions on Antennas and Propagation*, vol. 72, no. 1, pp. 290–299, 2024. DOI: 10.1109/TAP.2023.3323894

[166] K. H. May, S. Mohammadzadeh, A. Keil, G. von Freymann, and F. Friederich, "Coherent off-axis terahertz tomography with a multi-channel array and f-theta optics," *Sensors*, vol. 24, no. 2, p. 529, 2024. DOI: 10.3390/s24020529

[167] H. Hu, W. Lin, X. Ma, X. Hu, and X. Wang, "Terahertz 3-D fast line-scanning imaging using 3-D printed devices," *Optics Express*, vol. 32, no. 3, pp. 4111–4121, Jan. 2024. DOI: 10.1364/OE.511757

[168] S. D. Risley, "A new rotary prism," *Transactions of the American Ophthalmological Society*, vol. 5, pp. 412–413, 1889.

[169] K. Debbarma, N. Truong, S. K. Sharma, and J.-C. S. Chieh, "2-D beam steering performance of a triple mode horn antenna integrated with Risley prism and phase correcting surface," *IEEE Open Journal of Antennas and Propagation*, vol. 3, pp. 752–761, 2022. DOI: 10.1109/OJAP.2022.3187373

[170] S. A. Matos, N. J. G. Fonseca, J. C. Serra, J. M. Felício, J. R. Costa, and C. A. Fernandes, "Generalized Risley prism for beam-steering transmit arrays with reduced grating lobes," *IEEE Transactions on Antennas and Propagation*, vol. 71, no. 11, pp. 8420–8428, 2023. DOI: 10.1109/tap.2023.3313230

[171] C. D. McEwen and M. R. Khan, "Beam steering method with improved sidelobe response using dielectric wedges for satellite TV reception," in *1984 14th European Microwave Conference*, 1984, pp. 681–685. DOI: 10.1109/EUMA.1984.333403

[172] P. Church, J. Matheson, X. Cao, and G. Roy, "Evaluation of a steerable 3D laser scanner using a double Risley prism pair," in *Degraded Environments: Sensing, Processing, and Display 2017*, J. (N. Sanders-Reed and J. (J. A. III, Eds., International Society for Optics and Photonics, vol. 10197, 2017, 101970O. DOI: 10.1117/12.2262198

[173] S. Lu et al., "Inter-satellite laser communication system based on double Risley prisms beam steering," *Applied Optics*, vol. 58, no. 27, pp. 7517–7522, 2019. DOI: 10.1364/AO.58.007517

[174] J. A. Cluff, "Apparatus and method for investigating a sample," US8373126B2, Feb. 2013. [Online]. Available: https://patents.google.com/patent/US8373126B2

[175] E. P. Parrott, S. M. Y. Sy, T. Blu, V. P. Wallace, and E. Pickwell-MacPherson, "Terahertz pulsed imaging in vivo: measurements and processing methods," *Journal of Biomedical Optics*, vol. 16, no. 10, p. 106 010, 2011. DOI: 10.1117/1.3642002

[176] Z. Lyu et al., "A beam-scannable photonic THz-ISAC system based on Risley prisms," in *2023 Asia Communications and Photonics Conference/2023 International Photonics and Optoelectronics Meetings*, 2023. [Online]. Available: https://doi.org/10.1109/ACP/POEM59049.2023.10368958

[177] I. Maestrojuan, I. Palacios, I. Ederra, and R. Gonzalo, "Use of COC substrates for millimeter-wave devices," *Microwave and Optical Technology Letters*, vol. 57, no. 2, pp. 371–377, 2014. DOI: 10.1002/mop.28848

[178] K. Nielsen, H. K. Rasmussen, A. J. L. Adam, P. C. M. Planken, O. Bang, and P. U. Jepsen, "Bendable, low-loss TOPAS fibers for the terahertz frequency range," *Optics Express*, vol. 17, no. 10, pp. 8592–8601, 2009. DOI: 10.1364/OE.17.008592

[179] M. Naftaly, "Parameter extraction in time-domain spectrometers," English, in *Terahertz Metrology*, ser. Microwave Engineering, 1st ed., Norwood: Artech House, 2014, pp. 33–66, ISBN: 9781608077762.

[180] B. Chung, H. Lees, D. Headland, and W. Withayachumnankul, "Broadband and efficient terahertz beam scanning using a 3D-printed Risley prism," in *2022 47th International Conference on Infrared, Millimeter and Terahertz Waves*, 2022. DOI: 10.1109/IRMMW-THz50927.2022.9895483

[181] Y. Zhou, Y. Lu, M. Hei, G. Liu, and D. Fan, "Motion control of the wedge prisms in Risley-prism-based beam steering system for precise target tracking," *Applied Optics*, vol. 52, no. 12, pp. 2849–2857, 2013. DOI: 10.1364/AO.52.002849

[182] M. Sánchez and D. Gutow, "Control laws for a three-element Risley prism optical beam pointer," in *Free-Space Laser Communications VI*, A. K. Majumdar and C. C. Davis, Eds., International Society for Optics and Photonics, vol. 6304, 2006, p. 630 403. DOI: 10.1117/12.678149

[183] M. Born and E. Wolf, *Principles of Optics: 60th Anniversary Edition*, 7th ed. Cambridge University Press, 2019. DOI: 10.1017/9781108769914

[184] H. Yuan, D. Voß, A. Lisauskas, D. Mundy, and H. G. Roskos, "3D Fourier imaging based on 2D heterodyne detection at THz frequencies," *APL Photonics*, vol. 4, no. 10, p. 106 108, Oct. 2019. DOI: 10.1063/1.5116553

[185] S. J. Yoon, P. Bajcsy, M. Litorja, and J. J. Filliben, "Evaluation of lateral resolution of light field cameras," *Optical Engineering*, vol. 57, no. 09, art. no. 093101, Sep. 2018. DOI: 10.1117/1.oe.57.9.093101

[186] W. H. Southwell, "Pyramid-array surface-relief structures producing antireflection index matching on optical surfaces," *Journal of the Optical Society of America A*, vol. 8, no. 3, pp. 549–553, Mar. 1991. DOI: 10.1364/JOSAA.8.000549

[187] A. Siemion, L. Minkevičius, L. Qi, and G. Valušis, "Spatial filtering based terahertz imaging of low absorbing objects," *Optics and Lasers in Engineering*, vol. 139, art. no. 106476, 2021. DOI: 10.1016/j.optlaseng.2020.106476

[188] Y. Wang, Z. Zhao, Z. Chen, L. Zhang, and K. Kang, "Diffraction-induced edge contrast enhancement for terahertz imaging," *Chinese Optics Letters*, vol. 7, no. 8, pp. 690–693, Aug. 2009.

[189] Z. Hua, J. Liu, and C. Liu, "High-resolution dark-field confocal microscopy based on radially polarized illumination," *Optics Express*, vol. 30, no. 7, pp. 11 066–11 078, Mar. 2022. DOI: 10.1364/OE.451507

[190] J. Liu, J. Liu, C. Liu, and Y. Wang, "3D dark-field confocal microscopy for subsurface defects detection," *Optics Letters*, vol. 45, no. 3, pp. 660–663, Feb. 2020. DOI: 10.1364/OL.384487

[191] T. Löffler, T. Bauer, K. J. Siebert, H. G. Roskos, A. Fitzgerald, and S. Czasch, "Terahertz dark-field imaging of biomedical tissue," *Optics Express*, vol. 9, no. 12, pp. 616–621, Dec. 2001. DOI: 10.1364/OE.9.000616

[192] N. Hasegawa, T. Löffler, M. Thomson, and H. G. Roskos, "Remote identification of protrusions and dents on surfaces by terahertz reflectometry with spatial beam filtering and out-of-focus detection," *Applied Physics Letters*, vol. 83, no. 19, pp. 3996–3998, Nov. 2003.

[193] R. Jain, F. Landskron, J. Grzyb, and U. R. Pfeiffer, "Object feature extraction with focused terahertz plenoptic imaging," in *2018 43rd International Conference on Infrared, Millimeter, and Terahertz Waves (IRMMW-THz)*, 2018, pp. 1–2. DOI: 10.1109/IRMMW-THz.2018.8509974

[194] T. Loffler, K. J. Siebert, N. Hasegawa, T. Hahn, and H. G. Roskos, "All-optoelectronic terahertz imaging systems and examples of their application," *Proceedings of the IEEE*, vol. 95, no. 8, pp. 1576–1582, 2007. DOI: 10.1109/JPROC.2007.898901

[195] M. Lei and B. Yao, "Multifunctional darkfield microscopy using an axicon," *Journal of Biomedical Optics*, vol. 13, no. 4, art. no. 044024, 2008. DOI: 10.1117/1.2960019

[196] H. Liu, S. Wu, M. Zhao, Z. Wan, and G. Fang, "A novel terahertz dark-field imaging method for contrast enhancement," *IEEE Transactions on Plasma Science*, vol. 52, no. 10, pp. 5047–5053, 2024. DOI: 10.1109/TPS.2024.3417444

[197] J. H. McLeod, "The axicon: A new type of optical element," *Journal of the Optical Society of America*, vol. 44, no. 8, pp. 592–597, Aug. 1954. DOI: 10.1364/JOSA.44.000592

[198] U. Fuchs, D. Braun, and S. Wickenhagen, "Beam shaping concepts with aspheric surfaces," in *Laser Beam Shaping XVI*, A. Forbes and T. E. Lizotte, Eds., International Society for Optics and Photonics, vol. 9581, SPIE, 2015, art. no. 95810L. DOI: 10.1117/12.2186524

[199] T. Breen, N. Basque-Giroux, U. Fuchs, and I. Golub, "Tuning the resolution and depth of field of a lens using an adjustable ring beam illumination," *Applied Optics*, vol. 59, no. 15, pp. 4744–4749, May 2020. DOI: 10.1364/AO.389353

[200] Y. H. Ong and Q. Liu, "Axicon lens-based cone shell configuration for depth-sensitive fluorescence measurements in turbid media," *Optics Letters*, vol. 38, no. 15, pp. 2647–2649, Aug. 2013. DOI: 10.1364/OL.38.002647

[201] M. Rioux, R. Tremblay, and P. A. Bélanger, "Linear, annular, and radial focusing with axicons and applications to laser machining," *Applied Optics*, vol. 17, no. 10, pp. 1532–1536, May 1978. DOI: 10.1364/AO.17.001532

[202] B. Chung, D. Headland, and W. Withayachumnankul, "Terahertz imaging with 3D-printed Risley-prism and telecentric objective," *IEEE Transactions on Terahertz Science and Technology*, vol. 14, no. 4, pp. 446–454, 2024. DOI: 10.1109/TTHZ.2024.3404642

[203] A. D. Squires and R. A. Lewis, "Feasibility and characterization of common and exotic filaments for use in 3D printed terahertz devices," *Journal of Infrared, Millimeter, and Terahertz Waves*, vol. 39, no. 7, pp. 614–635, Jun. 2018. DOI: 10.1007/s10762-018-0498-y

[204] R. Soref and B. Bennett, "Electrooptical effects in silicon," *IEEE Journal of Quantum Electronics*, vol. 23, no. 1, pp. 123–129, Jan. 1987. DOI: 10.1109/JQE.1987.1073206

[205] M. van Exter and D. Grischkowsky, "Carrier dynamics of electrons and holes in moderately doped silicon," *Physical Review B*, vol. 41, pp. 12 140–12 149, 17 Jun. 1990. DOI: 10.1103/PhysRevB.41.12140

[206] D. Mittleman, R. Jacobsen, and M. Nuss, "T-ray imaging," *IEEE Journal of Selected Topics in Quantum Electronics*, vol. 2, no. 3, pp. 679–692, Sep. 1996. DOI: 10.1109/2944.571768

[207] S. Nashima, O. Morikawa, K. Takata, and M. Hangyo, "Measurement of optical properties of highly doped silicon by terahertz time domain reflection spectroscopy," *Applied Physics Letters*, vol. 79, no. 24, pp. 3923–3925, Dec. 2001. DOI: 10.1063/1.1413498

[208] R. Ulbricht, E. Hendry, J. Shan, T. F. Heinz, and M. Bonn, "Carrier dynamics in semiconductors studied with time-resolved terahertz spectroscopy," *Reviews of Modern Physics*, vol. 83, pp. 543–586, 2 Jun. 2011. DOI: 10.1103/RevModPhys.83.543

[209] T. Arnold, W. Muehleisen, J. Schicker, and C. Hirschl, "Inspection of mechanical and electrical properties of silicon wafers using terahertz tomography and spectroscopy," in *Terahertz Physics, Devices, and Systems IX: Advanced Applications in Industry and Defense*, Bellingham, WA, USA: SPIE, May 2015. DOI: 10.1117/12.2176999

[210] C.-Y. Jen and C. Richter, "Doping profile recognition applied to silicon photovoltaic cells using terahertz time-domain spectroscopy," *IEEE Transactions on Terahertz Science and Technology*, vol. 4, no. 5, pp. 560–567, Sep. 2014. DOI: 10.1109/TTHZ.2014.2330977

[211] J. Hennig et al., "Wide-range resistivity characterization of semiconductors with terahertz time-domain spectroscopy," *Optics Express*, vol. 32, no. 12, pp. 21 028–21 041, Jun. 2024. DOI: 10.1364/OE.519564

[212] C. Liewald, S. Mastel, J. Hesler, A. J. Huber, R. Hillenbrand, and F. Keilmann, "All-electronic terahertz nanoscopy," *Optica*, vol. 5, no. 2, pp. 159–163, Feb. 2018. DOI: 10.1364/OPTICA.5.000159

[213] V. C. Agulto, T. Iwamoto, Z. Zhao, S. Liu, K. Kato, and M. Nakajima, "Wafer-scale mapping of carrier density and mobility with terahertz time-domain ellipsometry," *Optics Letters*, vol. 50, no. 3, pp. 948–951, Feb. 2025. DOI: 10.1364/OL.546091

[214] R. A. Kaindl, M. A. Carnahan, D. Hägele, R. Lövenich, and D. S. Chemla, "Ultrafast terahertz probes of transient conducting and insulating phases in an electron–hole gas," *Nature*, vol. 423, no. 6941, pp. 734–738, Jun. 2003. DOI: 10.1038/nature01676

[215] P. A. George et al., "Ultrafast optical-pump terahertz-probe spectroscopy of the carrier relaxation and recombination dynamics in epitaxial graphene," *Nano Letters*, vol. 8, no. 12, pp. 4248–4251, Nov. 2008. DOI: 10.1021/nl8019399

[216] A. M. Ulatowski et al., "Contrasting charge-carrier dynamics across key metal-halide perovskite compositions through in situ simultaneous probes," *Advanced Functional Materials*, vol. 33, no. 51, p. 2 305 283, Aug. 2023. DOI: 10.1002/adfm.202305283

[217] C. S. Ponseca, A. Yartsev, E. Wang, M. R. Andersson, D. Vithanage, and V. Sundström, "Ultrafast terahertz photoconductivity of bulk heterojunction materials reveals high carrier mobility up to nanosecond time scale," *Journal of the American Chemical Society*, vol. 134, no. 29, pp. 11 836–11 839, Jul. 2012. DOI: 10.1021/ja301757y

[218] T. Kiwa, M. Tonouchi, M. Yamashita, and K. Kawase, "Laser terahertz-emission microscope for inspecting electrical faults in integrated circuits," *Optics Letters*, vol. 28, no. 21, pp. 2058–2060, Nov. 2003. DOI: 10.1364/OL.28.002058

[219] M. Yamashita et al., "THz emission characteristics from p/n junctions with metal lines under non-bias conditions for LSI failure analysis," *Optics Express*, vol. 19, no. 11, pp. 10 864–10 873, May 2011. DOI: 10.1364/OE.19.010864

[220] B. Chung, H. Lees, C. Chuengsatiansup, and W. Withayachumnankul, "Probing live PN junctions with terahertz waves," in *2023 48th International Conference on Infrared, Millimeter, and Terahertz Waves (IRMMW-THz)*, New York, NY, USA: IEEE, Sep. 2023. DOI: 10.1109/IRMMW-THz57677.2023.10299299

[221] C.-T. Sah, R. N. Noyce, and W. Shockley, "Carrier generation and recombination in P-N junctions and P-N junction characteristics," *Proceedings of the Institute of Radio Engineers*, vol. 45, no. 9, pp. 1228–1243, Sep. 1957.

[222] G. T. Reed, G. Mashanovich, F. Y. Gardes, and D. J. Thomson, "Silicon optical modulators," *Nature Photonics*, vol. 4, no. 8, pp. 518–526, Jul. 2010. DOI: 10.1038/nphoton.2010.179

[223] H.-T. Chen, W. J. Padilla, M. J. Cich, A. K. Azad, R. D. Averitt, and A. J. Taylor, "A metamaterial solid-state terahertz phase modulator," *Nature Photonics*, vol. 3, no. 3, pp. 148–151, Feb. 2009. DOI: 10.1038/nphoton.2009.3

[224] K. J. Willis, S. C. Hagness, and I. Knezevic, "A generalized Drude model for doped silicon at terahertz frequencies derived from microscopic transport simulation," *Applied Physics Letters*, vol. 102, no. 12, p. 122 113, Mar. 2013. DOI: 10.1063/1.4798658

[225] COMSOL, Inc., *P–N Junction 1D — comsol.com*, English, Tektronix Inc., 2023. [Online]. Available: https://www.comsol.com/model/pn-junction-1d-14621

[226] A. Kannegulla, M. I. B. Shams, L. Liu, and L.-J. Cheng, "Photo-induced spatial modulation of THz waves: Opportunities and limitations," *Optics Express*, vol. 23, no. 25, pp. 32 098–32 112, Dec. 2015. DOI: 10.1364/OE.23.032098

[227] K. M. Kramer and W. N. G. Hitchon, *Semiconductor Devices: A Simulation Approach*, eng, 1st ed. Upper Saddle River, N.J: Prentice Hall PTR, 1997, ISBN: 9780136143307.

[228] J. Dorkel and P. Leturcq, "Carrier mobilities in silicon semi-empirically related to temperature, doping and injection level," *Solid-State Electronics*, vol. 24, no. 9, pp. 821–825, 1981. DOI: https://doi.org/10.1016/0038-1101(81)90097-6

[229] B. E. A. Saleh and M. C. Teich, *Fundamentals of photonics* (Wiley series in pure and applied optics), English, 3rd ed. Hoboken, N.J: Wiley, 2019, ISBN: 9781119506874.

[230] B. Chung, H. Lees, M. Ibrahim, D. Headland, and W. Withayachumnankul, "Highly efficient terahertz dark-field imaging system with 3D-printed components," *Journal of Physics: Photonics*, vol. 7, no. 2, p. 025 012, Mar. 2025. DOI: 10.1088/2515-7647/adb81e

[231] Virginia Diodes, Inc., *Product overview - VNAX Vector Network Analyzer Extension Modules*, English, VDI, Apr. 2025, 53 pp. [Online]. Available: https://www.vadiodes.com/images/Products/VNA/Product_Manual/VDI-707.1-VNAx-Product-Manual.pdf

[232] A. Tarighat, R. Bagheri, and A. Sayed, "Compensation schemes and performance analysis of IQ imbalances in OFDM receivers," *IEEE Transactions on Signal Processing*, vol. 53, no. 8, pp. 3257–3268, Aug. 2005. DOI: 10.1109/TSP.2005.851156

[233] P. Gregorčič, T. Požar, and J. Možina, "Quadrature phase-shift error analysis using a homodyne laser interferometer," *Optics Express*, vol. 17, no. 18, pp. 16 322–16 331, Aug. 2009. DOI: 10.1364/OE.17.016322

[234] J. Watchi, S. Cooper, B. Ding, C. M. Mow-Lowry, and C. Collette, "Contributed review: A review of compact interferometers," *Review of Scientific Instruments*, vol. 89, no. 12, p. 121 501, Dec. 2018. DOI: 10.1063/1.5052042

[235] I. V. Mikhelson, S. Bakhtiari, T. W. Elmer II, and A. V. Sahakian, "Remote sensing of heart rate and patterns of respiration on a stationary subject using 94-GHz millimeter-wave interferometry," *IEEE Transactions on Biomedical Engineering*, vol. 58, no. 6, pp. 1671–1677, Jun. 2011. DOI: 10.1109/TBME.2011.2111371

[236] S. Diebold et al., "A W-Band MMIC radar system for remote detection of vital signs," *Journal of Infrared, Millimeter, and Terahertz Waves*, vol. 33, no. 12, pp. 1250–1267, Oct. 2012. DOI: 10.1007/s10762-012-9941-7

[237] H. Song and J.-I. Song, "Terahertz-wave vibrometer using a phase-noise-compensated self-heterodyne system," *IEEE Photonics Technology Letters*, vol. 28, no. 3, pp. 363–366, Feb. 2016. DOI: 10.1109/LPT.2015.2496328

[238] K. Siddiq, M. K. Hobden, S. R. Pennock, and R. J. Watson, "Phase noise in FMCW radar systems," *IEEE Transactions on Aerospace and Electronic Systems*, vol. 55, no. 1, pp. 70–81, Feb. 2019. DOI: 10.1109/TAES.2018.2847999

[239] R. Couderc, M. Amara, and M. Lemiti, "Reassessment of the intrinsic carrier density temperature dependence in crystalline silicon," *Journal of Applied Physics*, vol. 115, no. 9, p. 093 705, Mar. 2014. DOI: 10.1063/1.4867776

[240] S. Nashima, O. Morikawa, K. Takata, and M. Hangyo, "Temperature dependence of optical and electronic properties of moderately doped silicon at terahertz frequencies," *Journal of Applied Physics*, vol. 90, no. 2, pp. 837–842, Jul. 2001. DOI: 10.1063/1.1376673

[241] J. V. Campenhout, W. M. J. Green, S. Assefa, and Y. A. Vlasov, "Integrated NiSi waveguide heaters for CMOS-compatible silicon thermo-optic devices," *Optics Letters*, vol. 35, no. 7, pp. 1013–1015, Apr. 2010. DOI: 10.1364/OL.35.001013

[242] N. C. Harris et al., "Efficient, compact and low loss thermo-optic phase shifter in silicon," *Optics Express*, vol. 22, no. 9, pp. 10 487–10 493, May 2014. DOI: 10.1364/OE.22.010487

[243] S. Seliverstov, S. Svyatodukh, and G. Goltsman, "Thermal phase shift in THz silicon effective-medium waveguide," *Applied Physics Letters*, vol. 123, no. 9, p. 092 202, Sep. 2023. DOI: 10.1063/5.0159945

[244] Tektronix Inc., *FAQ ID 55421*, English, Tektronix Inc. [Online]. Available: https://www.tek.com/en/support/faqs/i-could-not-find-any-information-regarding-increase-bits-resolution-hires-mode-there-an

[245] J. Nikonowicz, A. Mahmood, E. Sisinni, and M. Gidlund, "Noise power estimators in ISM radio environments: Performance comparison and enhancement using a novel samples separation technique," *IEEE Transactions on Instrumenta-*

tion and Measurement, vol. 68, no. 1, pp. 105–115, Jan. 2019. DOI: 10.1109/TIM.2018.2833998

Glossary

A

ABS acrylonitrile butadiene styrene 20
ASOPS asynchronous optical sampling 16

C

CMOS complementary metal-oxide-semiconductor 17
COC Cyclic Olefin Copolymer 18, 20–22, 25, 29–31, 33, 40, 43, 45, 46, 51, 52, 74, 87, 88
CST CST Microwave Studio 82
CW continuous-wave 14, 15, 17, 83

E

ECOPS electronically controlled optical sampling 16

F

FDM fused deposition modelling 19, 45
FMCW frequency-modulated continuous-wave 9, 10, 15
FWHM full width at half maximum 54, 55

I

IF intermediate frequency 75, 83
IFFT inverse fast Fourier transform 39, 55
IQ in-phase and quadrature 75–77, 79, 81

L

LiDAR light detection and ranging 8, 10
LO local oscillator 74–77
LTEM laser emission terahertz microscopy 70
LWA leaky-wave antenna 17

M

MTF modulation transfer function 40, 45, 55, 57

N

NDT non-destructive testing 4, 7, 8, 14, 28, 45, 50, 61, 87

O

OPTP optical-pump terahertz-probe 70

P

PCA photoconductive antenna 15, 16
PLA polylactic acid 20, 44, 54

R

radar radio detection and ranging 8–10, 88
RF radio-frequency 17, 20, 74–77, 79, 81

S

SBD Schottky barrier diode 12–14
SNR signal to noise ratio 29, 81, 83
SNR vector network analyzer extender 74–76

T

TDS time-domain spectroscopy 5, 8, 64, 70
ToF time of flight 8, 10

U

UTC-PD uni-traveling-carrier photodiode 14

V

VNA vector network analyser 29, 30, 36, 46, 70, 73, 74, 76, 78, 83, 84